Development of a Novel Wideband UHF Sensor with High Noise Resistance Ability for High Voltage Insulation Diagnosis

Doctoral Dissertation

Development of a Novel Wideband UHF Sensor with High Noise Resistance Ability for High Voltage Insulation Diagnosis

Tuvshinbayar BANDI
(Student number: 195F6002)

Electrical Engineering Course, Department of Engineering,
Graduate School of Engineering,
Kyushu Institute of Technology
Japan

under the supervision of
Assoc. Prof. Shinya OHTSUKA

March 2022

博士学位論文

高電圧絶縁診断のための
高いノイズ耐性を有する
革新的な広帯域 UHF センサの開発

バンディ　トゥシンバヤール
(学生番号: 195F6002)

令和 4 年 3 月

九州工業大学 大学院工学府 工学専攻
電気エネルギー工学コース

指導教員
准教授　大塚　信也

Tuvshinbayar BANDI
Kyushu Institute of Technology
Department of Electrical and Electronics Engineering
Tobata, Kitakyushu, Fukuoka, Japan
Tuvshinbayar.bandi327@mail.kyutech.jp

The doctoral dissertation supervisor and chair of doctoral dissertation approval committee:

Shinya OHTSUKA, PhD
Associate Professor, Department of Electrical Engineering and Electronics
Faculty of Engineering, Kyushu Institute of Technology
Tobata, Kitakyushu, Fukuoka, Japan

The members of the doctoral dissertation approval committee:

Masamichi NAITOH, PhD
Professor, Department of Electrical and Electronics Engineering
Faculty of Engineering, Kyushu Institute of Technology
Tobata, Kitakyushu, Fukuoka, Japan

Kazuhiro TOYODA, PhD
Professor, Department of Space Systems Engineering
Faculty of Engineering, Kyushu Institute of Technology
Tobata, Kitakyushu, Fukuoka, Japan

Satoshi MATSUMOTO, PhD
Professor, Department of Electrical and Electronics Engineering
Faculty of Engineering, Kyushu Institute of Technology
Tobata, Kitakyushu, Fukuoka, Japan

The committees have examined the dissertation entitled "Development of a Novel Wideband UHF Sensor with High Noise Resistance Ability for High Voltage Insulation Diagnosis" presented by Tuvshinbayar BANDI, a candidate for the degree of Doctor of Philosophy, and hereby certify that it is worthy of acceptance.

Abstract

Partial discharge (PD) is a pre-breakdown phenomenon that can cause the insulation deterioration of HV equipment. Thus, detection of PD signals enables us to evaluate the insulation condition and avoid catastrophic breakdown. This also brings the reliable operation of the electric power system consisting of the HV equipment.

The UHF method, one of the PD detection methods on the PD-emitted EM wave in the UHF bands, has been widely used in the electric power system because this method has many advantages, such as a non-direct connection with the HV circuit, high sensitivity, quick response and so on. However, the rapid development of ICT and digital technologies could impact the PD detection by the UHF method in view of the noise interference by the communication waves, consequently reducing the UHF sensor's sensitivity and detection ability. Thus, eliminating the communication noise is strongly required in parallel with the wideband PD detection in the UHF method. Under this background, this dissertation dealt with the development of the wideband UHF sensor with high noise resistance ability for PD detection under noise conditions.

The Multiple Narrow Band (MNB) antenna, a newly proposed and developed wideband UHF sensor with high noise resistance, was designed and optimized based on the theoretical and experimental discussion. The MNB antenna satisfies the main requirements of the UHF sensor and has excellent properties; wideband detection (more than 1 GHz) and high noise resistance for the communication and ISM bands ($S11 > -6$ dB). The design rule was summarized as a flowchart to develop the MNB antenna with different detection and elimination frequencies depending on the purpose (Chapter 3).

The discharge detection property of the MNB antenna was clarified and compared with the HA based on the PD experiments. As a result, it was proved that the MNB antenna could detect different PD signals from the different insulations and discharge types, and the signal intensity, *i.e.*, the peak to peak amplitude of the antenna output, of the MNB antenna showed a good correlation with that of the HA (Chapter 4).

The noise resistance ability of the MNB antenna was extracted using the PD in SF_6 gas under the noise source experiment. The MNB antenna can detect the PD signal under noise conditions with a higher signal-noise ratio (*SNR*) than HA under elimination frequency noises. The PD in SF_6 gas under drone noise (2.4 GHz, Wi-Fi) experiment was performed to make practical conditions. The 100 times measurement result showed that the PD detection rate under drone noise was 1% and 94% for HA and MNB antenna, respectively. The PD signal and drone noise repetition rates were investigated to understand the advantage of MNB antenna compared with HA. As a result, it was observed that the PD signal repetition was much lower than drone noise repetition for HA, while the drone noise repetition was lower than PD signal repetition for the MNB antenna because of the noise resistance ability (Chapter 5).

The communication noise elimination ability of the MNB antenna was further improved by adding the low-pass filtering function without size extension. The Filtered Multiple Narrow Band (FMNB) antenna was designed with higher noise resistance than the MNB antenna. This enhancement increased the Wi-Fi noise resistance ability from 15 dBm to more than 30 dBm. Due to this noise reduction, the FMNB antenna detected the PD signal under drone noise with a noticeable higher *SNR* than the MNB antenna. In addition, the microstrip filter can be designed for different frequency bands to resist certain noises. Moreover, the MNB antenna can be designed for different PD signals, and different noise condition depends on the purpose by adjusting the detection and elimination frequencies. It means the MNB antenna can be used in all types of HV equipment as a UHF sensor. Also, the noise resistance ability makes the MNB antenna is suitable to cooperate with other ICT and digital technology as a wireless and smart sensor. (Chapter 6).

Acknowledgments

It has been an honor and great privilege to be a doctoral student at Kyushu Institute of Technology (Kyutech) for the last three years. This dissertation would not have been possible without the support of so many people in so many ways.

First of all, I am deeply indebted to my supervisor, Assoc. Prof. Shinya OHTSUKA for his remarkable, timeless, and invaluable assistance, support, and guidance for not only the academic but also social life. Without his knowledge and assistance, this research would not have been successful. Also, I would like to extend my sincere gratitude to Prof. Bat-Erdene BAYAR, Mongolian University of Science and Technology, for all his kind advice, valuable discussion, and great encouragement. Without his insightful guidance, this dissertation would not have taken the final shape.

My deep gratitude is due to Prof. Masamichi Naithoh, Prof. Kazuhiro Toyoda, and Prof. Satoshi Matsumoto for their continuous support, deep discussion, and comments during my research as my supervisory committee members. Also, I would like to extend many thanks and appreciation to Prof. Yuki Fukumoto, Assoc. Prof. Tohlu Matsushima, Mrs. Miwa Makino, Mrs. Keiko Matsuoka for their technical guidance and useful support.

It is a pleasure to acknowledge the scholarships and kind support I received during the Ph.D. program from the Mongolia-Japan higher Engineering Education Development (MJEED) project, Mongolian University of Science and Technology, and the Ministry of Education and Science of Mongolia.

I would like to express my heartfelt thanks and appreciation to all of my friends, colleagues, and the members of Ohtsuka's Laboratory, especially for Noko Koyama san, Hiroki Furuie, and Yusuke Oishi, for their unending support and help, either in terms of my doctoral studies or in my life personally. Thank you also to the staff at Kyushu Institute of Technology, as well as the great nation of Japan.

I offer my deepest personal gratitude to my parents (Bandi Ninjbayar Orkhid, Oyuntsetseg Gunraaz Borjigon), sister (Altanzul Bandi Orkhid), and brothers

(Yalakhbayar Bandi Orkhid, Enkhbayar Bandi Orkhid) who instilled in me the belief to pursue my education. I am very grateful for the guidance, love, and confidence they invested in me.

Finally, special thanks to my lovely wife (Ganchimeg Erdenezorig Alag-aduun), daughter (Margad Tuvshinbayar Orkhid), and son (Temuge Tuvshinbayar Orkhid), who always stay with me and give me energy, happiness, and purpose for my life - this work is dedicated to them.

<div align="right">

Tuvshinbayar Bandi Orkhid

March 2022

</div>

Table of Contents

List of Figures

List of Tables

List of Acronyms

3E	Energy, Economic and Environment
AC	Alternating current
AE	Acoustic Emission
AF	Antenna Factor
AI	Artificial Intelligence
BD	Breakdown Discharge
BGN	Background Noise
BW	Band Width
CNC	Computer Numerical Control
CPW	Coplanar Waveguide
DGA	Dissolved Gas Analysis
EF	Electric Field
EM	Electromagnetic
EMC	Electromagnetic Compatibility
EMI	Electromagnetic Interference
FFT	Fast Fourier Transform
FMNB	Filtered Multiple Narrow Band
GDP	Gross Domestic Product
GIS	Gas-Insulated Switchgear
HA	Horn Antenna
HV	High Voltage
ICT	International Communication Technology
IEC	International Electrotechnical Commission
IEEE	Institute of Electrical and Electronics Engineers
IoT	Internet of Things
ISM	Industrial Scientific and Medical
LPF	Low Pass Filter
MNB	Multiple Narrow Band
NA	Network Analyzer

PCB   Printed Circuit Board

PD   Partial Discharge

PDIV   Partial Discharge Inception Voltage

PEC   Perfect Electric Conductor

PML   Perfect Matching Layers

RF   Radio frequency

SBC   Scattering Boundary Condition

SBC   Single Board Computing

SG   Signal Generator

SMA   Sub Miniature version A

SNR   Signal Noise Ratio

TE   Transverse Electric

TEM   Transverse Electro-Magnetic

TM   Transverse Magnetic

UHF   Ultra-High Frequency

Chapter 1
Introduction

1.1   Introduction

Energy is an essential issue related to the environment and economy as well as social and industrial activities in modern countries. Due to the spread of the Covid-19 pandemic, the global energy demand fell down by around 4% in 2020 [1]. However, the world population grew 1.05% in 2020, and according to the United Nations in the worldwide population prospect, it is expected to grow up to 8.5 billion in 2030, 9.7 billion in 2050, and 10.9 billion in 2100 [2]. The global GDP is estimated to be overcome by 6% in 2021 and more than 2% higher than before the pandemic in 2019. The global energy demand is predicted to increase by 4.6% in 2021, more than dropping in 2020. Thus, the global energy demand will inevitably increase.

Therefore, the world energy consumption and economy are expected to steadily increase and grow in parallel with the environmental issue even though an abrupt event such as COVID-19 that affects everyday life worldwide could happen. The environmental issue is crucial and has to be resolved without hindering economic growth as well as social and industrial activities. Consequently, the Energy, Economic, and Environment (3E) concept is more attractive and studied [3]. The coordinated development of the 3E system is the main issue to achieve stable and sustainable development of the future society because energy-economy-environment are mutually influential and mutually restrictive [4]. Electricity (electric energy) is a key for the solution of the 3E system to be a high balance because of high efficiency, easy transmission, and clean energy. Therefore, the electricity demand is expected to increase by 4.5% in 2021, and the electricity's share in total energy demand could be above 20%.

In addition, International Communication Technology (ICT) is changing the world; the major countries have already developed their own strategies as a Digital Twin, Industrial 4.0, Society 5.0, and IoT. These ICT and digital technology, including AI, reduce processing time, loss, and cost. However, they strongly require a reliable and stable electricity supply while the high voltage (HV) equipment forming the electric power system is aging and increases the failure risk.

Therefore, it is necessary to develop the infrastructure inspection, diagnosis, and maintenance technologies for the electric power system. Partial discharge (PD) detection is a well-known monitoring technique for quality assessment of insulation condition of HV equipment because PD is a pre-breakdown phenomenon. If PDs are detected in the early stage of insulation failure or deterioration of insulation system, it is possible to avoid leading it to the breakdown and the resultant system collapse.

Therefore, PD detection methods are deeply studied, and the electric method, also called the conventional method, is commonly used for PD detection in HV equipment. This method has very high sensitivity and is standardized by (International Electrotechnical Commission) IEC-60270 and is useful for a factory measurement. However, it is difficult to on-line and real-time measurements such as the measurement during the operation of HV equipment in an electric power system because this method needs a direct electrical connection with the equipment under test and a high capacitance for filtering.

Among other un-conventional methods, the UHF method is widely used for PD detection because of high sensitivity, on-line, safety, and non-contact connection with HV equipment based on electromagnetic (EM) waves emitted from PD activity. Also, this method will be standardized near future as IEC TS 62478 "High voltage test techniques – Measurement of partial discharges by electromagnetic and acoustic methods" [5]. Fig. 1.1 shows the overview of the impact of PD detection for this electric and digital society.
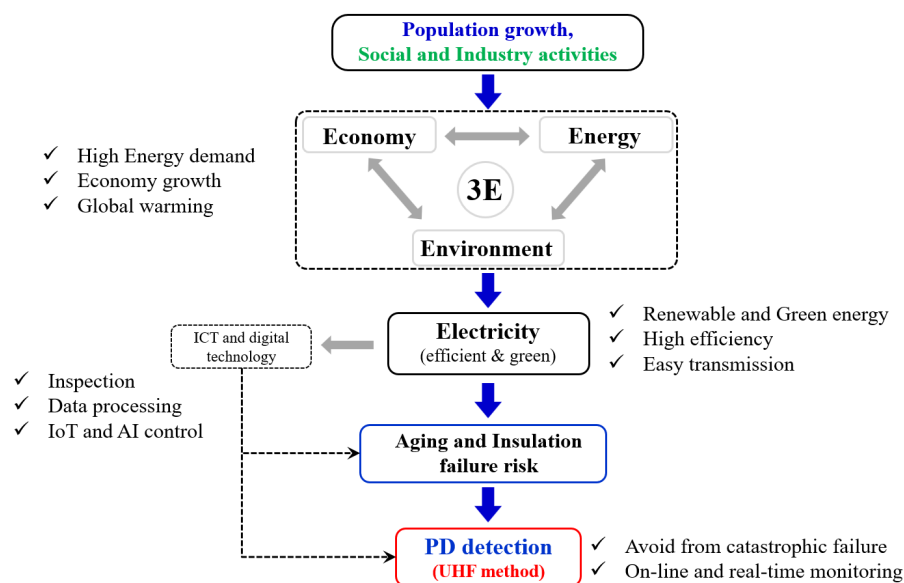
Fig. 1.1.   The schematic overview of the PD detection effect

In the UHF method, the wideband measurement is suitable for PD detection due to the broadband EM wave emitted from the PD source. However, wideband measurement is sensitive for not only PD-emitted signal but also noise, whose frequencies are included in the detectable frequency bands. The ICT and digital technologies are used frequencies mainly spread in the UHF band such as cell phone and ISM bands, which affect the PD detection as noise interference. Therefore, a new wideband UHF sensor with high noise resistance is required to detect the PD signal under the coming frequently wireless communication age.

This chapter deals with the PD detection methods, especially the UHF method, and a literary review of the UHF sensor. In addition, the aims, objectives, motivation, novelty, and outline of this dissertation are also discussed.

1.2 HV equipment failures and insulation diagnosis

1.2.1 HV equipment failures

The main issue of electric power systems is the increasing energy demand in parallel with aging high voltage (HV) equipment. Therefore, the influence of aged equipment in electric power systems, especially power transformers and gas-insulated switchgear (GIS), are studied to avoid breakdown, minimize blackout, reduce cost, and extend the lifetime equipment and enhance the reliability of power system.

Power transformer: The main factors that affect the life expectancy of transformers are (i) the initial thermal, electrical, and mechanical properties of insulation materials, (ii) the stress of thermal, electrical, and mechanical stress (iii) environmental conditions such as ambient temperature and (iv) permissible degree of deterioration [6]. It means the transformer insulation system suffers degradation due to thermal, electrical, and mechanical stress.

M.S.A. Minhas and other researchers [7] carried out the survey on failures in 188 power transformers in the voltage range of 88 kV to 765 kV and power rating from 20 to 800 MWA and reported that 30 % of failures due to aging of insulation, 23 % were tap-changers, 15% were core problems, 12% were lightning and switching problems, and others. In the study published by CIGRE [8], about 25 to 30 % of major failures are associated with a breakdown of insulation being in service over 20-25 years due to accumulation of moisture and contamination, and degradation. It showed the failure reason of power transformer involves predominantly insulation problems in service.

Gas-insulated switchgear (GIS): The GIS reliability survey was carried out based on the information from utilities about their equipment population of SF_6 circuit breakers and GIS in which 55 utilities from 24 countries participated [9]. This survey reported that the major GIS failure modes were the failure to perform the requested operation (63 %), dielectric breakdown (23%), loss of mechanical integrity (4%), loss of electrical connections integrity in primary and secondary circuits (1%) and others (9%).

In addition, the dielectric breakdown failure mode tends to increase, and failed components were changed due to the age of GIS. For example, in the GIS manufactured before 1993, the circuit breakers and switches (disconnector and earthing) failed in about 90% of the cases; the rest of the failures were caused by the failure of bus bars/bus ducts and instrument transformers. However, in GIS manufactured in 1994–2005, the proportion of the components in model failure changed; the failures of bus bars/bus ducts increased significantly, around 33% of total failures. It means the failure related to the insulation degradation is more critical than failures caused by operation and mechanical problems.

Therefore, the insulation diagnostic is an essential tool to prevent malfunctions and a catastrophic electrical breakdown of HV electric equipment, leading to a huge financial consequence. Thus, effective, accurate, and real-time insulation diagnosis technologies are needed to determine the potential insulation failure earlier.

1.2.2 Partial discharge detection for the insulation diagnosis

Insulation diagnostic and condition monitoring systems are required to keep the normal operation of the electric power system and diminish the probability of HV equipment failure. The insulation condition monitoring system works based on measurements such as temperature measurement, oil pressure monitoring, vibration measurement, and partial discharge (PD) measurement, which is the well-known insulation diagnostic method.

Partial discharge is an electric discharge that does not completely bridge the electrodes [10], i.e., a pre-breakdown phenomenon. PD commonly exists in HV equipment when the insulation system is deteriorating or has an inherent fault condition, and the electric field exceeds the dielectric strength [11]. PD could be generated by initial electrons and a high enough electric field to cause ionization [12]. Consequently, PD development is influenced by space charges like electrons and ions generated by the

ionization and the attachment as well as discharge channel conductivity [13]. Even if the amplitude of the PDs is typically small, they cause the development of insulation deterioration or continuously propagate until the insulation is unable to resist the electrical stress, and it leads to breakdown failure of HV equipment. So, it is possible to estimate the insulation condition and avoid a catastrophic failure of the HV equipment as detecting PD activity. In addition, PD measurement is significant in the manufacturing process of the HV equipment in view of quality control and assessment.

Fig. 1.2. shows the concept to perform insulation diagnosis of electrical power apparatus by PD detection [14]. Total understanding is needed to successfully perform the diagnosis, which has four main parts (i) PD phenomena, (ii) Propagation properties, (iii) Measurement system and sensor, and (iv) Data acquisition analysis / Judgment and decision. In addition, it needs to consider the noise environment, which strongly affects the insulation diagnosis technology. Depending on the signal types, the different frequencies affect for PD detection process as noise. For example, the communication and ISM bands work as noise for the UHF method, while the amateur radio and broadcasting bands represent noises for the acoustic emission method. Especially nowadays, the digital technology rapidly developed, the noise condition is a big factor for PD detection.
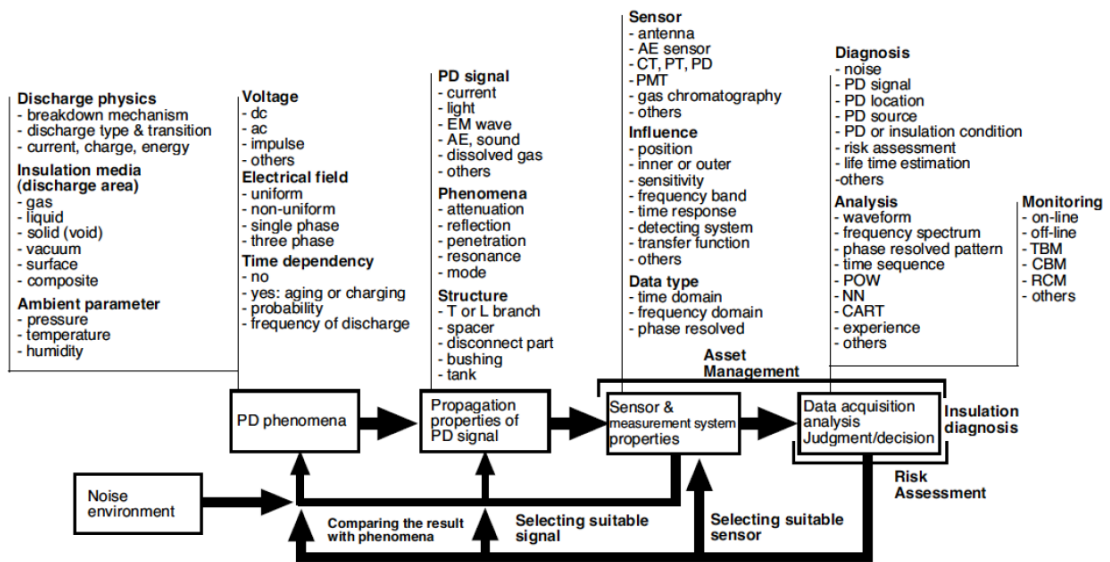
Fig. 1.2.   Concept to perform insulation diagnosis of electrical power apparatus detected by PD with high reliability [14]

- PD phenomena: The discharge phenomenon differs depending on the configuration of the insulation system, the surrounding environment, the applied voltage, the electric field distribution, and it is necessary to consider the change with time when the insulating material is deteriorated or charged. In addition, the PD mechanism is changed based on the insulation media. For liquid insulation, the free metal particle and impurity of insulation media can affect the PD development as an internal discharge [15]. For solid insulation, if impurity or structural defects could cause the internal PD. For example, the voids in epoxy resin are one of the sources of PD in solid insulation. Also, the surface discharge can occur in solid insulation when an electric field stress component is parallel to a dielectric surface. For example, the discharge can occur at the end of power cables, the overhang of generator winding, and the metal casing of bushing that contacts the epoxy resin insulator. The corona discharge occurs at a sharp protrusion or edge of high electric field metallic conductors in the gas-insulated system. Small sharp particles or dust on the surface, which acts as contamination in the gas-insulated system, may initiate the discharge. Then, the electrical discharge will develop at the tip of the particle and cause insulation failure. This study investigates the PD in SF_6 gas for the main PD source. PD type in SF_6 gas is typically streamer and leader discharges that differ from the conductivity of the discharge channel, which results in a difference in the breakdown risk.

- Propagation properties of PD signal: Signals generated by PD include electromagnetic waves, ultrasonic waves, decomposed gas, and light. Because those signals propagate through the environment and are acquired by a sensor, it is necessary to understand the propagation mechanism that depends on the device structure up to the sensor position. For example, attenuation, reflection, and resonance can change the signal properties. It is important to clarify the mode characteristics unique to signals and structures such as TEM, TE, and TM modes when propagating electromagnetic waves in the HV equipment. For example, the TE mode affects the UHF signal propagation as a resonant frequency depending on the physical dimension of the GIS tank.

- Sensor and measurement system: The sensors are the most important device for the measurement system and can be designed in many ways based on the purpose. For example, current transformer, UHF, acoustic emission, and light sensors are used based on purpose. The sensor installation position affects sensitivity and can be

roughly divided into the inside and the outside of the equipment. Even if the inside sensor gives the highest sensing, very few equipments have hand holes for inside sensor installation. Thus, the outside sensor is required for PD detection. The sensor can be evaluated by sensitivity, frequency band, time response, radiation pattern, detection field, etc. In addition, smart sensors are attracted for wireless signal transmission, single-board computing (SBC), IoT, AI, etc.

- Data acquisition analysis / Judgment and decision: Since insulation diagnosis is performed based on the acquired signal, it is important to select the data processing method, timing, and format according to the purpose, such as PD discrimination, PD location, and so on. In addition, it is necessary to distinguish the PD emitted signal from unnecessary signals in order to measure PD signal, especially from noise.

Understanding the whole series processes of insulation diagnosis technology as described above is important in establishing an insulation abnormality diagnosis system. In this study, the PD measurement system and detection methods are discussed more detail, especially the UHF method and sensor.

1.2.3   Partial discharge detection methods

PD activity generates related physical phenomena such as PD current, light emission, acoustic and ultrasonic waves, chemical reaction and byproduct, and electromagnetic (EM) waves. Accordingly, PD detection and/or measurement are carried out based on these physical phenomena by considering which phenomenon is suitable to apply in terms of diagnostic purpose and requirement. Some monitoring methods were developed for PD detection, such as electrical, acoustic, chemical, optical, and ultra-high frequency (UHF) methods. Those methods are roughly divided into two parts conventional and unconventional methods.

Conventional method: Measurement of the apparent charge (Q) of PD is known as a conventional or electrical PD detection method and standardized by (International Electrotechnical Commission) IEC 60270 [16]. Fig. 1.3 shows the basic measurement circuit of the conventional PD measurement, where Z and C_k represent the filter for high-frequency interference from the power sources, and C_t represents a coupling capacitor and test object; R is the input impedance of the measuring system. The PD charge is measured when PDs are first observed in the test object at the lowest applied voltage, called partial discharge inception voltage (PDIV). The apparent charge is the integrated

current generated by PD activity transmitting through the test circuit and measured by the measurement device. The charge amount is generally measured by picocoulombs (pC). The capacitor blocks low frequency and passes high frequency of PD current. The PD current is discriminated from noise signals using their rise time because PD current usually generates high rise time. However, the noise from power systems can be detected by the capacitor. The conventional PD detection method is useful for factory and laboratory conditions but is not appropriate for on-site, on-line detection of PD.
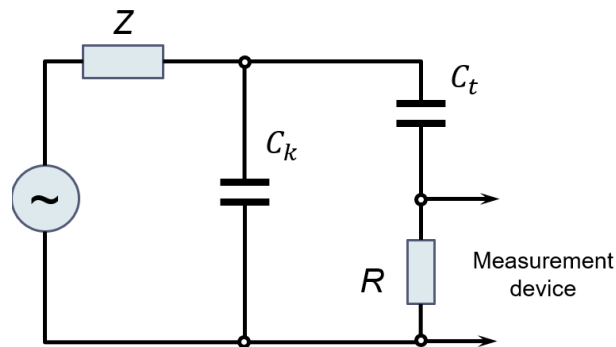
Fig. 1.3. Basic measurement circuit of PD charge

Unconventional PD detection methods: The unconventional PD detection methods use special sensors to detect physical phenomena caused by PD activity. The sensors are not electrically connected to the HV circuit, such as chemical, optic, sound, vibration, and EM wave sensors, as shown in Fig. 1.4. In addition, all methods have advantages and also disadvantages. In order to fill the disadvantages, combined methods were used for PD detection, such as the UHF method combined with the optical or acoustic method.
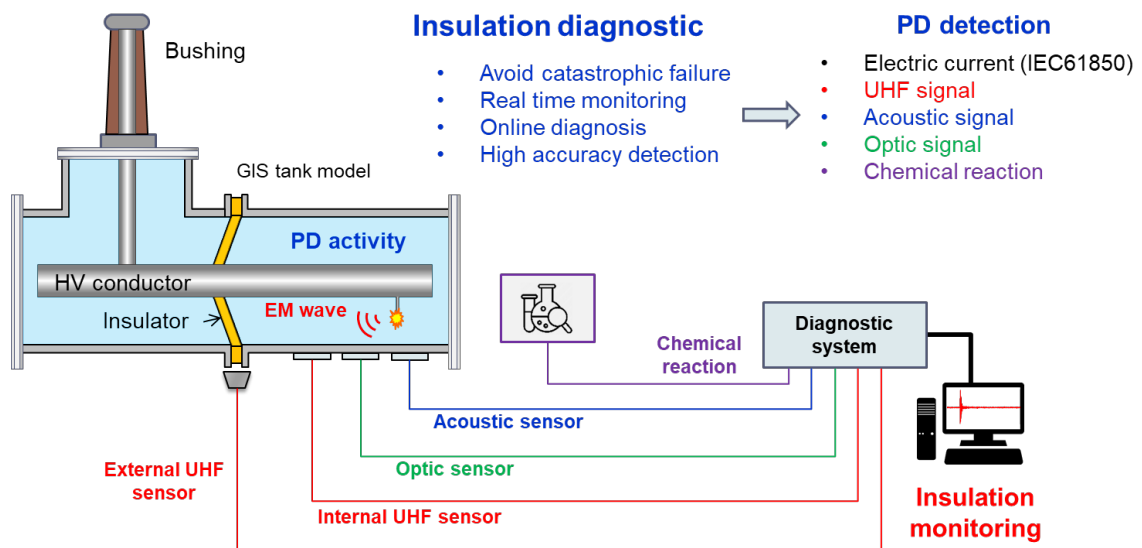
Fig. 1.4. Unconventional PD detection methods

Chemical method: The chemical method, called a dissolved gas analysis (DGA), is based on the volume and content of gas dissolved in insulation. This method is commonly used for PD detection inside power transformers and GIS as detecting the chemical decomposition of insulation materials caused by thermal and electrical stress. For power transformers, the decomposition of paper and oil insulation produces many chemical compounds, gas and solid such as carbon monoxide (CO), carbon dioxide (CO_2), hydrogen (H_2), methane (CH_4), acetylene (C_2H_2), ethylene (C_2H_4) and ethane (C_2H_6). There are some standards for DGA methods, ICE 60599 and IEEE Std C57.104TM-2008, which indicate the level of the chemical compounds for normal operating conditions of power transformers [17].

Also, the chemical PD detection method is useful for GIS filled with SF_6 gas (Sulfur hexafluoride). SF_6 gas is chemically inert and thermally stable for normal temperature [18], but SF_6 gas is decomposed into metal fluorides and sulfur fluorides (SF_4) due to PD phenomena. If discharge occurs around aluminum and copper conductor, the SF_6 gas is decomposed into SF_4 and copper fluoride (CuF_2). The DGA method is very effective PD detection inside of power transformer and GIS, but the measurement result shows the historical in nature and not descriptive of the instantaneous condition monitoring. It means the DGA method is not on-line and cannot detect the PD location.

Acoustic Emission (AE) method: AE method using the piezoelectric sensor for detecting PD is commonly used for power transformers. The electron avalanche of a PD activity releases energy that causes local heating of the gas or other material and, hence, causes a rapid local pressure increase. The resulting pressure wave propagates through the medium at a certain speed as acoustic signals such as 343 m/s in the air, 133 m/s in the SF_6 gas, and 1380 m/s in the transformer oil [20-21]. Due to the propagation characteristics of the insulation medium and apparatus structure, ultrasonic AE is measured in the 20 kHz to 500 kHz frequency range [21]. The AE method is on-line and enables to determine PD location as three-dimensional. However, the drawback of this method is sensitivity for noisy environments, outside corona discharges, high attenuation, and structure-borne interference depending on the path between the sensor and PD source [22].

Optical method: The optical method detects the light emission of PD activity. The spectrum and intensity of the optical signal depend on the insulation medium (insulation type) and the intensity of PD activity. The optical spectrum extends from ultraviolet over

the visible range into the infrared. The corona discharge emits the optical signal with the wavelength from 280 nm to 400 nm, while discharge in oil insulation emits the signal from 400 nm to 700 nm [23]. The optical method is highly immune against electromagnetic noise and is a safety method because the entire measurement system is isolated. However, it needs eye contact with the PD phenomena for detection, and the detection area is limited [24].

Ultra-high frequency method: The UHF method was first introduced by B. F. Hampton in 1987 for PD detection in GIS based on the electromagnetic wave emitted caused by rapidly increasing PD current pulse [25]. Then, a multiple-year research effort has been developed the UHF method to monitor insulation condition, and application of the UHF method widened for other HV equipment such as power transformer, cable, and so on. Among other unconventional methods, the UHF method is mostly used because of high sensitivity for PD detection, an immunity for low-frequency noise, on-line and real-time monitoring, non-direct connection with HV circuit, compact and low-cost structure. In addition, the UHF method is suitable to cooperate with other methods such as optical sensors [27] and standardized by IEC TS 62478 "High voltage test techniques – Measurement of partial discharges by electromagnetic and acoustic methods" standard.

The electromagnetic (EM) waves emitted from PD activity have very high frequency (VHF; 30 ~ 300 MHz) and ultra-high frequency (UHF; 300 MHz ~ 3 GHz) components and are propagated from the PD source in all directions. It is possible to evaluate and estimate the PD activity by catching these EM waves. In order to evaluate PD activity by the UHF method, at least three stages of information are needed; (i) PD detection, (ii) classification, and (iii) location. For the detection stage, the UHF sensor can detect the PD signal existence and amplitude in the time domain. Based on the measured EM wave shape and frequency component, it is possible to discriminate the PD type and classification. Then, PD location can be calculated as a time difference between the signal's arrival time at multiple sensors located at different locations.

1.3 UHF sensor types and comparison

The UHF sensor is an essential part of the UHF method to receive the EM wave. Therefore, many researchers pay attention to designing different UHF sensors depending on the purpose. This section discusses the literature review based on the IEEExplore database. The "partial discharge, UHF method, and antenna or sensor" were used as keywords; as a result, 72 journal papers introducing the UHF sensor were found from IEEExplore. Fig. 1.5 shows a relation between published year and published numbers of papers. It seems that the research interest related to the UHF method and sensor is increasing with each passing year.
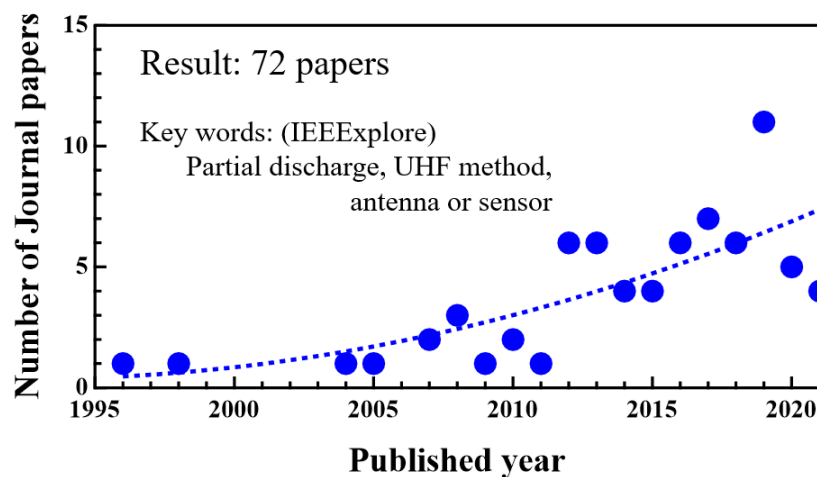
Fig. 1.5. Relation between number of published papers and published year

Table 1.1 shows the sensor types used for the UHF method; the UHF antennas are used as UHF sensors. Depending on the detection frequency band, the sensors could be classified into narrow and wideband sensors. Fig.1.6 shows the proportion of narrow and wideband sensors using founded journal papers. The wideband sensor is commonly used for the UHF method because the PD emitted signal has a broadband characteristic. Consequently, the advantage and disadvantages of the above types of sensors are discussed.
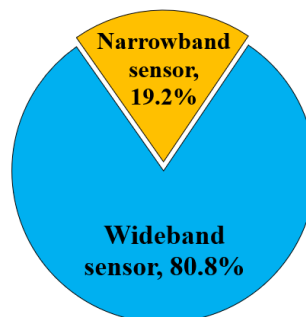
Fig. 1.6. The ratio of wide and narrowband antennas usage for UHF method

Table 1.1 UHF sensors used for PD detection

#	Type	Number
1	Disc antenna	16
2	Archimedean spiral, two arm spiral antenna	9
3	Conical antenna	8
4	Monopole antenna (narrowband)	7
5	Hilbert, Hilbert fractal, Moor fractal Antenna	7
6	Dipole antenna	5
7	Patch antenna (narrowband)	4
8	Printed circular, ellipse monopole antenna (wideband)	4
9	Horn antenna	3
10	Biconical antenna, Bowtie antenna, Elliptical dipole antenna	4
11	Discone antenna	2
12	Log-periodic antenna	2
13	Loop antenna (narrowband)	2
14	Slot antenna	2

1.3.1 UHF sensor types

Horn sensor: The Horn antenna (HA) is one of the highest sensitive and plate response antennas, which consists of a horn and waveguide section that reduces the reflection of open-end aperture. However, their large dimension is difficult to install in the HV equipment and would change the electric field distribution and reduce the distance between the HV conductor and equipment body, leading to the breakdown. Therefore, HA is generally used for laboratory conditions as an external reference sensor [27].
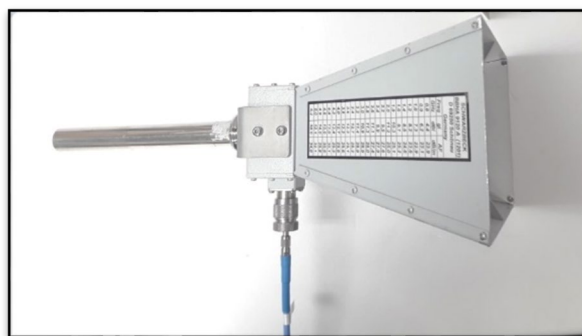
Fig. 1.7. Horn antenna (BBHA9120A; 0.8~5.2 GHz)

Disc sensor: The disc sensor represented as disc antenna and disc coupler is one of the most used sensors for the UHF method because a flat shape made it is simply installed GIS and transformer as an external and internal sensor. The disc antenna is the wideband

antenna and covers the PD emission frequency band [28]. However, it can be interference by communication and radio frequency noises.
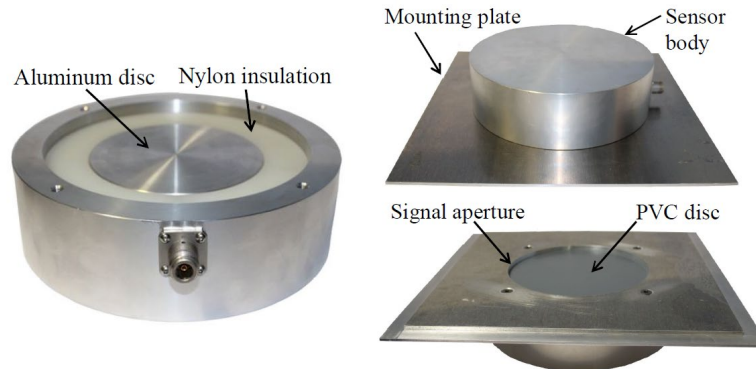
Fig. 1.8. Disc antenna (0.5~1.5 GHz) [28]

Spiral sensor: The printed spiral, Archimedean spiral, and two arm spiral antennas represent the spiral sensor. The advantages of the spiral antenna are broadband detection and compact printed structure [29]. However, theoretical calculations have shown that the input impedance spiral antennas are approximately 188 Ω [30]. Thus, the spiral antennas need the impedance matching part to achieve impedance consistency from the transmission line to the antenna. On many occasions, to achieve impedance matching a coaxial Balun, a printed microstrip transmission line or a coplanar waveguide is used to feed the spiral antenna from the middle point. This feed structure would increase the thickness of the spiral antenna, which is a disadvantage for the UHF sensor.
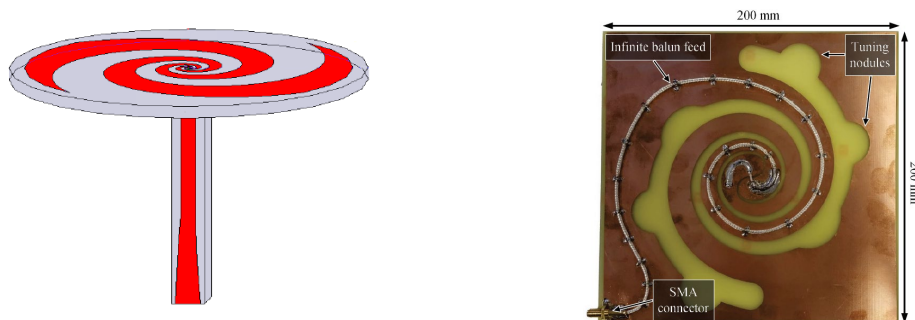
(a) The planar equiangular spiral antenna with microstrip feed

(b) The printed spiral with tuning modules

Fig. 1.9. Printed spiral antennas [29, 30]

Dipole antenna: The standard dipole antenna is generally a narrow band antenna. Thus, the detection sensitivity is low compared with a wideband antenna. To increase the detection bandwidth of the dipole antenna, the pole shape should be changed or adding some stubs. For example, an elliptical dipole sensor is used for PD detection in [31], and

K. Khotimah developed a T-shaped dipole antenna [32]. Even if the changing shape increases the frequency bandwidth, it also increases the antenna size.

(a) T-shaped dipole antenna (b) Ellipse dipole antenna
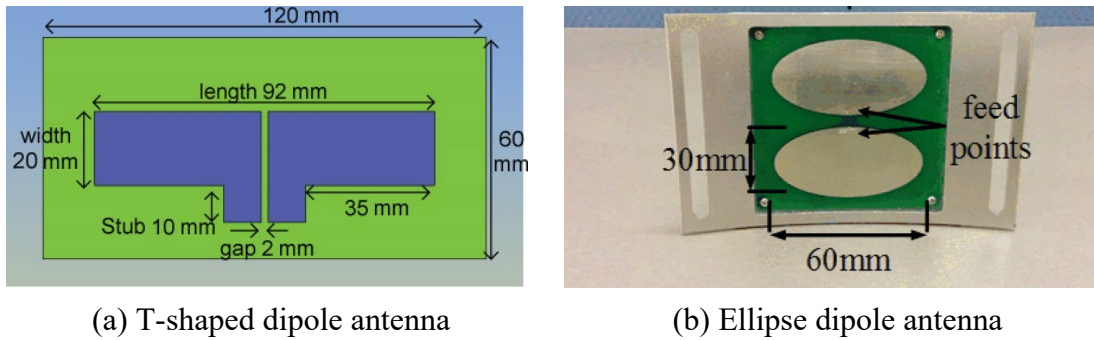
Fig. 1.10. Printed dipole antennas [31, 32]

Loop antenna: The typical loop antenna is narrowband and is commonly installed in the support insulator of GIS because this type of antenna is sensitive to magnetic fields. The loop types antennas are more sensitive to TM waves propagating in GIS than antennas, which are sensitive to an electric field, but less sensitive to TEM and TE mode [33, 34]. Therefore, the detection performance of loop antenna is related to the PD type and signal propagation in GIS. In addition, the magnetic field detection characteristic is a cause of difficult installation for the inside of GIS, which reduces the distance between the conductor and grounded flange.

(a) Printed meandering loop antenna (b) The wire loop antenna embedded in the barrier insulator
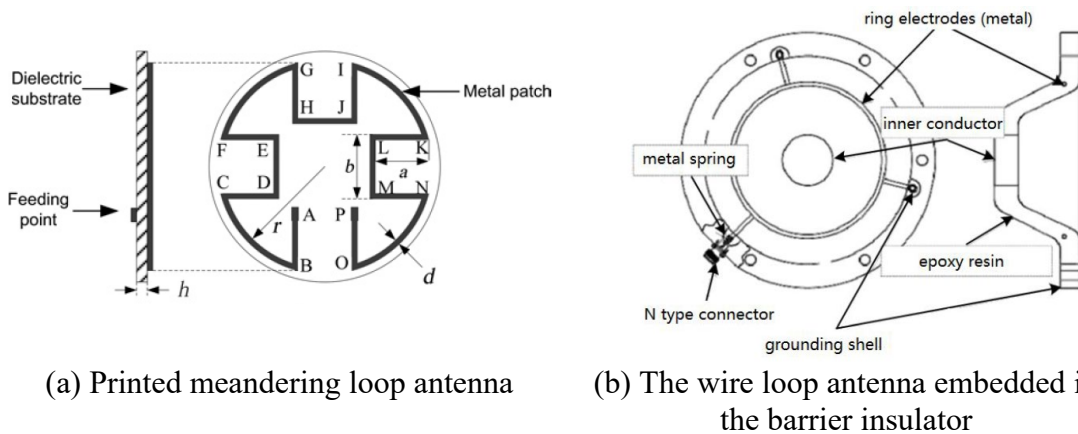
Fig. 1.11. Printed and wire loop antennas [33, 34]

Conical antenna: The conical antenna is an excellent wideband antenna for PD detection in transformers using an oil drain valve [35], but its detection frequency is related to the size. Since the antenna size for PD detection has limitations, the wideband conical antenna is difficult to use in the GIS tank. Also, the low-frequency band detection is not suitable for the UHF method due to low sensitivity and high noise interference.

(a) Conical antenna   (b) Installation of the conical antenna
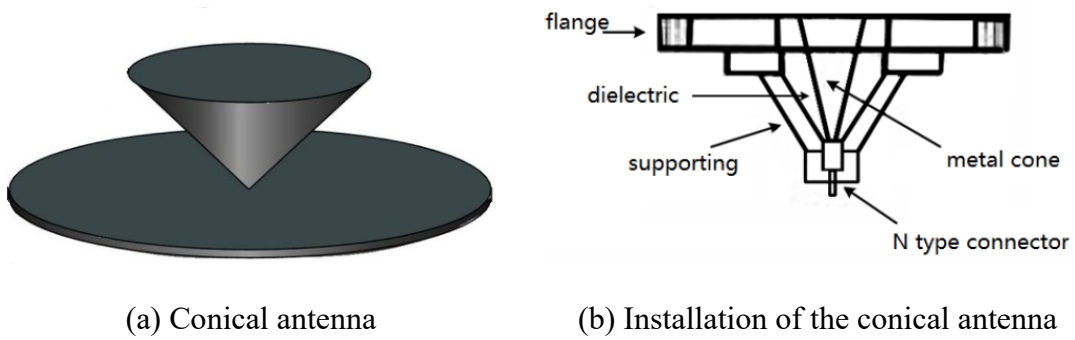
Fig. 1.12. Conical antenna [35]

Patch antenna: Patch antenna is one of the compact flat-type antenna, generally narrowband characteristic [36]. Even if the patch antenna is compact and easily installed for high voltage equipment, the detection sensitivity is lower than wideband antennas because of the antenna bandwidth. In addition, it is difficult to discriminate the PD types.
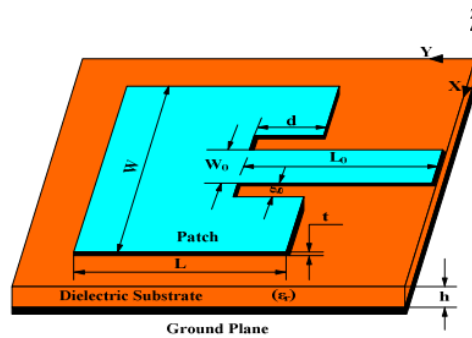
Fig. 1.13. Patch antenna with microstrip feed [36]

Monopole antenna: The typical monopole antenna is generally narrowband, but changing the shape of the pole adjusts the bandwidth of the monopole antenna like a dipole antenna [37, 38]. In addition, due to electric field detection, compact and adjustable structure, printed monopole antennas are widely used for PD detection, such as circular, ellipse, octagonal, and strip monopole antennas.

(a) Octagonal shaped   (c) Bio-inspired shaped

Fig. 1.14. Wideband monopole antenna [37, 38]

1.3.2 Comparison of UHF sensors

Based on the literature review of the UHF sensor, it can be concluded that the UHF antennas are used as a UHF sensor, and wideband antennas are suitable for PD detection more than narrowband antennas because of high sensitivity.

The UHF sensors used for PD detection are shown in Table 1.2 with some main parameters.

- The detection bandwidth is an important parameter for UHF sensors to define the detection sensitivity; thus, the wideband sensor is appropriate for the UHF method.

- The sensor size is a considerable parameter because of installation issues in HV equipment. So, flat and compact-sized sensors have advantages for preventing the effect of the insulation distance of HV equipment such as patch, printed monopole, and dipole antennas.

- The determining PD location is one of the superiorities of the UHF method. Using the UHF sensor can detect the wide-angle or omnidirectional, it is possible to detect the PD signal location using a few sensors.

- In addition, electric antennas are used wider than magnetic antennas because of the difficulty of installation in HV equipment.

Table 1.2. Comparison of UHF sensors

#	Antenna	Frequency band (GHz)	Bandwidth (GHz)	Size (mm)	Radiation pattern	Field detection
1	Horn antenna (BBHA9120A)	0.8~3.0	2.2	245x220x142 W x L x T	Directivity	Electric
2	Disc antenna [28]	0.55~1.0; 1.1~1.4; 1.5~1.6	0.85	r =60, T=16	Directivity	Electric
3	Spiral antenna [29]	0.3~3.0	2.7	r =109, T=211.5	Directivity	Electric
4	Conical antenna [39]	0.1~1.0	0.9	r =855, T=54	Directivity	Electric
5	Dipole antenna [34]	1.1~2.0	0.9	120x60x0.3 W x L x T	Omnidirectional	Electric
6	Loop antenna [33]	0.48~0.52; 0.8~0.85; 1.1~1.2	1.0	r =54, T=1.6	Omnidirectional	Magnetic
7	Patch antenna [36]	0.485~0.515	0.03	174x174x1.5 W x L x T	Directivity	Electric
8	Monopole antenna [38]	0.575~3.0	2.425	124x77x1.6 W x L x T	Omnidirectional	Electric

1.4   Research motivation and objective

The wideband sensor is more suitable for the PD detect field than the narrowband sensor because the PD-emitted EM wave has broadband characteristics. However, in view of the situation spreading the digital and communication technologies into the many fields, including the high voltage field, the wideband sensor is in a disadvantageous selection for PD detection under the very frequently communication environment, *e.g.*, a digital substation or an IoT world. In the UHF band related to the UHF method, many frequencies have been ordinarily used for communication and broadcasting, e.g., cellphone for 700, 800, 900MHz and 1.5, 1.7, 2.1, and 2.5 GHz bands, ham radio for 430MHz and 1.2 and 2.4 GHz bands, Wi-Fi connection for 2.4 and 5 GHz bands, and some of the industry, science and medical (ISM) bands are also included in the UHF band as the center frequencies of 433.92 and 915MHz and 2.45 GHz. It means these utilized frequencies work as noise against the UHF method. Fortunately, the communication and ISM frequencies are limited in very narrow frequency bands. Thus, if the wideband sensor realized only eliminating these communication frequencies in the detectable bandwidth, this sensor could have high sensitivity for PD detection without noise interference. This idea motivates the development of the novel wideband UHF sensor with noise resistance.

Using the wideband antenna with cascaded lumped filter, it is possible to detect the PD signal without noise interference, as shown in Fig. 1.15 [40]. However, this method has many disadvantages, such as the large size of a measurement system, a vulnerable connection, an interference of cascaded structure, and difficulty of installation in HV equipment. From this point of view, a new Multiple Narrow Band (MNB) antenna has been developed as a UHF sensor [41]. Fig. 1.16 shows the schematic diagram of the MNB antenna concept. The antenna designing process is discussed in detail in Chapter 3.
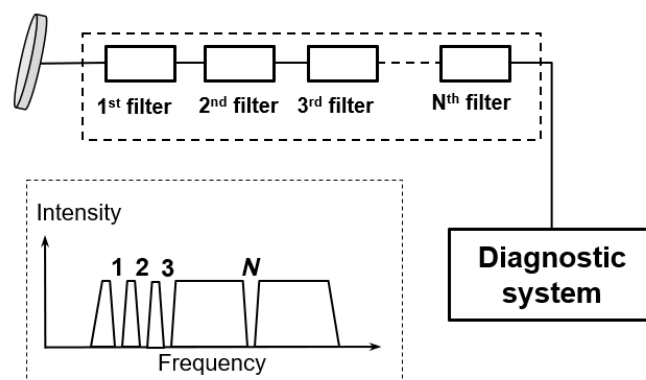
Fig. 1.15. Wideband antenna with cascaded filter for multi-resonant frequency [40]
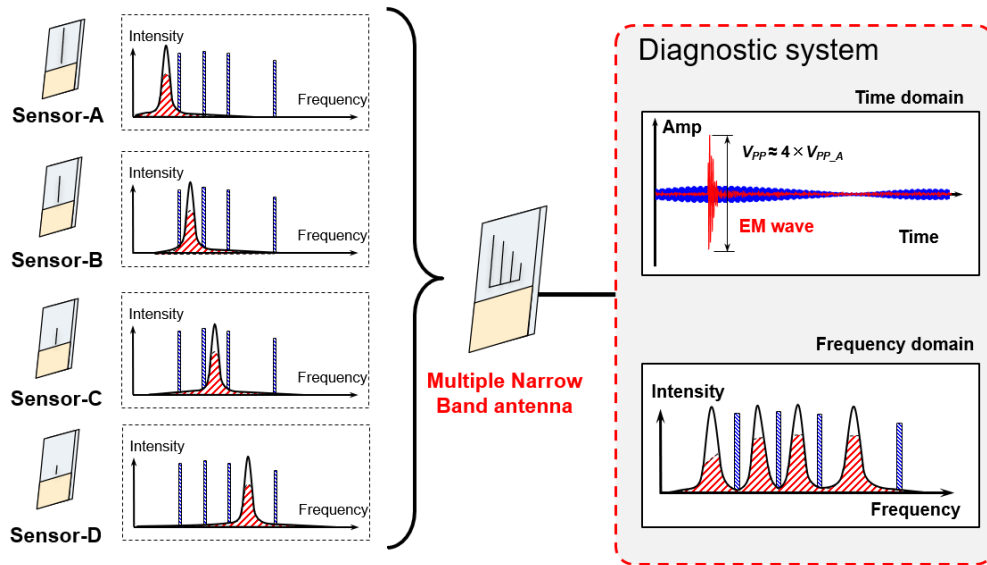
Fig. 1.16. The schematic diagram of the MNB antenna concept

Fig. 1.17 shows the ideal comparison of UHF sensors as the time and frequency domain for PD detection. The wideband antenna can detect the PD signal, but it can be masked by noise because the noise intensity and repetition rate are higher than the PD signal at the communication and ISM frequency band. Using the narrowband antenna makes it possible to avoid noise interference, but the acquired intensity of the PD signal is reduced drastically. The multiple-band detection increases the detection frequency bandwidth of the MNB antenna to be the same as a wideband antenna and eliminates some selective noise frequencies as noise resistance. Therefore, multiple-resonant frequency antennas can detect the PD signal with high sensitivity, same as the wideband antenna, and avoid communication noises as a narrow band antenna.

There are few UHF sensors with multi-resonance introduced for the PD detection field. For example, the quarter-wavelength monopole and loop sensors receive the target frequency band and high-order oscillations [33], even narrowband antennas. Unfortunately, those high-order oscillations frequencies could not be adjusted independently. Therefore, the objective of this study is to develop the new MNB antenna for PD detection as a wideband UHF sensor with noise reduction ability, and the detection and elimination frequencies of the MNB antenna should be simply adjusted independently of each other [42] for different types PD detection and different frequency noises. The noise elimination ability increases the PD detection ability of the MNB antenna under the communication and ISM band. In addition, it gives a chance to cooperate with the drone and other electronic devices as a smart sensor based on the IoT,

AI, and digital technologies without the inference of communication and ISM frequency band [43].
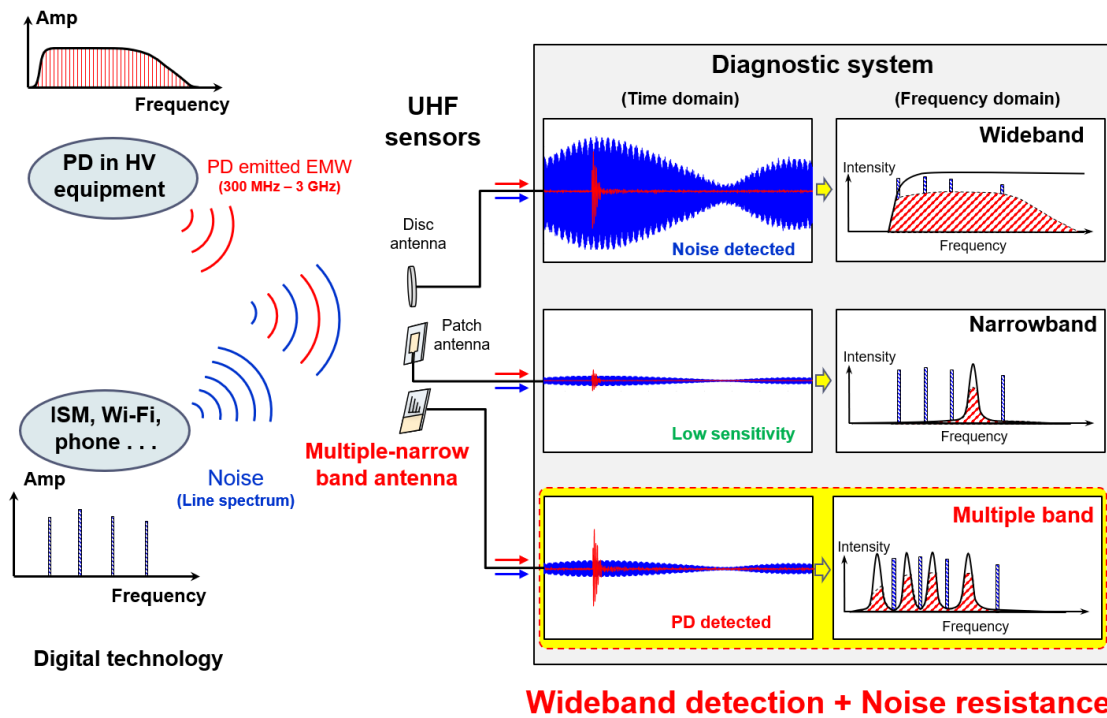
Fig. 1.17. The comparison of UHF sensors as a time and frequency domain response for PD detection under noise conditions

1.5   Dissertation Outline

This dissertation presents the novel wideband UHF sensor realized by the multiple narrowband antenna with the communication noise resistance ability for insulation diagnosis of HV apparatus. The multiple narrowband means that the sensor is able to detect PD signal with wideband by selectively choosing the frequency component eliminating the communication frequencies working as noise. This dissertation consists of seven chapters, and the outline of each chapter is as follows:

Chapter 1 introduces the background and objectives of this dissertation, which deals with the UHF sensor for the insulation diagnosis, *i.e.,* the UHF method, to detect PD signals in the HV electric power system. There are researches on the UHF sensors and noise elimination technologies, but the combined sensor has never been developed so far. The author firstly proposed the wideband UHF sensor with high noise resistance ability for the insulation diagnosis. Also, the literature review of UHF sensors and dissertation outline are promoted.

Chapter 2 describes the experimental setup, including the wideband UHF sensor the author designed and developed and the experimental procedure. As a discharge signal, not only breakdown and partial discharges in the air but also PDs in SF_6 gas or electric tree in XLPE sample were prepared. As a communication noise, artificial noise emitted from SG and HA or an actual Wi-Fi communication signal emitted from a commercial drone was applied. Breakdown, partial discharge, artificial and Wi-Fi noise used in this study are explained based on the experiment condition, apparatus, and setup.

Chapter 3 deals with how to design and fabricate the novel wideband UHF sensor that is realized by the MNB antenna with a single surface PCB and an SMA connector. Also, the parameter optimization of the antenna is shown based on experimental results together with theoretical performance obtained by the COMSOL simulation.

Chapter 4 indicates the experimental result on fundamental properties of the developed wideband UHF sensor on the discharge signal detection with different discharge sources. The (i) PD detection ability and (ii) discrimination ability of MNB antenna for PDs in different insulation based on the breakdown and partial discharge experiments results. The frequency components of the PD emitted signal are changed based on the insulation materials and PD types. The MNB antenna can be designed to detect PD in different insulations by adjusting resonant frequencies of the MNB antenna as changing the length of strips.

Chapter 5 also indicates the experimental result of the developed wideband UHF sensor on the elimination properties with two different types of noise. The MNB antenna was applied to measure the PD in SF_6 gas under the following two noises: (i) Artificial noises – emitted by a signal generator through HA (elimination frequencies of MNB antenna) and (ii) Real Wi-Fi communication noise emitted from a commercial drone – 2.4 GHz.

Chapter 6 shows the improvement of the noise elimination ability by introducing the low-pass filtering function into the sensor by which the capacitance and the resistance were formed by making the micro-strip patterns on the PCB. This sensor added the filtering function was called the enhanced filtered multiple narrowband (FMNB) sensor. The FMNB antenna was applied to measure the PD in SF_6 gas under Wi-Fi noise emitted from the commercial drone and compared with the MNB antenna and standard HA.

Chapter 7 summarizes all the contents discussed in this dissertation and recommendations for future work.

References

[1] International Energy Agency, "Global Energy Review 2021," *Glob. Energy Rev. 2020*, pp. 1–36, 2021.

[2] U. N. D. of E. and S. A. P. Division, *World population prospects 2019*. 2019.

[3] J. Uribe-Toril, J. L. Ruiz-Real, J. Milán-García, and J. D. P. Valenciano, "Energy, economy, and environment: A worldwide research update," *Energies*, Vol. 12, No. 6, 2019.

[4] Y. Du, K. Xiang, Y. Li, C. Lin, X. Huang, and H. Lin, "Research on Relationship between Energy-Economy-Environment and Index System under the New Situation," *2019 IEEE PES Innov. Smart Grid Technol. Asia, ISGT 2019*, pp. 2932–2935, 2019.

[5] British Standards Institution, "High Voltage Test Techniques—Measurement of Partial Discharges by Electromagnetic and Acoustic Methods," 2016.

[6] S. Chakravorti, D. Dey, and B. Chatterjee, "Recent Trends in the Condition Monitoring of Transformers: Theory, Implementation, and Analysis," *Power Syst.*, Vol. 67, pp. 1–26, 2013.

[7] M. S. A. Minhas, J. P. Reynders, and P. J. de Klerk, "Failures in power system transformers and appropriate monitoring techniques," *IEE Conf. Publ.*, Vol. 1, No. 467, pp. 94–97, 1999.

[8] V. M. Lokhanin, A K, Morozova, T I, Shneider, G Y, Sokolov, V V, and Chornogotsky, "Internal insulation failure mechanisms of HV equipment under service conditions," *Cigre Rep.*, Vol. 15, No. 201, pp. 1–6, 2002.

[9] Cigré Working Group A3.06, *Final Report of the 2004 - 2007 International Enquiry on Reliability of High Voltage Equipment - Part 1 - Summary and General Matters*, Vol. 513, 2012.

[10] F. H. Kreuger, "Partial Discharge Detection in High-voltage Equipment." Butterworths, the University of Michigan, pp. 1–14, 1989.

[11] IEEE Power & Energy Society, *IEEE Standard Terminology for Power and Distribution Transformers*. 2010.

[12] L. Niemeyer, L. Ullrich, and N. Wiegart, "The Mechanism of Leader Breakdown in Electronegative Gases," *IEEE Trans. Electr. Insul.*, Vol. 24, No. 2, pp. 309–324, 1989.

[13] A. Chachereau and S. Pancheshnyi, "Calculation of the effective ionization rate in air by considering electron detachment from negative ions," *IEEE Trans. Plasma Sci.*, Vol. 42, No. 10, pp. 3328–3338, 2014.

[14] M. H. Shinya Ohtsuka, Takashi Teshima, Satoshi Matsumoto, "部分放電検出に基づく電力機器の絶縁診断に関する考え方," 電気学会全国大会講演論文集, No. 6, pp. 351–352, 2006.

[15] J. Kuffel, E., Zaengl, W. S., and Kuffel, "High Voltage Engineering: Fundamentals," in *Springer Handbooks*, Butterworth-Heinemann, 2000, pp. 367–394.

[16] The British Standard Institution, "High-voltage test techniques - Partial discharge measurements," *BS EN 602702015, Br. Stand. Committees*, 2015.

[17] IEEE Power and Energy Society, *IEEE Approved Draft Guide for the Interpretation of Gases Generated in Oil-Immersed Transformers*. IEEE PC57.104/D6.2, 2019.

[18] R. J. Van Brunt and J. T. Herron, "Fundamental Processes of SF6 Decomposition and Oxidation in Glow and Corona Discharges," *IEEE Trans. Electr. Insul.*, Vol. 25, No. 1, pp. 75–94, 1990.

[19] L. E. Lundgaard, "Partial Discharge - Part XIII: Acoustic Partial Discharge Detection -Fundamental Considerations," *IEEE Electr. Insul. Mag.*, Vol. 8, No. 4, pp. 25–31, 1992.

[20] R. Meunier and G. H. Vaillancourt, "Propagation behaviour of acoustic partial discharge signals in oil-filled transformers," *IEEE Int. Conf. Conduct. Break. Dielectr. Liq. ICDL*, pp. 401–404, 1996.

[21] IEEE Power and Energy Society, *IEEE Guide for the Detection, Location and Interpretation of Sources of Acoustic Emissions from Electrical Discharges in Power Transformers and Power Reactors*. IEEE Std C57.127-2018 (Revision of IEEE Std C57.127-2007), 2019.

[22] S. M. Markalous, S. Tenbohlen, and K. Feser, "Detection and location of partial discharges in power transformers using acoustic and electromagnetic signals," *IEEE Trans. Dielectr. Electr. Insul.*, Vol. 15, No. 6, pp. 1576–1583, 2008.

[23] M. Muhr and R. Schwarz, "Experience with optical partial discharge detection," *Mater. Sci. Pol.*, Vol. 27, No. 4, pp. 1139–1146, 2009.

[24] S. Biswas, C. Koley, B. Chatterjee, and S. Chakravorti, "A methodology for identification and localization of Partial Discharge sources using optical sensors," *IEEE Trans. Dielectr. Electr. Insul.*, Vol. 19, No. 1, pp. 18–28, 2012.

[25] B. F. Hampton and R. J. Meats, "Diagnostic Measurements At Uhf in Gas Insulated Substations.," *IEE Proc. C Gener. Transm. Distrib.*, Vol. 135, No. 2, pp. 137–144, 1988.

[26] X. Han, J. Li, L. Zhang, P. Pang, and S. Shen, "A Novel PD Detection Technique for Use in GIS Based on a Combination of UHF and Optical Sensors," *IEEE Trans. Instrum. Meas.*, Vol. 68, No. 8, pp. 2890–2897, 2019.

[27] S. Kaneko, S. Okabe, M. Yoshimura, H. Muto, C. Nishida, and M. Kamei, "Detecting characteristics of various type antennas on partial discharge electromagnetic wave radiating through insulating spacer in gas insulated switchgear," *IEEE Trans. Dielectr. Electr. Insul.*, Vol. 16, No. 5, pp. 1462–1472, 2009.

[28] A. M. Ishak, M. T. Ishak, M. T. Jusoh, S. F. Syed Dardin, and M. D. Judd, "Design and Optimization of UHF Partial Discharge Sensors Using FDTD Modeling," *IEEE Sens. J.*, Vol. 17, No. 1, pp. 127–133, 2017.

[29] T. Li, M. Rong, C. Zheng, and X. Wang, "Development simulation and experiment study on UHF partial discharge sensor in GIS," *IEEE Trans. Dielectr. Electr. Insul.*, Vol. 19, No. 4, pp. 1421–1430, 2012.

[30] C. Zachariades, R. Shuttleworth, R. Giussani, and T. H. Loh, "A Wideband spiral UHF coupler with tuning nodules for partial discharge detection," *IEEE Trans. Power Deliv.*, Vol. 34, No. 4, pp. 1300–1308, 2019.

[31] X. Chen, Y. Qian, G. Sheng, and X. Jiang, "A time-domain characterization method for UHF partial discharge sensors," *IEEE Trans. Dielectr. Electr. Insul.*, Vol. 24, No. 1, pp. 110–119, 2017.

[32] K. Khotimah, U. Khayam, Suwarno, Y. Tai, M. Kozako, and M. Hikita, "Design of dipole antenna model for partial discharge detection in GIS," *Proc. - 5th Int. Conf. Electr. Eng. Informatics Bridg. Knowl. between Acad. Ind. Community, ICEEI 2015*, pp. 186–191, 2015.

[33] H. F. Ye, Q. Yong, D. Yue, G. H. Sheng, and X. C. Jiang, "Development of multi-band ultra-high-frequency sensor for partial discharge monitoring based on the meandering technique," *IET Sci. Meas. Technol.*, Vol. 8, No. 5, pp. 327–335, 2014.

[34] T. Hoshino, K. Nojima, and M. Hanai, "Real-time PD identification in diagnosis of GIS using symmetric and asymmetric UHF sensors," *IEEE Trans. Power Deliv.*, Vol. 19, No. 3, pp. 1072–1077, 2004.

[35] L. Chen, C. Xiaoxin, S. Xianjun, and X. Hua, "Present Situation and Development of Internal Sensors for Ultra-high Frequency Detection in Gas Insulated Switchgear," *J. Phys. Conf. Ser.*, Vol. 1659, No. 1, 2020.

[36] B. Sarkar, D. K. Mishra, C. Koley, and N. K. Roy, "Microstrip patch antenna based UHF sensor for detection of Partial Discharge in High Voltage electrical equipments," *11th IEEE India Conf. Emerg. Trends Innov. Technol. INDICON 2014*, 2015.

[37] F. Bin, F. Wang, Q. Sun, S. Lin, Y. Xie, and M. Fan, "Internal UHF antenna for partial discharge detection in GIS," *IET Microwaves, Antennas Propag.*, Vol. 12, No. 14, pp. 2184–2190, 2018.

[38] G. V. R. Xavier, A. C. De Oliveira, A. D. C. Silva, L. A. M. M. Nobrega, E. G. Da Costa, and A. J. R. Serres, "Application of Time Difference of Arrival Methods in the Localization of Partial Discharge Sources Detected Using Bio-Inspired UHF Sensors," *IEEE Sens. J.*, Vol. 21, No. 2, pp. 1947–1956, 2021.

[39] E. H. Plant, P. J. Moore, S. Member, I. E. Portugues, and I. A. Glover, "Radiometric Location of Partial Discharge Sources," Vol. 20, No. 3, pp. 2264–2272, 2005.

[40] E. M. Amin and N. C. Karmakar, "A passive RF sensor for detecting simultaneous partial discharge signals using time-frequency analysis," *IEEE Sens. J.*, Vol. 16, No. 8, pp. 2339–2348, 2016.

[41] T. Bandi and S. Ohtsuka, "A Multiple Narrow Band Antenna for Detection of Discharge-Emitted Electromagnetic Waves for Insulation Diagnostic," *IEEJ Trans. Electr. Electron. Eng.*, Vol. 15, No. 12, pp. 1751–1757, 2020.

[42] T. Bandi, M. Tanaka, H. Furuie, and S. Ohtsuka, "Developing of Multiple-narrowband Antenna to Detect Partial Discharge-emitted Signal under Radio Communication Noise Environment," *Proceeding - 8th Int. Conf. Cond. Monit. Diagnosis, C. 2020*, pp. 154–157, 2020.

[43] T. Bandi and S. Ohtsuka, "Partial Discharge Detection of Multiple-Narrow Band Antenna under the Radio Communication Noise," *IEEJ Trans. Electr. Electron. Eng.*, Vol. 16, No. 5, pp. 715–721, 2021.

Chapter 2

Experimental Setup and Procedure

2.1 Introduction

As described in Chapter 1, the aim of this study is to design, develop, and evaluate the novel wideband UHF sensor, which has a high sensitivity for partial discharge (PD) detection and noise resistance ability for communication and ISM frequency bands. This chapter explains the following topics in detail: (i) a simulation and a test setup for UHF sensor design, (ii) PD experimental setup to assess PD detection ability of UHF sensor (iii) noise emission sources to evaluate noise resistance ability of UHF sensor and (iv) the environment condition and devices used in this research.

2.2 Antenna simulation and test setup

2.2.1 Antenna simulation setup

The proposed UHF sensor is simulated by COMSOL Multiphysics software [1], RF module, releasing on the finite element method, specifically the frequency domain form of Maxwell's equations, to evaluate the initial and boundary conditions. In this research, the *Electromagnetic Waves, Frequency Domain interface* was used to solve the time-harmonic wave equation for the electric field:

$$\nabla \times (\mu_r^{-1} \nabla \times E) - k_0^2 \varepsilon_r E = 0 \qquad (2.1)$$

where E is the electric field, ε_r is the relative permittivity, ε_0 is the permittivity of a vacuum, μ_r is the relative permeability, σ is the electrical conductivity and k_0 is the wavenumbers of free space. The equation solves the electric field, E, at the operating frequency. Other inputs are the material properties and can be fitted for simulation conditions. This study used the FR-4, glass-reinforced epoxy laminate material as a substrate. Table 2.1 presents the material properties used for the simulation.

Table 2.1. Material properties used for sensor simulation

Component	Material	Conductivity (S/m)	Relative permittivity	Relative permeability
PCB substrate	FR-4	0.004	4.5	1.0
Enclosing domain	Air	0	1.0	1.0

The Perfect Electric Conductor (PEC) boundary condition is used to design the metallic radiation and ground parts, including the microstrip feeding transmission lines [2]. This boundary condition sets the tangential component of the electric field to zero, as shown in Equation 2.2. It is used to model a lossless metallic surface (for example, a ground part) or a symmetry-type boundary condition. It imposes symmetry for magnetic fields and "magnetic currents" and antisymmetric for electric fields and electric currents. It supports induced electric surface currents, and thus any prescribed or induced electric currents (volume, surface, or edge currents) flowing into a perfect electric conductor boundary is automatically balanced by induced surface currents.

$$\mathrm{n} \times E = 0 \qquad (2.2)$$

The sensor's simulation needs the non-reflection boundaries far away from the source. However, it is impossible to make a large infinity model. RF module suggests two methods to make a non-reflection simulation area; Perfect Matching Layers (PML) and Scattering Boundary Condition (SBC) [3]. The PML is a high-quality approach for radiation absorbing, but the PML uses more memory than the SBC. In this study, to decrease the calculation size and reduce the simulation time, the SBC was used to model a small region around the sensor without reflection, as shown in Fig. 2.1. According to Equation 2.3, it is non-reflection if incident radiation is exactly normally incident to the boundary. In another case, an incident upon the SBC at a non-normal incidence is slightly reflected. This study used a spherical-shaped SBC domain with a 250 mm radius.

$$\mathrm{n} \times (\nabla E) + ik_0 E = 0 \qquad (2.3)$$
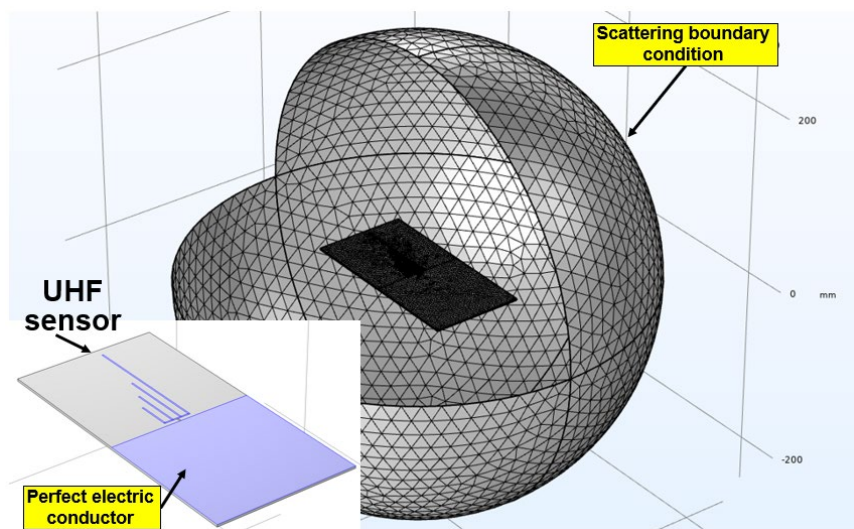
Fig. 2.1. Simulation design for UHF sensor

The *Lumped port* (Coaxial and uniform type) function was used for feeding. This function sets the coaxial feed cable to operate in the Transverse Electro-Magnetic (TEM) mode. The characteristic impedance of the port was set to 50 Ω, which matches that of the SubMiniature version A (SMA) type connector. The mesh discretization was performed automatically by COMSOL using the physics-controlled mesh option. This option optimizes the mesh size based on frequency, i.e., the size and elements number of mesh is adjusted automatically when the frequency changes. As a result, the memory requirements and the computation time for the simulation are minimized since the optimal size of elements is selected for each frequency step. Table 2.2 shows the mesh parameters used in this study.

Table 2.2. Mesh parameters used for antenna simulation

Parameters Antennas	Number of elements	Minimum element size (mm)	Average element size (mm)
Single strip antenna	228,471	0.1924	0.6517
MNB antenna	169,388	0.1828	0.6484
FMNB antenna	211,681	0.1546	0.6544

The simulation performed in the range 0.1~3.0 GHz in 10 MHz steps for the UHF method and estimates the main parameters for UHF sensor performance, such as reflection loss, radiation pattern, input impedance, electric field distribution, and so on. The environment temperature and pressure were fixed as 20ºC and 1 MPa in simulation. The initial optimization process achieved a reflection loss (S11 parameter) lower and higher than -6 dB at detection frequency and elimination frequency, respectively. The reflection loss of -6 dB (around 25% of power reflected) was considered a reasonable reference level to noise elimination ability. The simulation was repeated with a different value for one parameter when other parameters were fixed as an iterative approach to investigate the effect of physical dimensions on antenna performance.

In addition, there are some research works for developing UHF sensors for PD detection using COMSOL software [4-5].

2.2.2 Antenna test setup

After receiving an acceptable simulation result, the MNB antenna was fabricated by CNC 3018 mini PCB engraving machine, whose programable resolution is 0.06 mm. The fabricated MNB antenna was calibrated based on the following measurements:

- Reflection loss measurement (S11)
- Transfer function measurement (S21)

- Antenna factor measurement (AF)

- Radiation pattern measurement (RP)

Table 2.3 shows the list of equipment which used for the antenna test. The standard wideband antennas (HA, BBHA9120A, and BiConiLog, Model 3142E) were used for comparison purposes. The standard Horn Antenna (HA) is used to reference antenna for antenna test measurement because of flat and wideband detection characteristics, and Fig. 2.2 shows the reflection loss of HA. The network analyzer (TTR506 A) was used to measure the antenna's reflection loss, transfer function, and antenna factor. The oscilloscope (RTO1044, 10 GS/s) is used for radiation pattern measurement.

Table 2.3. Measurement devices used for antenna calibration

#	Device name	Type	Frequency range	Used for
1	Horn antenna	BBHA 9120 A	0.8 GHz ~ 10 GHz	S11, S21
2	BiConiLog antenna	Model 3142E	30 MHz ~ 6 GHz	S11, S21
3	Network analyzer	TTR506 A	100 kHz ~ 6 GHz	S11, S21, AF
4	Oscilloscope	RTO1044, 10 GS/s	Up to 4 GHz	RP
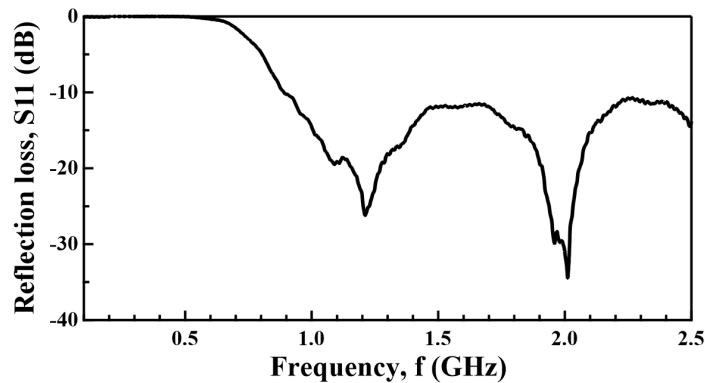
Fig. 2.2. Reflection loss of standard Horn Antenna

The experiment setup used to measure the reflection loss and the transfer function is shown in Fig. 2.3. The distance (d) between antennas was selected as 1m to satisfy the far-field regions of detection frequency of both antennas used in the experiment. The antennas' directions exactly matched the front side of the antennas. Table 2.4 shows the Network Analyzer (NA) setup, calibrated before every measurement using OSLT 3.5mm BN533828 calibration kit.

Table 2.4. Setup of the network analyzer for antenna calibration

#	Device name	Type
1	Frequency range	100 kHz ~ 3 GHz
2	Measurement points	1500
3	Power level	10 dBm
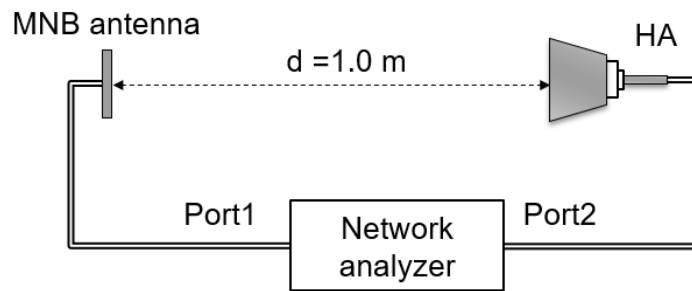
Fig. 2.3. The antenna test setup for reflection loss and transfer function measurements

The antenna factor (AF) is one of the important parameters for receiver antennas to calculate a received electric field strength from received power. There are two acceptable methods to measure the AF; the reference antenna method and three antennas (or standard site) methods [6-7]. The three-antenna method was used in this study because of not need the reference antenna. In the three-antenna method, three measurement results are collected using transmit/receive (Tx/Rx) pairs of three antennas with identical setups. Then, three unknown AFs are calculated from system equations of three measurement results.

In this study, first, three identical HA were calibrated, and measurement results were compared with the factory datasheets value [8] of antennas to validate the AF calibration setup. Fig. 2.4 shows the AF measurement setup, and the calculated AFs of three identical HA are shown in Fig. 2.5 compared with the datasheet's value. The difference between measurement and datasheet values was around 1.5 dB/m and almost constant. The identical HA's measurement results agreed well with each other and have a similar trend with datasheet value, which means this method can be used to evaluate the AF measurement. Therefore, the same measurement setup is used for antenna factor measurement of proposed MNB antennas. The radiation pattern measurement is discussed next section because it was performed based on breakdown discharge detection.
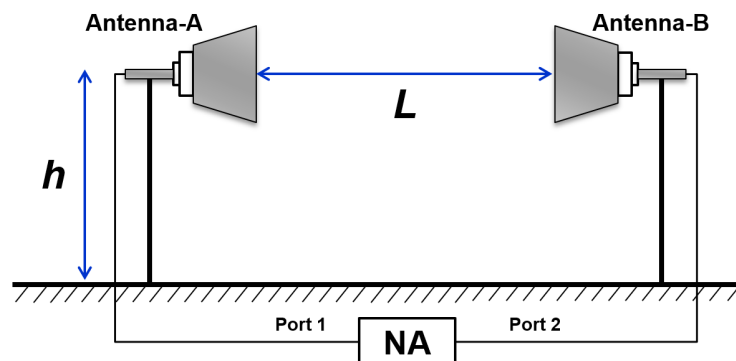
Fig. 2.4. Arrangement of AF measurement
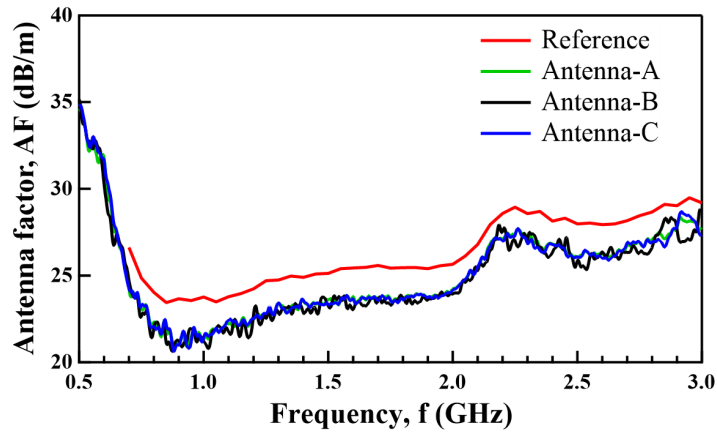
Fig. 2.5. AF measurement results compared with reference value when identical three HA were used.

2.3   Discharge Detection Setup

The proposed MNB antenna was applied to discharge measurement to investigate the discharge detection ability, and the measurement result was compared with standard HA. All experiments were performed in the noise reduction anechoic room, as shown in Fig. 2.6. The background noise condition is shown in Fig. 2.7. The background noise amplitude and intensity were under 5 mV and -75 dBm, respectively. The environmental condition was relatively constant during the measurement because of the anechoic room. Table 2.5 shows the environmental condition measured during each discharge measurements.

Table 2.5. Environment condition of partial discharge measurement

#	Parameter	PD in air	PD in SF$_6$	PD in XLPE
1	Temperature ($^{\circ}$C)	23.9	25.5	26
2	Humidity (%)	61.4	38.8	39.5

Fig. 2.6.   The anechoic room used for the experiment

(a) Time domain   (b) Frequency domain
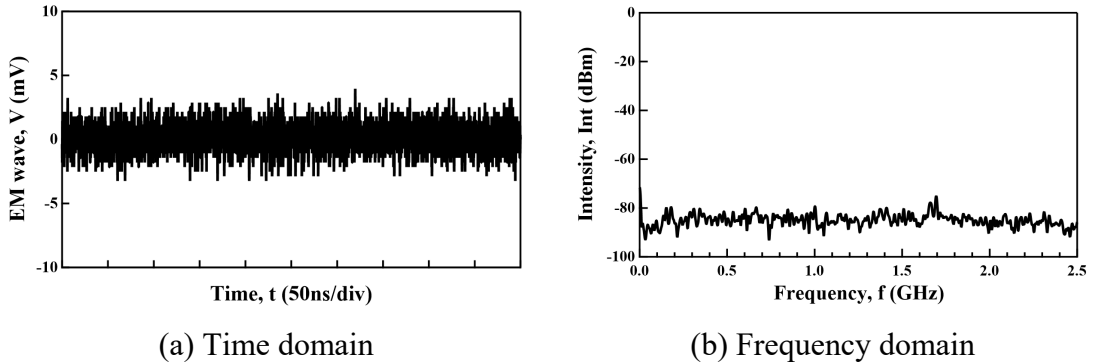
Fig. 2.7. Background noise measurement

The needle-plate electrode system was used as a discharge source in this study. The following discharge sources were used to evaluate the discharge detection characteristic:

1. Breakdown discharge in air
2. Partial discharge in SF_6
3. Partial discharge in dry air
4. Partial discharge in XLPE insulation

Table 2.6 shows the devices list used in the discharge measurement setup. The pre-amplifier is used to increase the amplitude of partial discharge, while the attenuator is used to measure PD current to protect the measurement device.

Table 2.6. Measurement devices used for discharge measurement

#	Device name	Type	Main parameter	Used for
1	HV-source	Special design	±4.1 kV, DC	BD source
2	HV-amplifier	Trek, Model 20/20C	20 kV peak AC	PD source
3	Limiting resistor	-	50 kΩ	PD source
4	Function generator	Tektronix, AFG3102	10 Vpp, 100 MHz	PD source
5	Oscilloscope	LeCroy, 104Xi-A	1GHz, 10 GS/s	PD source
6	Horn antenna	Schwarzbeck, BBHA 9120A	0.8 GHz ~ 10 GHz	Measurement
7	Preamplifier	R&K, AA220	25 dB	Measurement
8	Attenuator	Anritsu, 41KC-20	20 dB	Measurement
9	Oscilloscope	Tektronix, DPO7254C	2.5 GHz, 40 GS/s	Measurement
10	Oscilloscope	R&S, RTO1044	4 GHz, 40 GS/s	Measurement

2.3.1 Breakdown discharge measurement setup

First, the proposed MNB antennas were applied to breakdown discharge (BD) measurement because the BD phenomena have high amplitude and are more easily detected than PD phenomena. The measurement result was compared with simultaneously measured HA's result and experiment setup as shown in Fig 2.8 [9]. The HA was used to define the original characteristic of the discharge emitted signal except

for the reference antenna's role. The BD signal was emitted from the HV source and needle-plate electrodes with a 0.5 mm gap, as shown in Fig. 2.9.
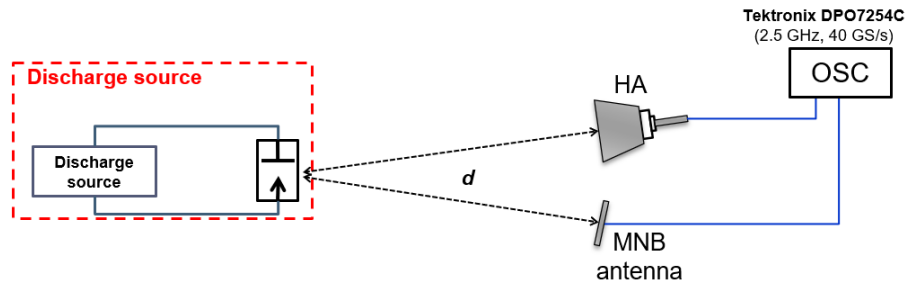
Fig. 2.8. BD measurement experiment setup
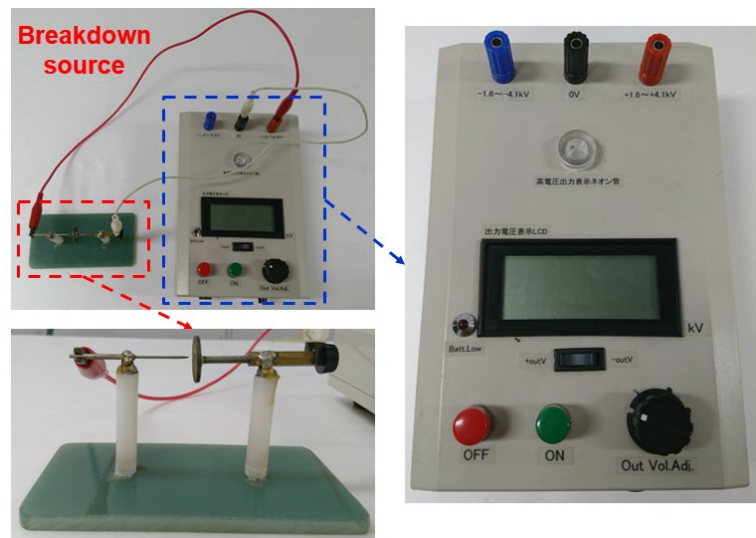
Fig. 2.9. Needle-plate electrode representing BD source

In addition, the BD measurement was used to evaluate the radiation pattern of the proposed MNB antenna. The MNB antenna was applied to detect BD signal with six different positions, as shown in Fig. 2.10 when the BD source position was fixed. Then, measured results compared each other and the result of HA as a reference value.
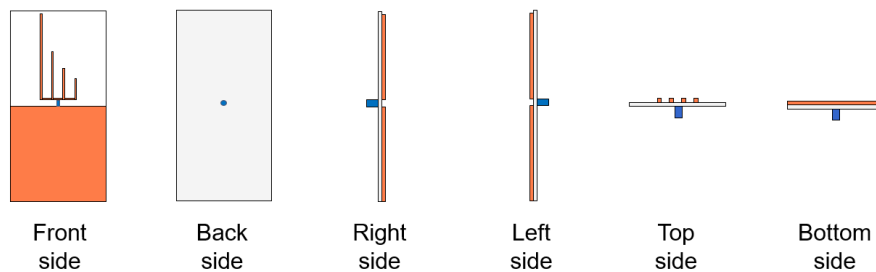
Fig. 2.10. The position of MNB antenna for radiation pattern measurement

2.3.2 Partial discharge in a gas insulation measurement setup

The many types of gas insulation materials are used for HV equipment. The dry air and SF_6 gas were used as a dielectric gas medium for the PD source in this study [9-10]. The atmospheric air is a natural dielectric material, while the SF_6 gas is commonly used in high voltage equipment as a gas insulation medium because of its high dielectric strength.

Before the PD measurement, the BD inception voltage for each insulation for safety purposes. Then, applied high voltage was selected as 20 kV peak and 12 kV peak for SF_6 gas and dry air, respectively. Fig. 2.11 shows the PD in the gas insulation measurement setup. PD source was represented a needle-plate electrode system in the acrylic chamber filled by gas insulation at 0.1 MPa. The needle electrode used for the PD experiment are shown in Fig. 2.12, and Table 2.7 shows the needle size.

Table 2.7. Measurement condition and needle size

#	Parameters	Dry air	SF_6
1	Radius of curvature (μm)	50.6	77.3
2	Gap length, g (mm)	15	13
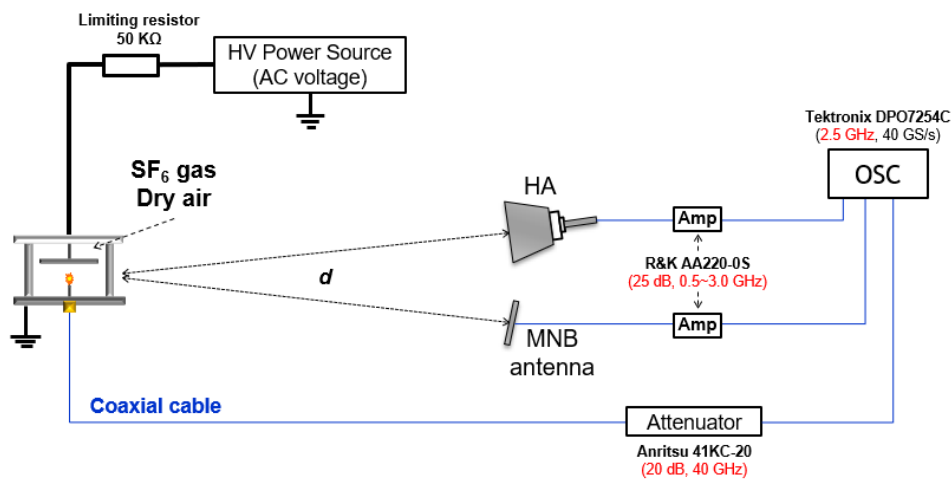
Fig. 2.11. PD in the gas insulation measurement setup
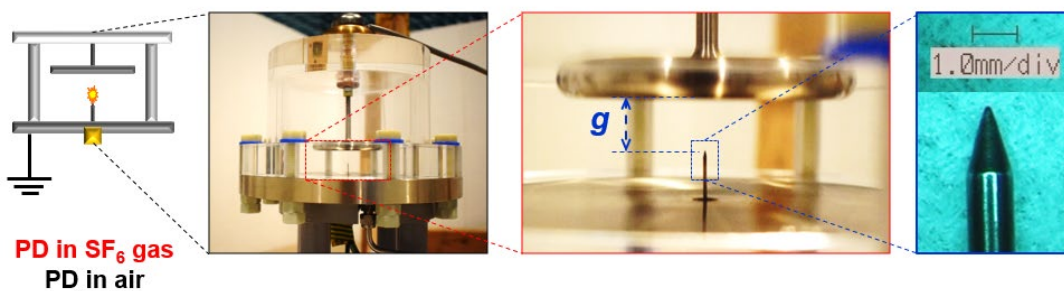
Fig. 2.12. Needle electrode used PD source

The PD emitted EM waves are simultaneously acquired by HA and MNB antennas, which were identically connected to the digital oscilloscope through 50 Ω coaxial cable and 25 dB pre-amplifier to increase the amplitude of the PD signal. The frequency range of the pre-amplifier was 0.5 GHz ~ 3.0 GHz, crossing to the frequency band of the UHF method. Also, the PD current was measured through the needle electrode, coaxial cable, and 20 dB attenuate by the oscilloscope for comparison purposes.

2.3.3 PD in XLPE insulation measurement setup

Fig. 2.13 shows the experiment setup of PD in XLPE insulation. PD source was represented as metal protrusion mounted in the XLPE insulation as shown in Fig. 2.14. This practical defect sample was made by Sumitomo electrical industries in Japan. The XLPE insulation material and making way are high identity with real XLPE insulated power cable.
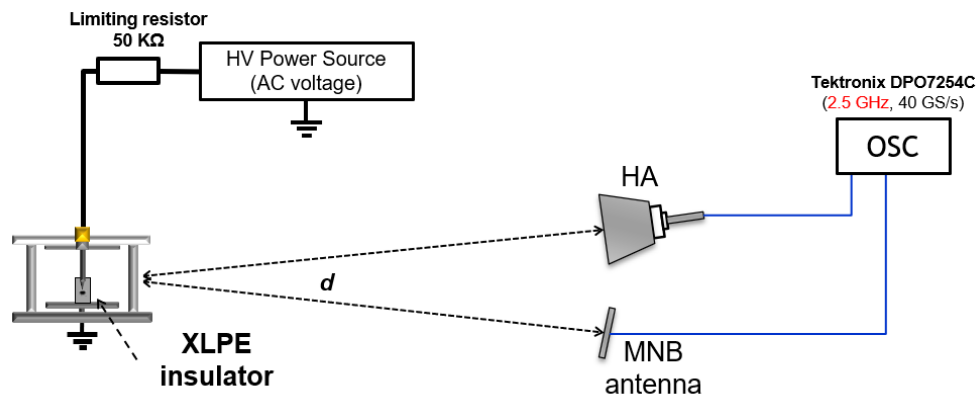
Fig. 2.13. PD in XLPE insulation measurement setup
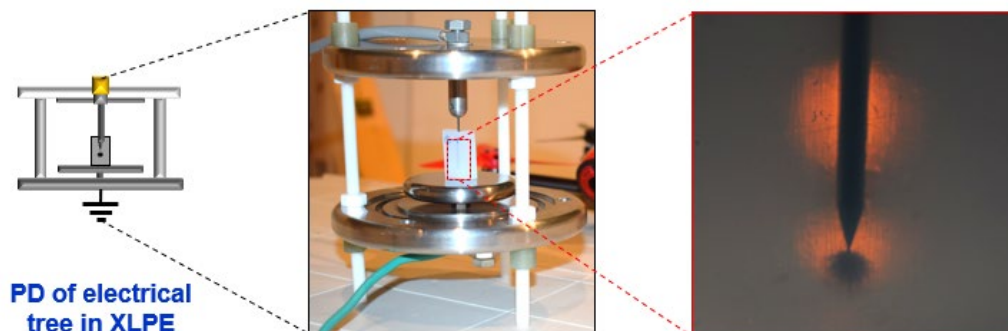
Fig. 2.14. Practical defect sample made with a metal protrusion in XLPE

The PD current and pre-amplifier were not used in this experiment to prevent the breakdown, which grows the electric tree of the defect sample. The applied high voltage was 7 kV, satisfying the non-growing electric tree in XLPE insulation. UHF sensors were

located 1 meter from the PD source and simultaneously measured the PD-emitted EM wave.

2.4   Noise source and measurement setup

The main advantage of the MNB antenna is its noise elimination ability. The MNB antenna was applied to measure the noise to evaluate noise reduction. This study used two different noise sources: artificial and real Wi-Fi noises.

2.4.1 Artificial noise source and experiment setup

Fig. 2.15 shows the PD in SF_6 gas under the artificial noise experiment setup. The PD source and measurement system were similar to previous sections 2.3.2. The artificial noise was emitted from the signal generator (SG, Rohde&Schwarz, SMA100A) through standard HA (Schwarzbeck, BBHA 9120A), the same as the receiver antenna. The noise transmitted antenna was located 1 and 2 meters from PD source and receiver antennas, respectively [12].
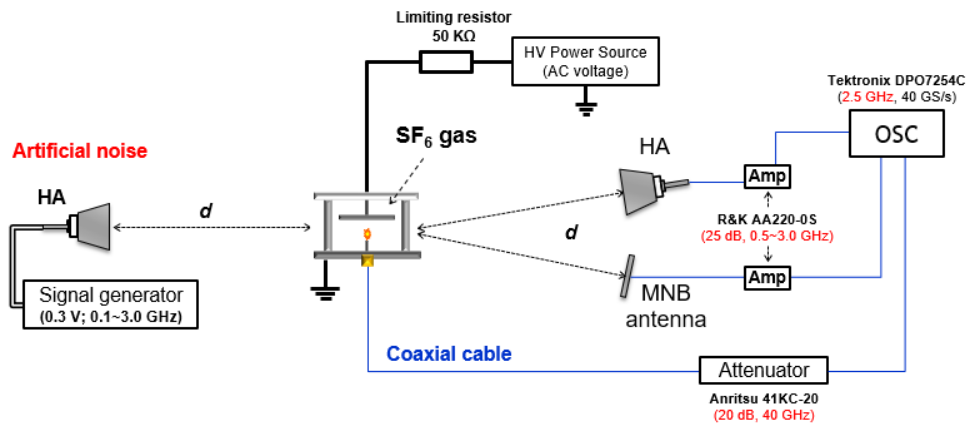
Fig. 2.15. PD in SF_6 gas measurement setup under artificial noise
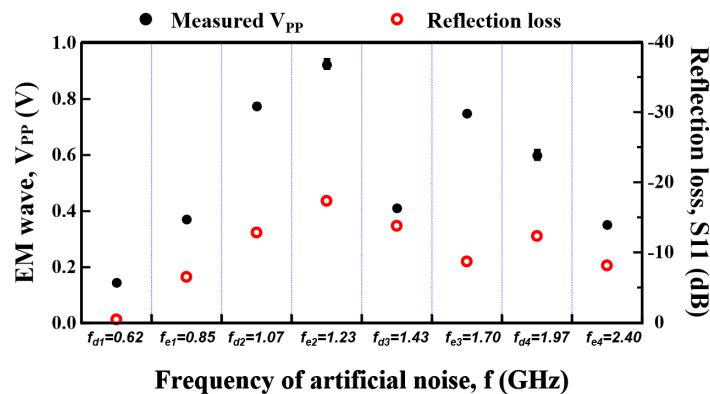
Fig. 2.16. Measured V_{PP} compared with reflection loss of receiver HA.

The artificial noise frequency was selected based on the operation frequency of the proposed MNB antenna as four elimination and four detection frequencies. The amplitude of SG was fixed as 300 mV. Fig. 2.16 shows the measured V_{PP} of receiver HA and compared with reflection loss of it. The received V_{PP} is directly related to the receiver antenna's reflection loss.

2.4.2 Actual Wi-Fi noise source and experiment setup

Fig. 2.17 shows the PD in SF_6 gas under the Wi-Fi noise experiment setup. The Wi-Fi noise is emitted from an unmanned aerial vehicle (Phantom-4, commercial drone). The drone was located in 3.5 and 4.5 meters from PD source and receiver antennas [13]. Phantom-4 drone operates at a 2.4 GHz frequency band, and the operating channel is automatically changed based on the environmental condition. Fig. 2.18 shows the measured EM waveform and frequency spectrum of receiver HA. The average V_{PP} was 815 mV, and the intensity was around -17.7 dBm at 2.45 GHz.
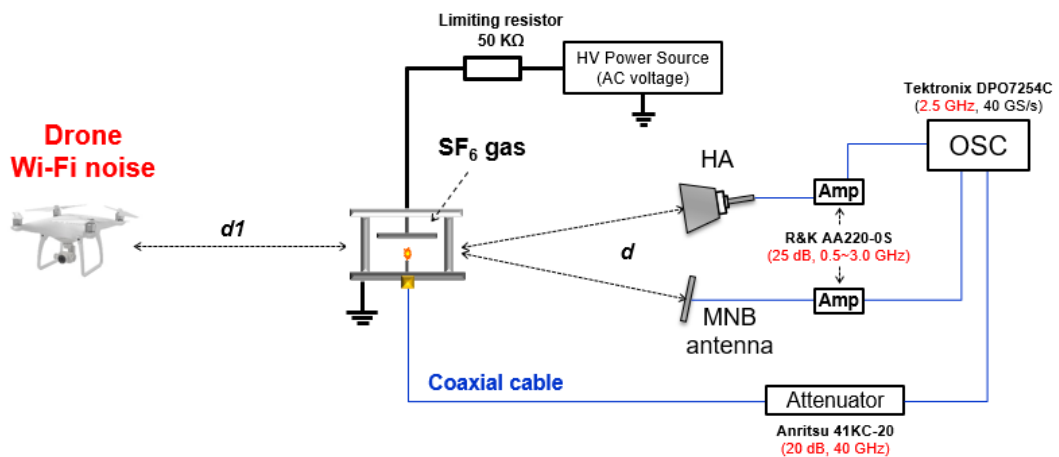
Fig. 2.17. PD in SF_6 gas measurement setup under Wi-Fi noise

(a) EM wave   (b) Frequency spectrum
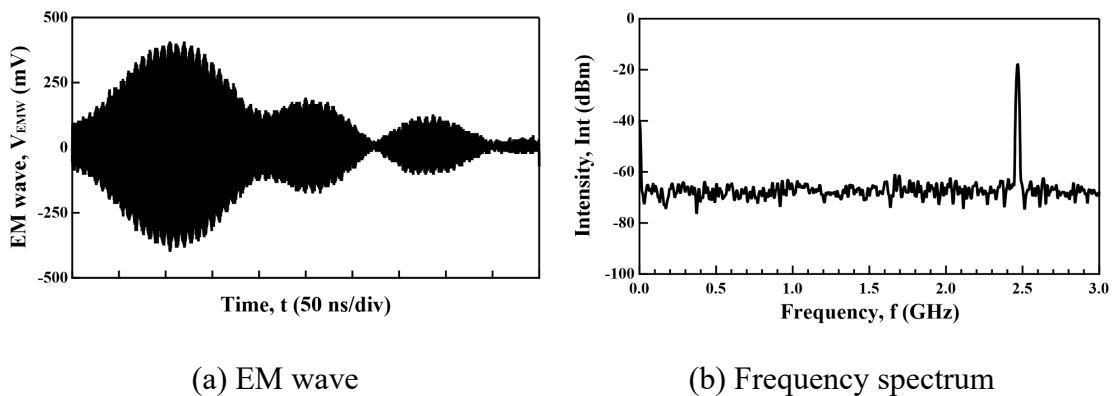
Fig. 2.18. Wi-Fi noise emitted from the commercial drone (Phantom-4)

References

[1]   COMSOL AB, "COMSOL Multiphysics®, v. 5.6. www.comsol.com." Stockholm, Sweden.

[2]   W. Frei, "Modeling of Materials in Wave Electromagnetics Problems." COMSOL Blog, 2015.

[3]   W. Frei, "Using Perfectly Matched Layers and Scattering Boundary Conditions for Wave Electromagnetics Problems." COMSOL Blog, 2015.

[4]   C. Zachariades, R. Shuttleworth, R. Giussani, and T. H. Loh, "A Wideband spiral UHF coupler with tuning nodules for partial discharge detection," *IEEE Trans. Power Deliv.*, Vol. 34, No. 4, pp. 1300–1308, 2019.

[5]   C. Zachariades, R. Shuttleworth, and R. Giussani, "A Dual-Slot Barrier Sensor for Partial Discharge Detection in Gas-Insulated Equipment," *IEEE Sens. J.*, Vol. 20, No. 2, pp. 860–867, 2020.

[6]   J. Wout and M. Luc, "An improved method to determine the antenna factor," *IEEE Trans. Instrum. Meas.*, Vol. 54, No. 1, pp. 252–257, 2005.

[7]   A. A. Smith, "Standard-Site Method for Determining Antenna Factors," *IEEE Trans. Electromagn. Compat.*, Vol. EMC-24, No. 3, pp. 316–322, 1982.

[8]   Schwarzbeck Mess-Electronik, "Datasheet: Double Ridged Broadband Horn Antenna, BBHA 9120 A."

[9]   T. Bandi and S. Ohtsuka, "A Multiple Narrow Band Antenna for Detection of Discharge-Emitted Electromagnetic Waves for Insulation Diagnostic," *IEEJ Trans. Electr. Electron. Eng.*, Vol. 15, No. 12, pp. 1751–1757, 2020.

[10]   T. Bandi and S. Ohtsuka, "Partial Discharge Detection of Multiple-Narrow Band Antenna under the Radio Communication Noise," *IEEJ Trans. Electr. Electron. Eng.*, Vol. 16, No. 5, pp. 715–721, 2021.

[11]   T. Bandi and S. Ohtsuka, "Application of MNB antenna for Discriminating between Partial Discharges in Dry Air and SF 6 Gas," in *The 73rd Joint Conference of Electrical, Electronics and Information Engineers in Kyushu*, 2020, Vol. 2020 02–2P, p. 366, 2020.

[12]   T. Bandi, M. Tanaka, H. Furuie, and S. Ohtsuka, "Developing of Multiple-narrowband Antenna to Detect Partial Discharge-emitted Signal under Radio Communication Noise Environment," *Proceeding - 8th Int. Conf. Cond. Monit.*

Diagnosis, C. 2020, pp. 154–157, 2020.

[13] T. Bandi and S. Ohtsuka, "Application of Microstrip Filter for Multiple Narrow Band Antenna to Detection of Partial Discharge," in *The 22nd International Symposium on High Voltage Engineering, 2021*, pp. 1–5.

Chapter 3
Design of a Novel UHF Sensor for PD Detection

3.1 Introduction

As described in Chapter 1, the main part of the ultra-high frequency (UHF) method is sensors which are installed on the high voltage (HV) equipment without direct connection to the HV circuit and are able to detect the EM wave emitted from partial discharge (PD) activity in safety and on-line operation mode. The UHF antennas are commonly used as UHF sensors in the PD detection and monitoring field. Due to rapidly developed communication and digital technology, multiple-band antennas are required to detect PD signals with high sensitivity and without communication noise interference.

There are very few attempts to develop the multiple-band antenna for the PD detection field. In [1], the meandering printed loop antenna is introduced as a multiple-band antenna for PD detection in transformer oil. The loop, dipole, and monopole types antennas have a high-order resonant characteristic, which gives an ability to detect multiple resonant frequencies. However, these multi resonance bands are just high-order oscillations of the first resonant frequency of the antenna, and it is impossible to adjust the resonant frequencies independently from each other.

In addition, the wideband antenna with a number of cascaded resonators for signifying the identification data of PD emitted signal was suggested in [2]. The cascaded resonators operate as bandstop filters and attenuate certain frequencies, and this method is useful for detecting multiple band signals. However, adding the passive resonators increases the sensor's size, connection loss, and the vulnerability of the diagnostic system.

This chapter describes the requirements of a UHF sensor and how to design and fabricate the novel multiple narrow bands (MNB) antenna for PD detection under high communication noise conditions as a wideband UHF sensor with high noise resistance. In addition, the MNB antenna's physical parameters are optimized. The important antenna parameters are shown based on experimental results compared with theoretical performance obtained by the COMSOL simulation software.

3.2   Requirements and Development Method

3.2.1   Requirements of UHF PD sensor

The UHF sensor is actively studied for PD detection in all types of HV equipment since the UHF method was proposed for diagnostic measurements in gas-insulated substations (GIS) by B. F. Hampton [3]. The UHF sensor for insulation diagnosis should satisfy the following requirements.

- **A highly sensitivity**: The operation frequency band of the UHF sensor is required to match the entire emission frequency band of the PD signal and the wider bandwidth as possible to increase the sensitivity of PD detection. According to the IEC TS 62478 standard [4], the measurable spectrum in the UHF band should be high or comparable to the spectrum of a moving particle with a discharge level of 5 pC.

- **Noise elimination**: Due to rapidly developed wireless communication, the PD signal could be masked by UHF environment noise. Therefore, UHF sensors need noise resistance ability [5].

- **The flat and compact size for simple installation**: The UHF sensor should not affect the insulation distance between high voltage conductors and grounded flange when installed in high voltage equipment. Also, the electric field detection is more comfortable than the magnetic field sensor due to installation difficulties.

- **Low cost**: A complex monitoring system can be performed using multiple UHF sensors. Therefore, UHF sensors are highly required to reduce the production and mounting cost depending on the practical application.

- **Wide area detection**: In order to investigate the PD signal coming from an unknown location, omnidirectional radiation property is needed to catch the signal from all sides of the sensor [6]. The receiving time and amplitude difference between multi-sensor allow an investigation of PD location and on-line monitoring.

The above requirements clearly show that the multiple-narrow band, a flat printed and omnidirectional antenna is suitable for UHF sensor because it can be a solution to satisfy the high sensitivity of the PD detection in parallel with noise resistance.

In addition, the EM wave emitted from PD activity is changed depending on PD type and signal propagation. Therefore, a simple adjustable structure is good for UHF sensors for different PD detection and noise environments. Also, the cooperation with digital and

ICT technology gives a big advantage for UHF sensors such as IoT and AI technology to develop complex diagnostic systems.

From the above summary, it seems that the PD detection field needs a UHF sensor with (i) multiple-narrow band resonant frequencies, (ii) high noise resistance, (iii) omnidirectional radiation characteristics, (iv) printed flat structure and (v) electric field detection ability.

3.2.2 Approaches to achieving MNB antenna

The multiple-band antennas are widely used in the communication field to transfer EM signals, such as double band and triple-band antennas. However, a typical multi-band antenna, a composite structure of narrowband resonant components, has great design difficulties because of the sophisticated structure and extremely sensitive impedance bandwidth [7]. Two methods can be used to develop multiple-band antennas.

- Notching method: Wang-Sang Lee and others introduced a multiple band-notched antenna system developed by adding the narrow frequency notch band in the printed wideband monopole antenna [8]. The notching element works the same as the narrow bandstop filter. Fig. 3.1 shows the concept of a multiple band-notched antenna system. The notching method is compact and can eliminate the frequency band with a narrowband. It means the detection frequency band could be much wide. However, the notching elements could interfere each other due to mutual coupling and inductance. As a result, the design and adjustment of resonant and elimination frequencies will be difficult. Also, the notching elements' number and the antenna size are increased when the number of elimination frequencies is increased.
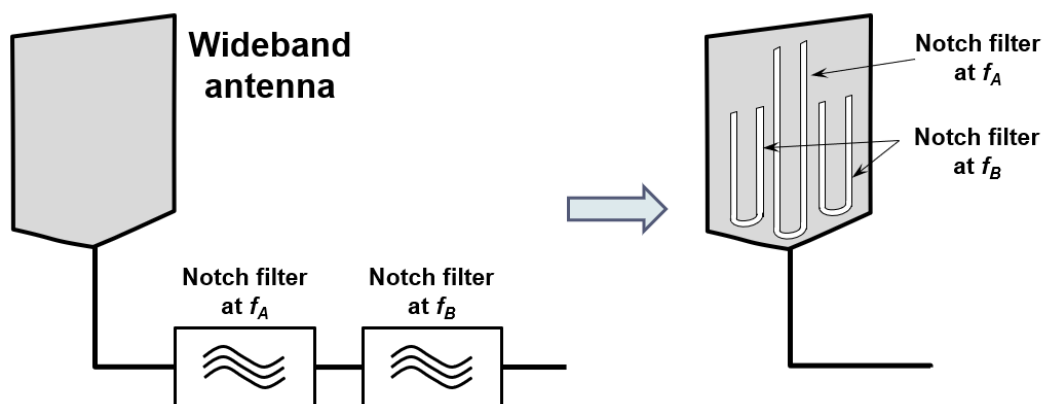
Fig. 3.1 The concept of multiple band-notched antenna system [8]

- Composed structure method (multiple narrowband integrations) [9]: It needs the single-band antennas that respond to target narrow frequency bands such as dipole and monopole antenna; then, integrating single band antennas can develop multiple narrowband antennas, which respond to every single antenna's detection frequency band. Fig. 3.2 shows the concept of the multiple narrowband integration method's structures. When using this method, the detection frequency numbers are defined by a single antennas number. The advantages of this method are simple adjustment and compact size because the detection and elimination frequencies can be changed independently from each other.
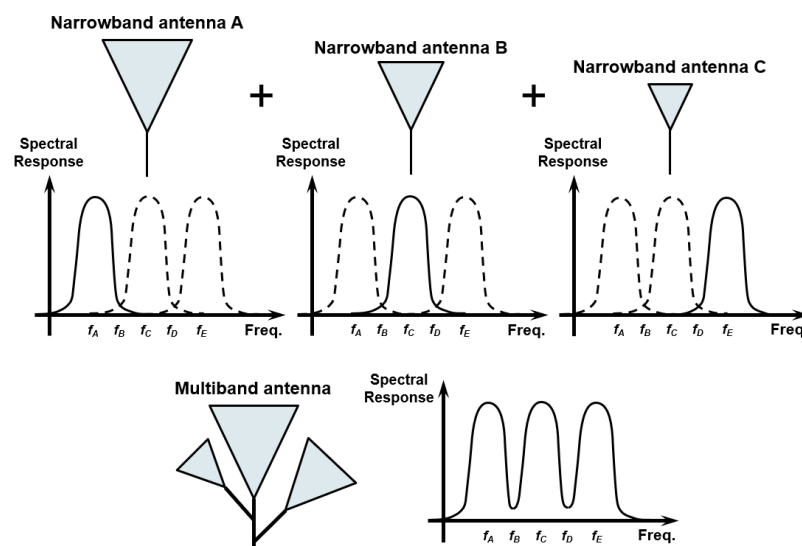
Fig. 3.2 The concept of the multiple narrowband integration antenna [9]

The PD emitted signal is changed based on many factors such as insulation and defect types, and the noise frequencies are also varied depending on the environmental conditions. The simple adjustment of detection and elimination frequencies is a high advantage for the UHF sensors. Therefore, the multiple narrowband integration method is used to develop the MNB antenna for PD detection because of the simple and compact structure.

3.2.3 Antenna type selection for MNB antenna

Once the composed structure method is selected, the narrowband antenna is needed to develop the MNB antenna. The antenna type is important to develop the UHF sensor because the main characteristics of the UHF sensor depend on the antenna type. According to the requirements of the UHF sensor, an antenna has to be printed flat structure, omnidirectional radiation, and electric field detection characteristics.

In chapter 1, many types of UHF sensors are compared. Among them, the patch, loop, dipole, and monopole are commonly used narrowband antenna types. The loop antenna is a magnetic field detection characteristic, which impedes the antenna installation process in HV equipment [10]. Integrating multiple patch antenna is not suitable for size limitation because of the rectangular-shaped radiation part. Thus, there are two antenna types to satisfy all criteria; printed dipole [11] and printed strip monopole antenna [12]. In this study, the printed quarter wavelength, strip monopole type is used for the multiple narrowband integration method as shown in Fig 3.3 because integrated strip monopoles can work with one ground plate, reducing the mutual inductions between radiation parts of the antenna. In addition, changing only one strip can adjust the corresponding resonant frequency of the antenna.

a) Two dimensions   b) Three dimensions
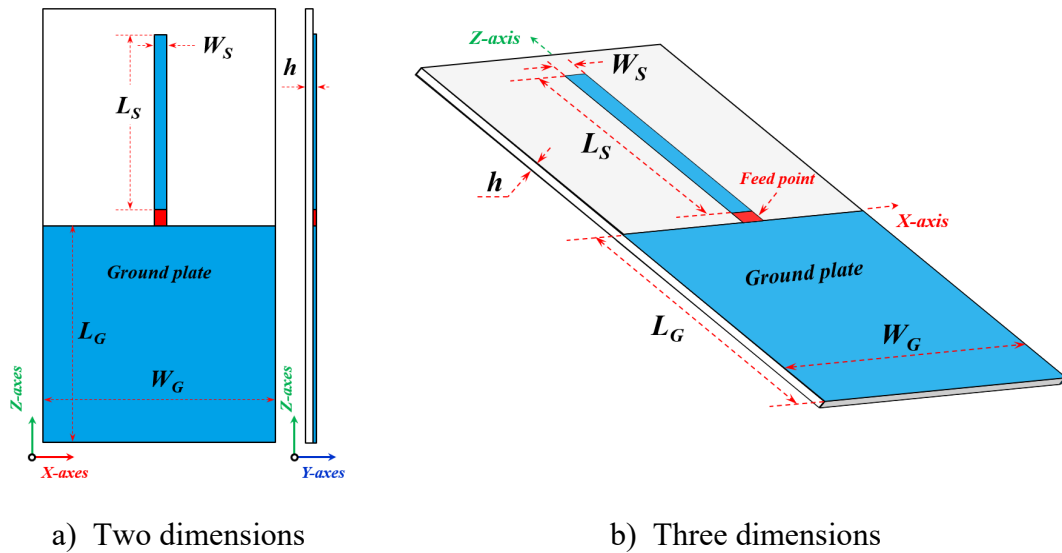
Fig. 3.3 Printed single strip antenna design

3.2.4. Frequency band selection of MNB antenna

The aim of the MNB antenna is a high sensitivity for PD detection and the noise resistance of specific noises such as communication, broadcast, and Wi-Fi frequencies. PD signal frequency depends on insulation media, discharge types, discharge condition, and so on, while they have band distribution in the UHF band. Therefore, it needs to define the operation frequency zone of the MNB antenna as an initial limitation. The operation frequency zone was selected as $0.5 \sim 2.5$ GHz for the MNB antenna proposed in this study to consider PD in SF_6 gas.

Since the operation frequency zone was selected, the elimination frequency (f_e) bands were defined by considering the environment noisy frequencies, and the number of f_e

could be chosen selectively. However, the high number of f_e reduces the PD detection sensitivity due to decreased detection frequency zone. Of course, the noisy frequency band is changed based on the measurement location, cell phone operation frequency band, cell phone transmission substation, etc. The four noise frequencies related to the communication and ISM frequencies in the UHF band were selected as f_e; (i) for cell phone frequency band, 850 MHz, (ii) for amateur radio band, 1250 MHz, (iii) for cell phone frequency band, 1700 MHz, and (iv) for a Wi-Fi frequency band of ISM frequency, 2.4 GHz [5].

After selecting the f_e, it needs two requirements to select the detection frequency (f_d) bands; (i) cover the frequency band of PD-emitted signal as much possible as wider range and (ii) avoid from the noise frequencies. In addition, the strip monopole antenna is resonated not only at its detection frequency but also at a higher-order resonance of that. Fig. 3.4 shows the explanation of the high-order resonation of strip monopole antenna.
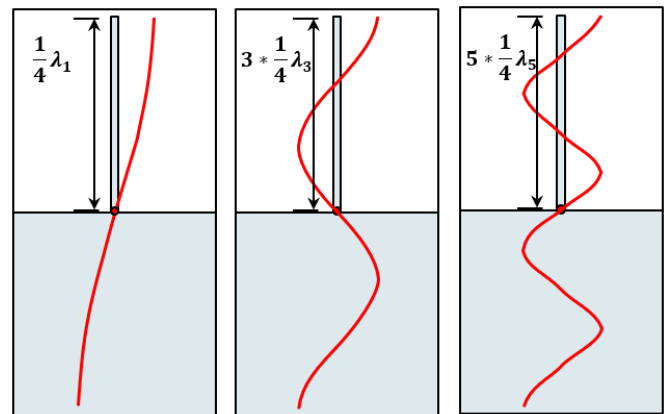
(a) EM wave detection
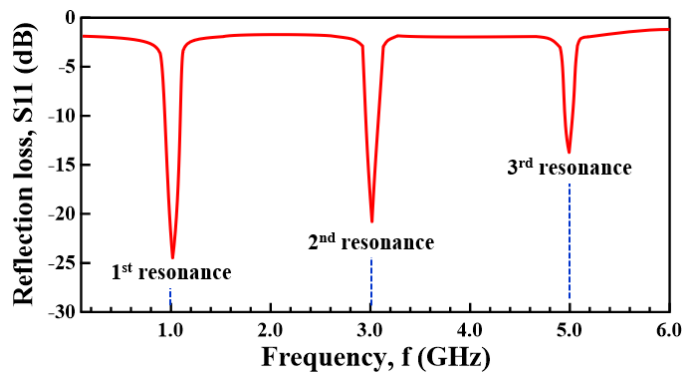
(b) Frequency response

Fig. 3.4 Higher-order odd number oscillation of the strip monopole antenna

The strip monopole antenna is resonated at target frequency (strip length equals quarter wavelength in this study). Also, it is resonated at the higher-order odd number

oscillation, for example, third and fifth-order in Fig. 3.4 (a). Therefore, it needs to consider the high order resonant frequency band to select the f_d bands. The four f_d were selected in this study as 0.6, 1.0, 1.4, and 1.8 GHz. The detection frequency band and high-order resonant frequencies should not cross the selected elimination frequency bands, as shown in Fig. 3.5. The simply adjustable feature of the MNB antenna is suitable for designing with different detection and elimination frequency characteristics selectively.
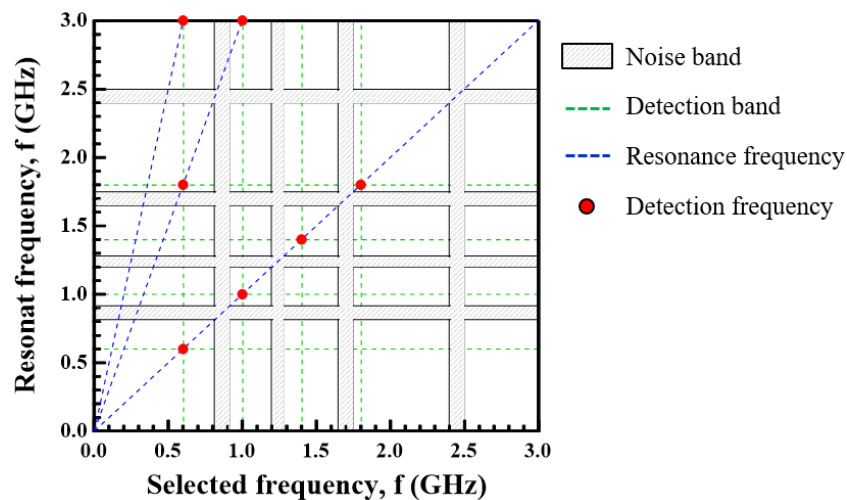
Fig. 3.5 Frequency band selection for MNB antenna

3.3   Design and simulation of MNB antenna

3.3.1   Single strip monopole antenna

As earlier mentioned, the printed strip monopole antenna was selected for developing an MNB antenna because this type's antenna is adequate for all requirements such as EF detection, simply adjustable, omnidirectional, compact, low cost, and so on. Therefore, the printed single strip, i.e., monopole type, antenna was investigated using a simulation made by COMSOL software [13] before designing the MNB antenna. In the simulation, main parameters were calculated, such as the reflection loss, i.e., the S11 parameter, as reflecting the detection properties together with the electric field (EF) distribution around the strip as well as the radiation pattern from the antenna.

Based on the repeated simulation results, the antenna physical dimensions were optimized, and whose effect for antenna performance was estimated and explained theoretically. Fig. 3.3 shows a typical configuration of the single strip antenna patterned on the printed circuit board (PCB), whose back surface has no metal plate and one feed point formed between the strip and the ground plate. There are three feeding methods for

printed monopole antennas; coaxial, coplanar waveguide, and microstrip. The coaxial feed method is used for MNB antenna because one-side printing and connection of SMA port are suitable for simply installing HV equipment. The other feeding methods are discussed deeply in Chapter 6 for enhanced MNB antenna.

There are a few main physical parameters for a single strip monopole antenna to optimize; strip length, strip width, ground length, ground width, feeding gap. The substrate's thickness and relative permittivity were set as $t = 1.6$ mm and $\varepsilon_r = 4.5$ as commercial FR-4 types PCB.

Strip length (L_S) **-** The strip length L_S corresponds to the resonant frequency, *i.e.*, f_d, based on a quarter wavelength ($\lambda/4$) arising on the strip, and the approximate formula on the strip length L_S at the f_d is given as equation (3.1).

$$L_S = \lambda/4 = \frac{c}{4f_d\sqrt{\varepsilon_{eff}}} \tag{3.1}$$

where c is the speed of light of 3×10^8 m/s, λ is a full wavelength, and ε_{eff} is the effective relative permittivity of the substrate.

Using equation (3.1), the strip length was calculated. Then, a single strip antenna was simulated with the calculated strip length when W_S, W_L, W_g, and f were fixed as 1mm, 100mm, 100mm, and 3mm, respectively. Fig. 3.6 shows the relation between calculated and simulated resonant frequencies based on the reflection loss parameter. Simulated resonant frequencies, f_s, generally agree with the calculated resonant frequencies, f_t. However, there was a slight difference between the estimated length from equation (3.1) and the simulated result of the COMSOL. Namely, some modification is needed to improve the accuracy of the equation (3.1).
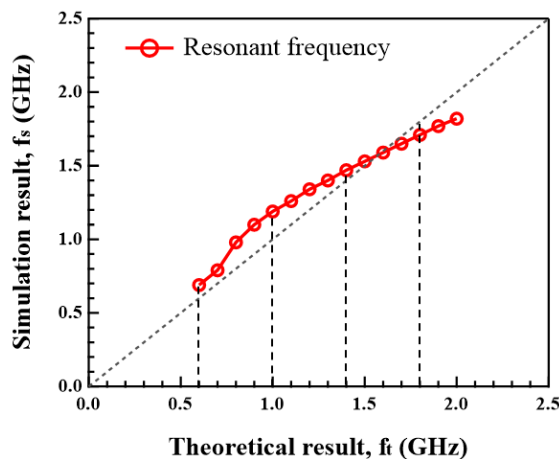
Fig. 3.6 The comparison between simulated and theoretical calculated frequencies

Strip width (W_S) **-** The strip width was determined based on the simulation result. In Fig. 3.7, the reflection loss curve of the single strip monopole antenna is shown depending on the strip width when L_S was fixed as 90.5 mm for 0.6 GHz frequency band. As a result of the increment of W_S, the frequency bandwidth is increased.
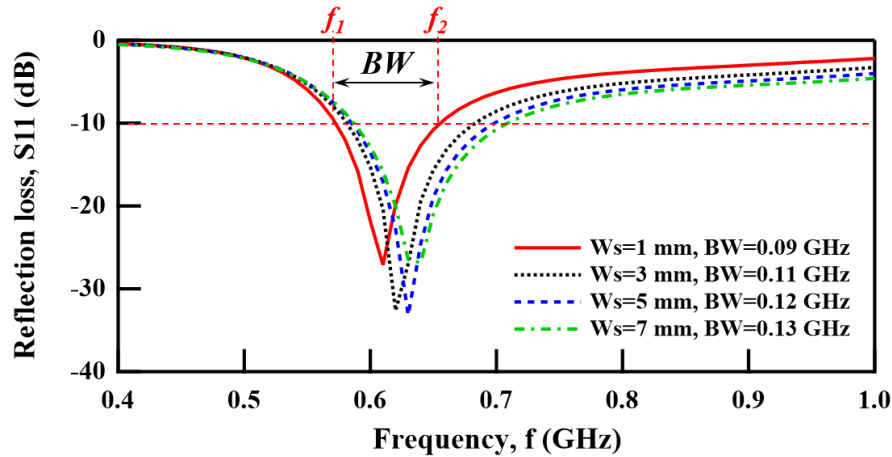
Fig. 3.7 Effect of strip width for reflection loss

The equivalent circuit of the antenna helps to understand the effects of the physical dimensions. Fig. 3.8 shows the five-element equivalent circuit used for printed strip monopole antenna [14, 15]. The equivalent circuit includes two parts; the parallel component represents the radiation part and resistance of the antenna, while the series circuit acts as the feed part and compensates for the reactance of the antenna. The value of lumped elements is changed based on the physical dimension of the antenna [14].
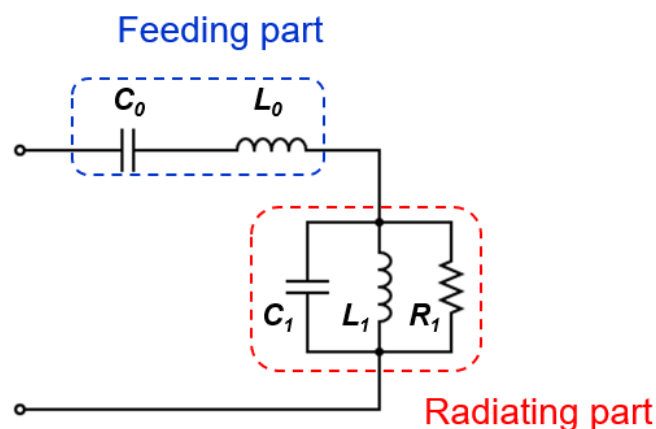
Fig. 3.8 Five-element equivalent circuit of the antenna [17]

The input impedance of single strip monopole antenna is shown in Fig. 3.9 when L_S =90.5mm, W_S =1mm, L_S =100, and W_S =100 mm. At the resonant frequencies, the Zin

was equal to 50 Ω. The second resonant frequency comes from the high order oscillation of the first resonant frequency.
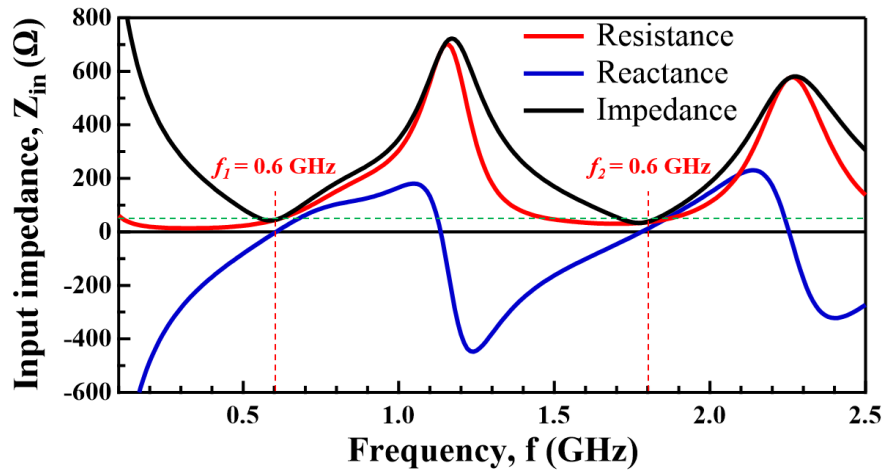
Fig. 3.9 Input impedance (L_S =90.5mm, W_S =1mm and $L_G = W_G$ =100 mm)

The capacitance and inductance of the antenna have a direct and reverse relationship with the strip width, respectively. It means that when strip width increased, the inductance reduced, and capacitance increased. These affect the antenna's quality factor (Q-factor). The Q-factor is defined as a dimensionless parameter that describes the underdamped condition of an oscillator or resonator and is calculated by equation (3.2) [16].

$$Q = \frac{1}{R}\sqrt{\frac{L}{C}}; \quad BW = \frac{f_r}{Q}; \quad (3.2)$$

From equation 3.2, it is clearly seen that the reduction of inductance and increment of capacitance made the Q-factor is reduced; consequently, the antenna bandwidth is increased.

In this study, MNB antenna is designed to realize narrow bandwidths because it increases the eliminate ability for untargeted frequencies, and multiple strips afford enough bandwidth for PD detection. Thus, the strip width was 1 mm, and further narrow strips than 1mm are difficult to fabricate.

Ground length and ground width (L_g and W_g) - The ground parts are used to take into the image theory. The ground size selected be longer than the radiation part to represent infinity ground as the following equation:

$$L_g > 6h + L_S; \quad (3.3)$$

where, h is substrate thickness, L_S is strip length. Fig 3.10 showed the simulation result when L_G was changed from 50 mm to 150 mm with a 25 mm step. The growth of L_G increases the equivalent circuit's parallel inductance ($L1$). As a result, the resonant frequency is reduced, and the bandwidth is increased. The lowest reflection loss occurred when L_S was 100 mm, the same as image theory.

Fig. 3.11 showed the simulation result when W_G was changed from 50mm to 150mm with 25 mm step. It seems that the W_G does not noticeably affect the antenna performance. Therefore, the ground length and width were fixed as 100 x100 mm, longer than the longest strip length (90.5 mm for f_{d1}=0.6 GHz).
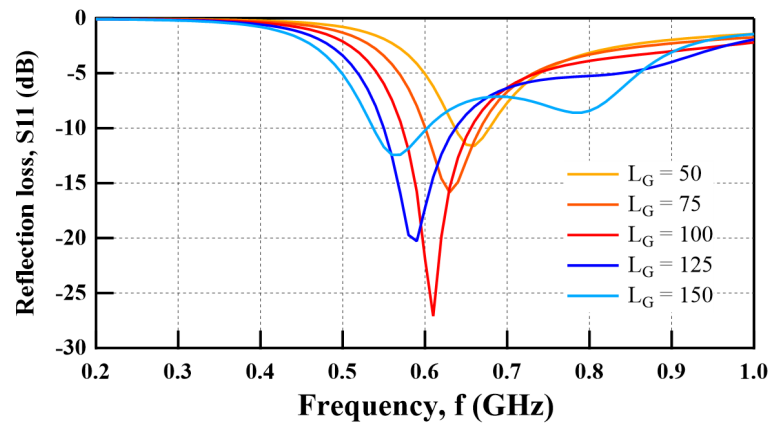
Fig. 3.10   Effect of ground length (W_G=100 mm, L_S=90.5mm, and W_S=1mm)
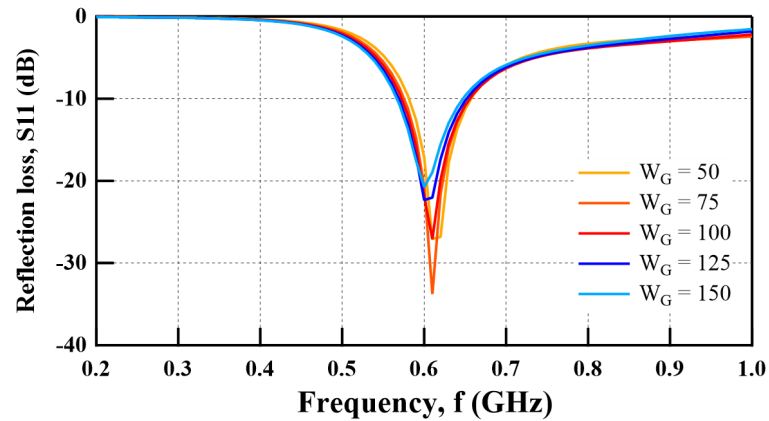
Fig. 3.11   Effect of ground width (L_G=100 mm, L_S=90.5mm, and W_S=1mm)

Feed length (*f*) - The feed length is a gap between radiation and ground parts of the antenna. According to the equivalent circuit, the $C0$ is reduced, and bandwidth is reduced if the feed length increases, as shown in Fig. 3.12. However, connecting the radiation and ground parts to the SMA connector is difficult. Therefore, the feed gap was selected as 3 mm to simplify the connection of the SMA port.
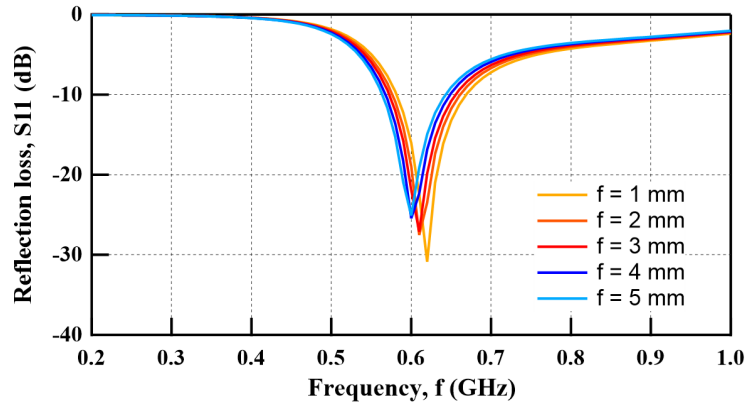
Fig. 3.12 Effect of feed length ($W_G = L_G$=100 mm, L_S=90.5mm, and W_S=1mm)

Simulation for target frequencies - Consequently, the single strip antennas are simulated for four detection frequencies (0.6, 1.0, 1.4, and 1.8 GHz). Table 3.1 shows strip length and the simulated resonant frequencies.

Table 3.1 Simulation result of the single narrowband antenna

Band	f_{d1}	f_{d2}	f_{d3}	f_{d4}
Target frequency (GHz)	0.6	1.0	1.4	1.8
Strip length (cm)	90.5	56.5	34.8	22.6
Resonant frequency (GHz)	0.61	0.98	1.4	1.82

Fig. 3.13 shows the reflection loss properties of single strip monopole antennas when the strip length is the same as shown in Table 3.1, and the W_S is fixed as 1 mm. The simulation result demonstrated that the detection frequencies decreased with an increase in the strip length, as expressed in equation (3.1). The reflection loss was lower than -6 dB at each resonant frequency, and resonant frequencies agree well with the target frequencies.

(a) Design
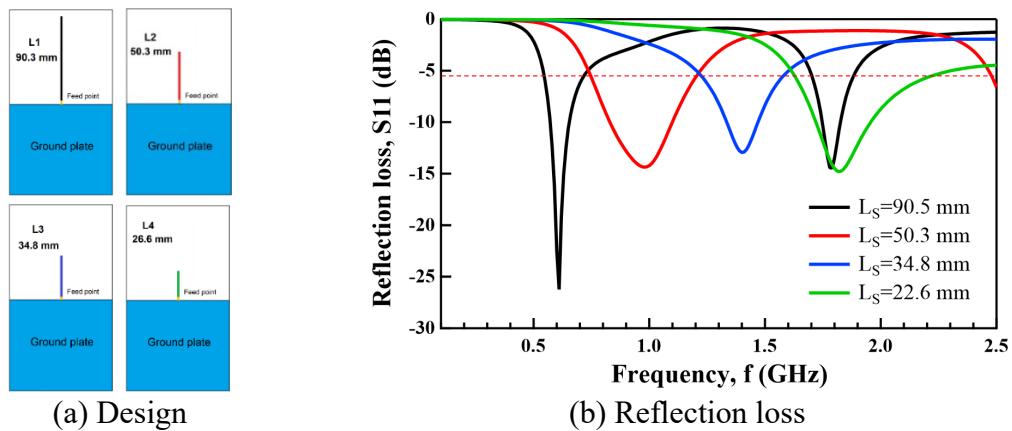
(b) Reflection loss

Fig. 3.13 Simulated reflection loss properties of the single strip antenna with different strip lengths.

In particular, two peaks were found in the longest strip of $L_S = 90.3$ mm; that is, 0.6 GHz and around 1.8 GHz. The former resonance corresponds to the designed frequency, while the latter is caused by the third-order resonance of the designed one. To confirm this, the electric field distributions of the single strip antenna ($L_S = 90.5$ mm) at 0.6 and 1.8 GHz were simulated (Fig. 3.14). At 0.6 GHz, the electric field accumulated around the strip edge to receive high power. While, the high intensity appeared in two points at 1.8 GHz; edge and one-third of the strip. It verified that the second resonant frequency is the third-order resonance of the first one.
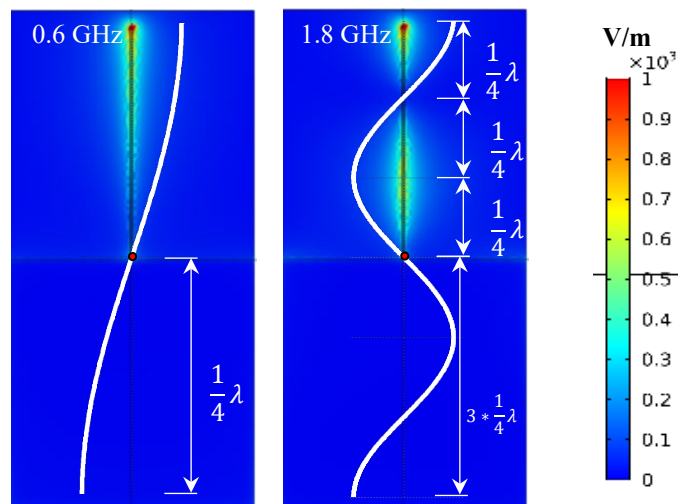
Fig. 3.14 Electric field distributions of the strip of Ls = 90.3 mm at different frequencies corresponding to the two peaks of the S11 properties in Fig. 3.13

3.3.2 Multiple Narrow Band antenna

The simulation result of the single narrowband antenna demonstrates applicable performance. Thus, the four strips antenna, i.e., MNB antenna, patterned on the PCB, and one feed point formed between the line bar connected with the four strips and the ground plate were configured as shown in Fig. 3.15. Each strip length was designed the same as the strip length of a single strip monopole antenna for each detection frequency. The strip length was calculated from the horizontal connection line connected to the feed point. The gap length between the strips, g, was decided as 5 mm as a reasonable value. If reducing the g, the mutual inductance between strips is increased.

In addition, the larger reflection loss, approaching zero at elimination ability of the frequencies represents good performance, can be deteriorated by increasing g due to the decrease in the Q-factor of the resonance even though the increasing g can reduce the interference between the strips.

Fig. 3.16 shows the simulated reflection loss properties of the four strips MNB antenna shown in Fig. 3.15 compared with the sum of the reflection loss values of each single strip monopole antenna in Fig. 3.13. In Fig. 3.16, the peak frequencies of the MNB antenna agreed well with the designed detection frequencies except for the second resonant frequency (1 GHz). This difference is related to the mutual inductance between strips. The second resonant frequency came from the second-longest strip, located between the first and third strip, and the mutual inductance between strips was highest in the second strip because that is directly related to the parallel strip lengths and reverse relation with the distance between strips. When the electric field accumulates the strip edge, the parallel strip works like parallel inductance, and the mutual inductance increases the self-inductance of the second strip. As a result, the resonant frequency of the second strip is increased.
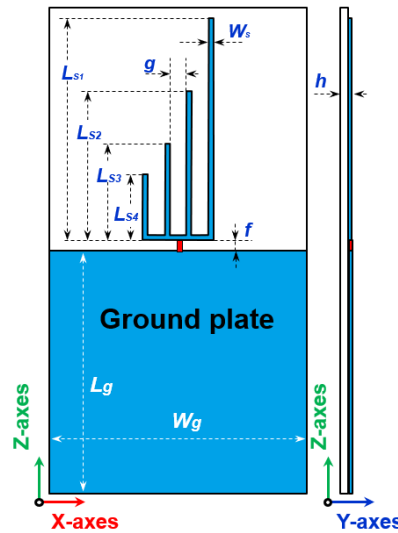
Fig. 3.15 Design of MNB antenna
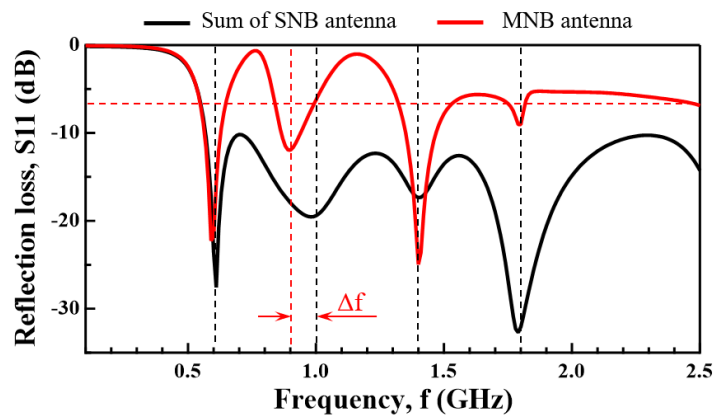
Fig. 3.16 Simulated S11 properties of the MNB antenna shown in Fig. 3.15 compared with the sum of the S11 values of each single strip antenna in Fig. 3.13

The second resonant frequency was adjusted from 1.1 GHz to 1.0 GHz by reducing the second strip length. Fig. 3.17 shows the reflection loss curve of MNB antenna after adjustment (Simulation-B) and compared with the previous result (Simulation-A). Table 3.2 shows the strip length and peak of resonant frequencies of simulations A and B. The simulation result demonstrated that it is possible to adjust the resonant frequency by changing the corresponding strip length without influencing other resonant frequencies.
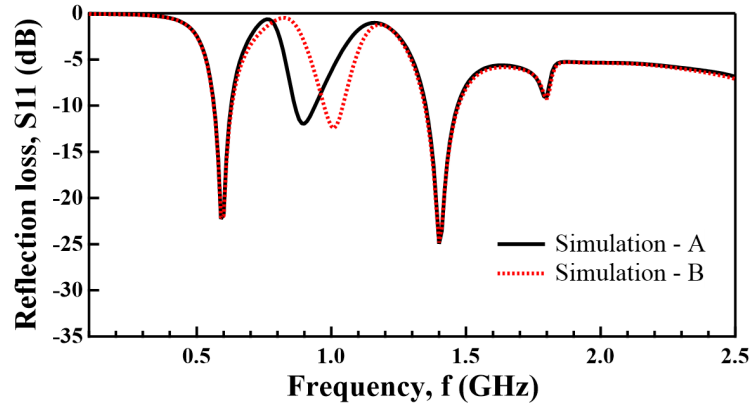
Fig. 3.17   Simulated S11 properties of the MNB antenna after adjustment and compared with the previous one

Table 3.2 Simulated resonant frequencies of MNB antenna

Band		1st	2nd	3rd	4th
Target frequency, f_T (GHz)		0.6	1.0	1.4	1.8
Simulation-A	L_S (cm) / f_d (GHz)	90.5 / 0.61	56.5 / 0.9	34.8 / 1.4	22.6 / 1.82
Simulation-B	L_S (cm) / f_d (GHz)	90.5 / 0.61	50.3 / 1.02	34.8 / 1.4	22.6 / 1.82

In addition, the detection frequencies were confirmed as the typical electric field distribution on the resonance appearing on the corresponding strip shown in Fig. 3.18. The existence of additional high order resonance of longest strip appeared at 1.8 GHz.
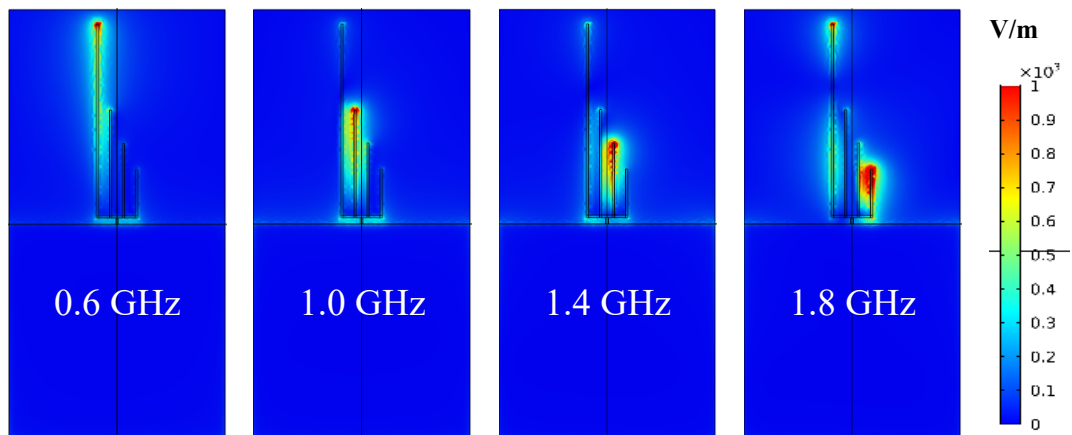
Fig. 3.18   Electric field distribution of the four strips MNB antenna at different detection frequencies.

As an example of the directivity of the MNB antenna, the simulated results of the radiation patterns in the 2D and 3D displays are shown in Fig. 3.19. In the figures, the direction of the strip length corresponds to the Z-axis, so the X and Y axes correspond to the perpendicular direction to the strips. The frequencies selected in the figures correspond to the detection ones. It seems that the MNB antenna has a good omnidirectional pattern in the X and Y-axis direction while weak in the Z-axis direction, which means that the directivity of the MNB antenna is fundamentally similar to a standard monopole antenna [12]. In addition, the omnidirectional radiation pattern can be adjusted flexibly using the cavity structure to increase the directivity at the target direction.
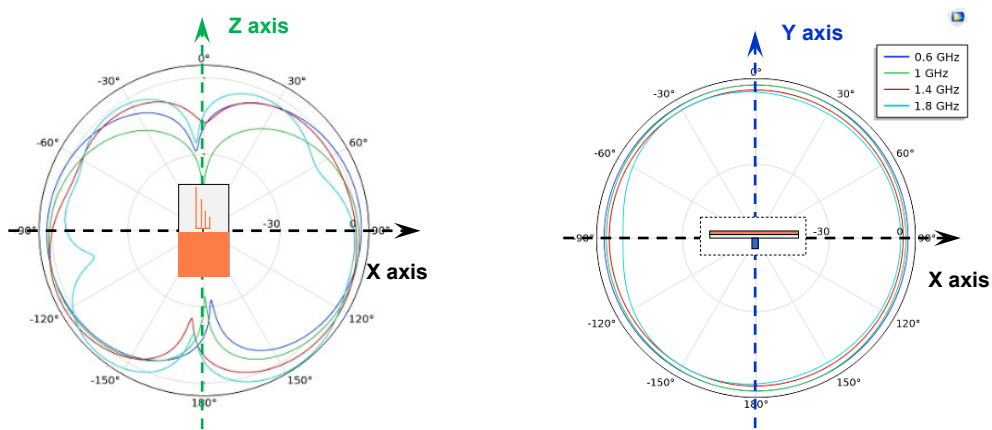
a) X-Z axis at Y=0   b) X-Z axis at Z=0
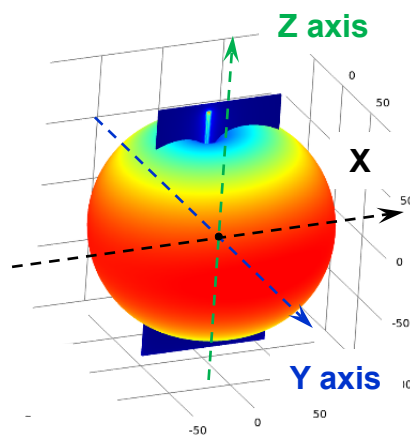
c) 3D simulation at f = 1 GHz

Fig. 3.19   Examples of a radiation pattern of the four strip MNB antenna at the detection frequencies as directivity.

3.4   Fabrication and test of MNB antenna

The four strips MNB antenna designed above was fabricated in a one-sided FR-4 PCB using a CNC machine as shown in Fig. 3.20 and connected an SMA connector at a feed point. Fig. 3.21 shows a photograph of the fabricated MNB antenna together with a Horn Antenna (HA), which is used in this study for comparison.
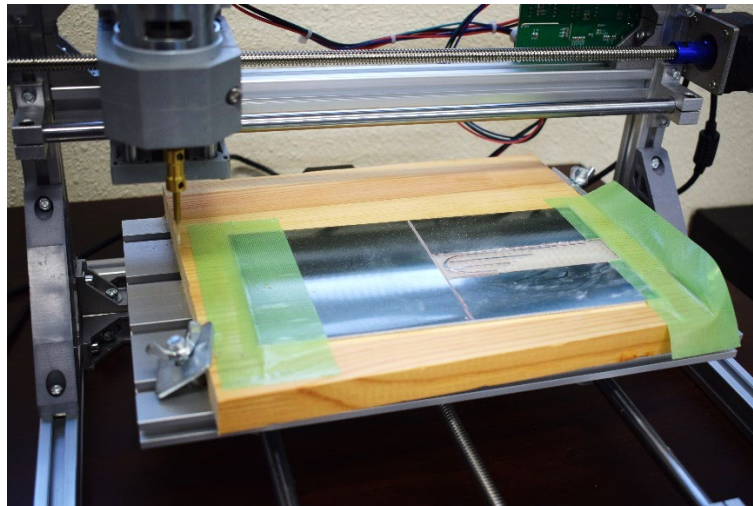
Fig. 3.20   MNB antenna fabrication process using CNC machine

Fig. 3.21   Comparison of size and shape between the fabricated four strips MNB antenna and a Horn antenna (HA)

Table 3.3 shows the physical dimension of the fabricated MNB antenna. The fabricated four strips MNB antenna is a flat printed type antenna, thus having a relatively thin and compact shape compared with the HA. This becomes an advantage when applying this antenna into the HV power equipment in view of freedom of arrangement and safety together with the nature of electric field detection. This section discusses the main antenna parameters based on experimental results such as reflection loss, transfer

function, and antenna factor. The directivity of the MNB antenna is experimentally examined in Chapter 4 by detecting the breakdown emitted signal.

Table 3.3 Physical dimension of fabricated MNB antenna

#	Parameters	Dimension (mm)
1	L_{S1}	90.5
2	L_{S2}	50.3
3	L_{S3}	34.8
4	L_{S4}	22.6
5	W_S	1.0
6	L_g	100.0
7	W_g	100.0
8	f	3.0
9	g	5.0
10	h	1.6

3.4.1 Reflection loss and transfer function measurement

After fabrication, the reflection loss of the MNB antenna was measured using a vector network analyzer, and the measurement setup is explained in Chapter 2. The measured reflection loss property is shown in Fig. 3.22 compared with the simulated result. The measured result basically agreed well with the simulated one even though the peak frequencies increased slightly from the simulated one, and a new remarkable dip around 2.0 GHz appeared. This difference in frequency might be caused by some parameter differences such as the relative permittivity and the thickness of the substrate that affect mutual inductance and coupling capacitance formed between the strips and/or between the strips and the ground plate, as well as the resultant Q-factor of the antenna.
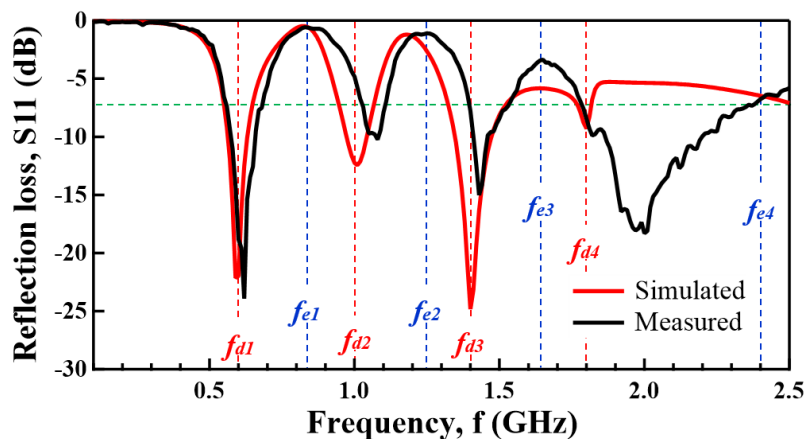
Fig. 3.22 Comparison of the reflection loss properties between the measured and simulated results for the four strips MNB antenna.

Also, the substrate thickness is changed due to the fabrication error. However, this difference affects as positive for antenna performance because the detection bandwidth was increased, and the important thing is that the reflection loss was lower than -6 dB at elimination frequencies.

As earlier mentioned, to belong to the detection frequency band, it is required that the reflection loss should be less than the threshold level (-6 dB). Based on the above definition, the detection bandwidth of the MNB antenna was calculated, and the result is shown in Table 3.4 for each detection frequency band. The total frequency bandwidth of the MNB antenna is 1.03 GHz. For antenna definition, if the absolute bandwidth exceeds 500 MHz or fractional bandwidth exceeds 10% of central frequency, that antenna is considered the wideband antenna [17]. Therefore, the MNB antenna is considered as a wideband antenna.

Table 3.4. The frequency bandwidth of MNB antenna

#	Resonant frequency (GHz)	Detection frequency zone (GHz)	BW of MNB antenna (GHz)
1	0.62	0.55 ~ 0.69	0.14
2	1.07	1.01 ~ 1.12	0.11
3	1.43	1.39 ~ 1.56	0.17
4	1.97	1.77 ~ 2.38	0.61
Total			**1.03**

Fig. 3.23 shows the measured transfer function of the MNB antenna when the reference antenna is HA. The transfer function was high at the f_d and reduced at the f_e. At the f_{d4}, the transfer function was slightly low. It could be related to the reference antenna or antenna gain because the transfer function is calculated based on two antennas' performance and gain.
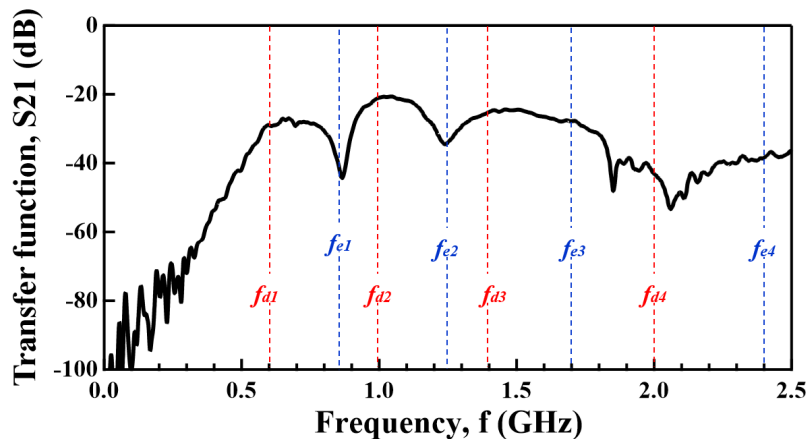
Fig. 3.23   Transfer function of MNB antenna compared with reflection loss

3.4.2 Antenna factor measurement

The UHF antenna receives the electric field emitted from discharge and transmits it to the voltage at the output of the antenna terminal. The antenna factor (AF) represents the transmission coefficient between the incident electric field and output voltage. As determining the AF, the original electric field emitted from discharge could be calculated. In practice, a logarithmic expression for the AF is much simpler to apply and is more commonly used. As discussed in Chapter 2, the three antennas method used to measure the antenna factor of MNB antenna. The two standard-HAs were used with MNB antenna as three transmit/receive pairs, and a vector network analyzer was used to measure the S21-parameter for each pair.

From the Friis formula, the relation between antenna gains and S21-parameter can be represented as the following equations:

$$G_a + G_b = (S_{21})_{ab} + 20 \log\left(\frac{4\pi R}{\lambda}\right); \tag{3.4}$$

$$G_b + G_c = (S_{21})_{bc} + 20 \log\left(\frac{4\pi R}{\lambda}\right); \tag{3.5}$$

$$G_c + G_a = (S_{21})_{ca} + 20 \log\left(\frac{4\pi R}{\lambda}\right); \tag{3.6}$$

where G is the gain of the corresponding antenna and $20 \log\left(\frac{4\pi R}{\lambda}\right)$ is free space propagation loss, R is the distance between two antennas, λ is the wavelength.

By simplifying the above system equations, the antenna gain of each antenna can be obtained as below equations.

$$G_a = \frac{1}{2}\left\{(S_{21})_{ab} + (S_{21})_{ca} - (S_{21})_{bc} + 20 \log\left(\frac{4\pi R}{\lambda}\right)\right\}; \tag{3.7}$$

$$G_b = \frac{1}{2}\left\{(S_{21})_{ab} + (S_{21})_{bc} - (S_{21})_{ca} + 20 \log\left(\frac{4\pi R}{\lambda}\right)\right\}; \tag{3.8}$$

$$G_c = \frac{1}{2}\left\{(S_{21})_{bc} + (S_{21})_{ca} - (S_{21})_{ab} + 20 \log\left(\frac{4\pi R}{\lambda}\right)\right\}; \tag{3.9}$$

Consequently, the AF is calculated using the following equation.

$$AF(dB) = 20 \log \left[\frac{2\pi}{\lambda} \sqrt{\frac{2.4}{10^{G/10}}} \right] \qquad (3.10)$$

Fig. 3.24 (a) shows the AF measurement result of HA compared with the AF from the datasheet, which is the general specific document of BBHA 9120 A types HA. The main trends of the measured AF and datasheet values agreed well except for the small gap, around 1.5 dB, same as Chapter 2. From 2.1 GHz, the measured AF was slightly increased because of the reflection of the ground. Fig. 3.24 (b) shows that the measured AF of the MNB antenna, which has high relation with a transfer function. The electric field emitted from the discharge signal could be calculated using AF.

(a) The HA (b) The MNB antenna
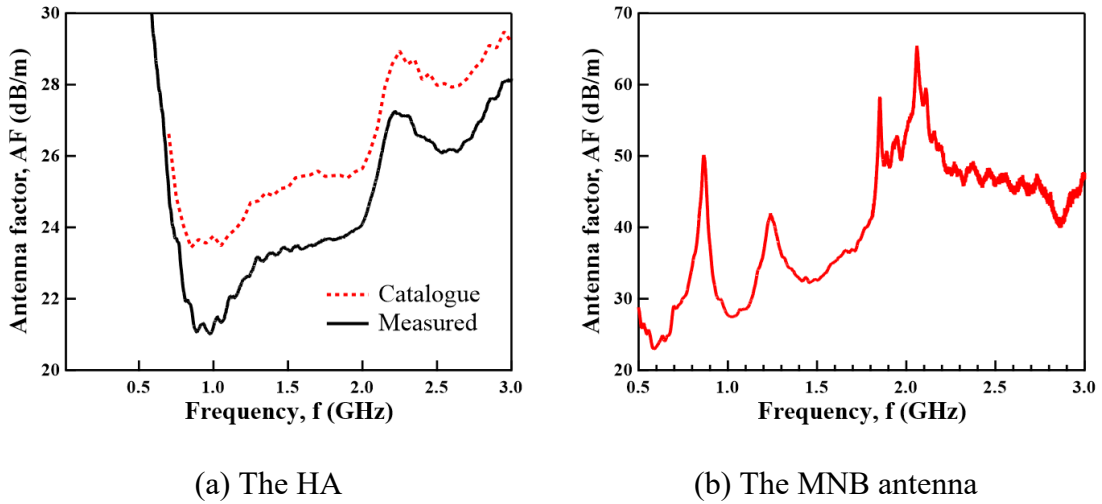
Fig. 3.24 The measurement result of AF compared with the datasheet of the factor

3.4.3 MNB antennas with a different structure for comparison

The proposed MNB antenna has been evaluated theoretically and experimentally, and the result shows the desirable antenna performance. However, the proposed MNB antenna is a general study. There is the same way to improve the antenna structure. For example, the L-shape or a meandering radiation part can reduce the antenna size [18], discussed in the Appendix. Also, the MNB antenna can be developed with a microstrip circuit without size extension as a changing feed method. This topic is introduced in Chapter 6 [19].

This section discusses the MNB antennas with different connection structures for comparison purposes with the proposed MNB antenna, as shown in Fig. 3.25. The MNB-B and MNB-C are designed and fabricated for the same detection and elimination

frequency band with the proposed antenna, MNB-A. The MNB-B and MNB-C antenna was designed with U-shaped and a short straight connection line. Also, the MNB-C antenna was designed with a short ground plate. The measured reflection loss of MNB antennas is shown in Fig. 3.26.
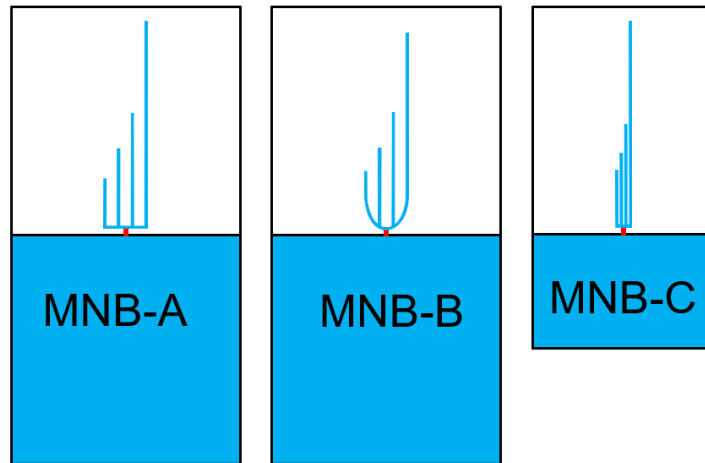
Fig. 3.25   The MNB antennas with different connection structure

The total detection bandwidth of MNB antenna is 1.03 GHz, 1.15 GHz, and 0.81 GHz for MNB-A, MNB-B, and MNB-C antenna, respectively. The MNB-B antennas detection BW is slightly higher than the MNB-A antenna, but the resonant frequency of MNB-B and MNB-C antennas are shifted from target frequencies due to the change of radiation part size and mutual inductance between strips. The fabricated MNB antennas' performances are compared based on the discharge measurement experimental result in Chapter 4.
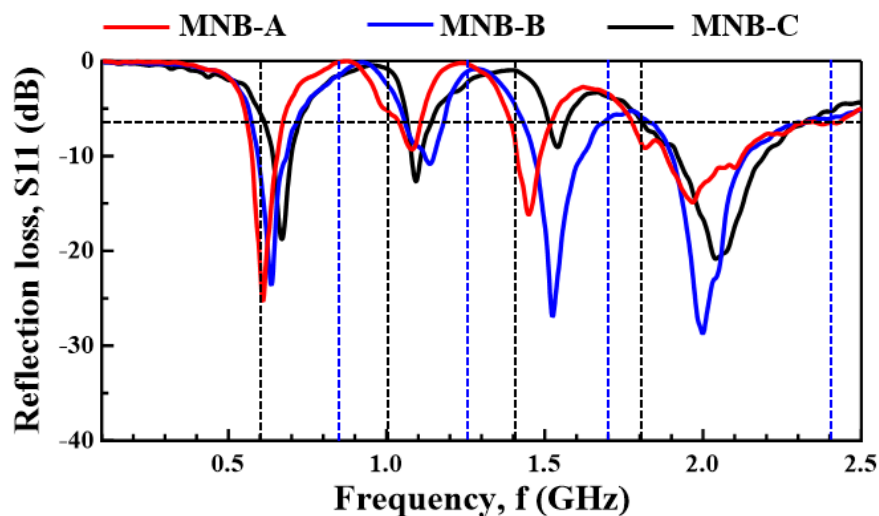
Fig. 3.26   Reflection loss of MNB antennas shown in Fig. 3.25

3.5   Conclusion

The multiple narrowband antenna was designed as a novel wideband UHF sensor for PD detection with high noise resistance in this chapter. The antenna performance was clarified based on simulation and experimental results. The conclusions are shown below.

1.   The multiple narrow band (MNB) antenna has been successfully designed for the UHF method with noise reduction ability.

2.   Using the integration method, the MNB antenna kept the resonant frequency of all single strips, and it means each detection frequency can be adjusted independently from others.

3.   The MNB antenna satisfies the main requirements of the UHF sensor, such as multiple narrow bands for high sensitivity, elimination frequency bands for noise, omnidirectional radiation pattern, compact, simply adjustable, and low-cost structure.

4.   The based on the theoretical and experimental results, the MNB antenna designing flow chart was made, as shown in Fig. 3.27. Following this flow chart, it is possible to selectively design the MNB antenna for different types of PD and different noise conditions.

5.   This study is fundamental research, so we did not focus on size reduction of the antenna and used a straight strip for the MNB antenna. However, if there are some size limitations, it is possible to reduce the antenna size using the L-shape or meandered strip.

Start

Substrate thickness (h) and dielectric constant (ε_r)

Detection frequency zone ($f_{d\ min}$ & $f_{d\ max}$)

Elimination frequencies (f_{en})

Select detection frequencies (f_{dn})

Yes

$f_{dn} = f_{en}$

No

Calculate the strip length ($L_{sn} = \frac{1}{4} * \lambda_{eff\_n}$)

Yes

Size limitation? (Select radiation shape)

No

Straight strip line

Calculate the strip width (W_S based on BW)

Calculate the ground size (L_g & $W_g \geq L_{S\ max} + (6 \times h)$)

No

Within size limitation?

Yes

L-shape radiation or Meandered line radiation

Feed method selection (Based on purpose)

$f_{Rn} = f_{dn}$ && $f_{Rn} \neq f_{en}$

No

Adjustment L_S and W_S

Yes

End

Fig. 3.27   MNB antenna designing flow chart

References

[1]   H. F. Ye, Q. Yong, D. Yue, G. H. Sheng, and X. C. Jiang, "Development of multi-band ultra-high-frequency sensor for partial discharge monitoring based on the meandering technique," *IET Sci. Meas. Technol.*, Vol. 8, No. 5, pp. 327–335, 2014.

[2]   E. M. Amin and N. C. Karmakar, "A passive RF sensor for detecting simultaneous partial discharge signals using time-frequency analysis," *IEEE Sens. J.*, Vol. 16, No. 8, pp. 2339–2348, 2016.

[3]   B. F. Hampton and R. J. Meats, "Diagnostic Measurements At Uhf in Gas Insulated Substations.," *IEE Proc. C Gener. Transm. Distrib.*, Vol. 135, No. 2, pp. 137–144, 1988.

[4]   British Standards Institution, "High Voltage Test Techniques—Measurement of Partial Discharges by Electromagnetic and Acoustic Methods," 2016.

[5]   T. Bandi, M. Tanaka, H. Furuie, and S. Ohtsuka, "Developing of Multiple-narrowband Antenna to Detect Partial Discharge-emitted Signal under Radio Communication Noise Environment," *Proceeding - 8th Int. Conf. Cond. Monit. Diagnosis, C. 2020*, pp. 154–157, 2020.

[6]   S. Coenen and S. Tenbohlen, "Location of PD sources in power transformers by UHF and acoustic measurements," *IEEE Trans. Dielectr. Electr. Insul.*, Vol. 19, No. 6, pp. 1934–1940, 2012.

[7]   Y. X. Guo, M. Y. W. Chia, and Z. N. Chen, "Miniature built-in multi-band antennas for mobile handsets," *IEEE Trans. Antennas Propag.*, Vol. 52, No. 8, pp. 1936–1944, 2004.

[8]   W. S. Lee, W. G. Lim, and J. W. Yu, "Multiple band-notched planar monopole antenna for multi-band wireless systems," *IEEE Microw. Wirel. Components Lett.*, Vol. 15, No. 9, pp. 576–578, 2005.

[9]   H. G. Schantz, G. Wolenec, and E. M. Myszka, "Frequency notched UWB antennas," *2003 IEEE Conf. Ultra Wideband Syst. Technol. UWBST 2003 - Conf. Proc.*, pp. 214–218, 2003.

[10]   T. Hoshino, K. Nojima, and M. Hanai, "Real-time PD identification in diagnosis of GIS using symmetric and asymmetric UHF sensors," *IEEE Trans. Power Deliv.*, Vol. 19, No. 3, pp. 1072–1077, 2004.

[11]   T.-C. T. and K.-L. W. Yung-Tao Liu, "High-Gain Printed Dipole Antenna,"

Microw. Opt. Technol. Lett., Vol. 46, No. 3, pp. 214–218, 2005.

[12]   M. J. Ammann and M. John, "Optimum design of the printed strip monopole," *IEEE Antennas Propag. Mag.*, Vol. 47, No. 6, pp. 59–61, 2005.

[13]   COMSOL AB, "COMSOL Multiphysics® v. 5.6. www.comsol.com." Stockholm, Sweden.

[14]   Y. Liao, T. H. Hubing, and D. Su, "Equivalent Circuit for Dipole Antennas in a Lossy Medium," *IEEE Trans. Antennas Propag.*, Vol. 60, No. 8, pp. 3950–3953, 2012.

[15]   M. Hamid and R. Hamid, "Equivalent circuit of dipole antenna of arbitrary length," *IEEE Trans. Antennas Propag.*, Vol. 45, No. 11, pp. 1695–1696, 1997.

[16]   J. Bird, *Electrical Circuit Theory and Technology, 6th ed*. 2017.

[17]   "Ultra-Wideband Transmission Systems," *US Fed. Commun. Comm. (FCC), Part 15 - Radio Freq. device, 503 - Defin.*, 2002.

[18]   T. Leng, X. Huang, K. Chang, J. Chen, M. A. Abdalla, and Z. Hu, "Graphene Nanoflakes Printed Flexible Meandered-Line Dipole Antenna on Paper Substrate for Low-Cost RFID and Sensing Applications," *IEEE Antennas Wirel. Propag. Lett.*, Vol. 15, pp. 1565–1568.

[19]   T. Bandi and S. Ohtsuka, "Application of Microstrip Filter for Multiple Narrow Band Antenna to Detection of Partial Discharge," in *The 22nd International Symposium on High Voltage Engineering, 2021*, pp. 1–5.

Chapter 4

Discharge Detection Properties of MNB antenna

4.1 Introduction

Chapter 3 clarified a new Multiple Narrow Band (MNB) antenna design and evaluated the antenna's performance theoretically and experimentally. As integrating the printed strip monopole antennas, the MNB antenna was developed as the wideband UHF sensor with high noise resistance. The advantage of the MNB antenna can be fabricated for different types of PD and different noise conditions using the designing rule as shown in Fig. 3.27. The proposed MNB antenna consists of four strips with different lengths to detect four detection frequencies, f_d, and eliminate four elimination frequencies, f_e. The detection frequencies of the MNB antenna were selected as 0.6, 1.0, 1.4, and 1.8 GHz, which skipped the elimination frequencies (0.85, 1.25, 1.70, and 2.40 GHz) and corresponded to the PD emitted frequency zone at the UHF band. The simulation and test results showed that the MNB antenna satisfies all requirements of the UHF sensor. In addition, the two different MNB antennas (MNB-B and MNB-C) were fabricated with different connection structures for checking the versatility of MNB antenna and comparison purposes except for the proposed MNB antenna (MNB-A).

In this chapter, the fabricated MNB antennas are first compared based on breakdown discharge (BD) measurement; then, the proposed MNB antenna is further investigated compared with the standard wideband Horn Antenna (HA). The discharge detection ability of the MNB antenna is assessed on the breakdown and partial discharge (PD) experiments results. The frequency components of the PD emitted signal are changed based on the insulation materials and PD types [1]. The SF_6 gas is known as a highly used insulation gas for GIS because of extremely chemically stable, non-flammable, and highly electronegative, with excellent dielectric properties of approximately three times more than air. Therefore, the MNB antenna, discussed in this study, is designed for the PD in SF_6 gas, and detection frequencies are selected for PD in SF_6 gas. However, in the electric power substation, a complicated and combined substructure, many HV equipment work together simultaneously. For example, the GIS is connected to the electric system through a high voltage power cable (XPLE insulation) or overhead transmission line (air insulation).

Therefore, the MNB antenna is applied to detect the PD in SF_6 gas, dry air, and XPLE insulations and compared with HA, whose technical parameters are shown in Chapter 2. The purposes of HA were (i) the comparison of detection abilities of antennas and (ii) to understand the original characteristic of discharge signal because the HA has excellent wide and flat frequency response.

4.2   Breakdown discharge detection

Electrical breakdown is defined as the process by which an insulating material in a strong electric field becomes electrically conductive. The electric field needed for BD occurrence depends on many factors, including the distance between electrodes, environment condition (humidity, temperature, pressure), insulation material condition, and so on. BD phenomena cause the high electric current, large electric spark, steep temperature, and pressure rise, which are the reason for the catastrophic failure of electric equipment and can affect the stability and reliability of electric power systems. Also, EM waves are emitted from BD with a higher amplitude than PD phenomena. Therefore, the MNB antennas shown in Fig. 3.25 were applied to detect BD emitted signal for the first trial of discharge detection.

4.2.1 Comparison of fabricated MNB antennas

Fig. 4.1 shows a schematic diagram of the experimental setup to measure BD phenomena in the air as discharge signal measurement. BD phenomena were generated between a needle to plane electrode system in the air by applying the high voltage.
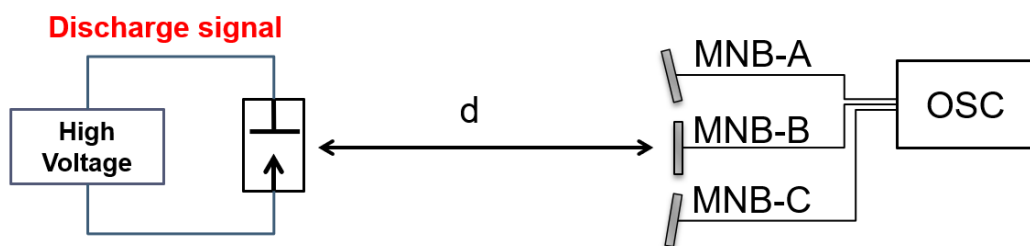
Fig. 4.1 Experiment setup to measure the breakdown signals in the air.

The MNB antennas simultaneously measured BD signal with the same measurement system. As an example of the simultaneous measurement, the typical discharge waveforms are shown in Fig. 4.2. The MNB-A and B antennas' peak-to-peak amplitudes (V_{PP}) were similar and much higher than MNB-C due to the detection frequency band of antennas. The detection frequency band of MNB antennas was discussed in Chapter 3.

Fig. 4.3 shows the scattering of V_{PP} based on 100 times measurement results. The average V_{PP} of antennas was 240, 242, and 122 mV for MNB-A, B, and C antennas. The MNB-C antennas detection ability was much lower than the other two antennas, and MNB-A and MNB-B antennas detection abilities have very high similarities because of the detection bandwidth of antennas.
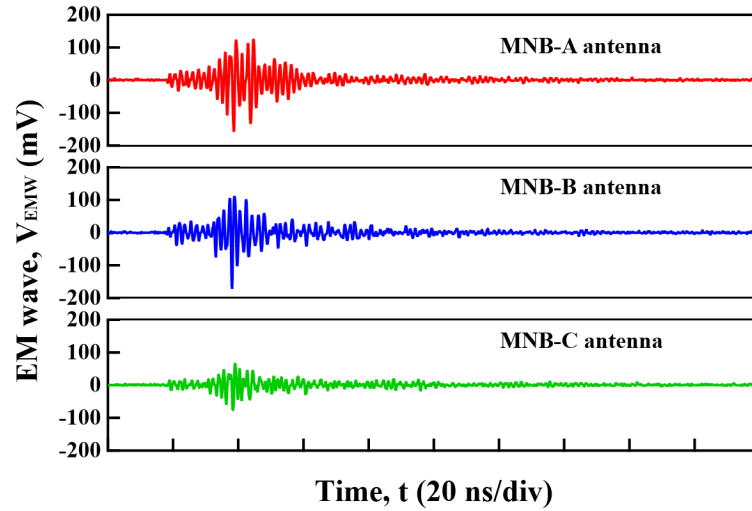
Fig. 4.2 BD emitted EM wave measured by MNB antennas
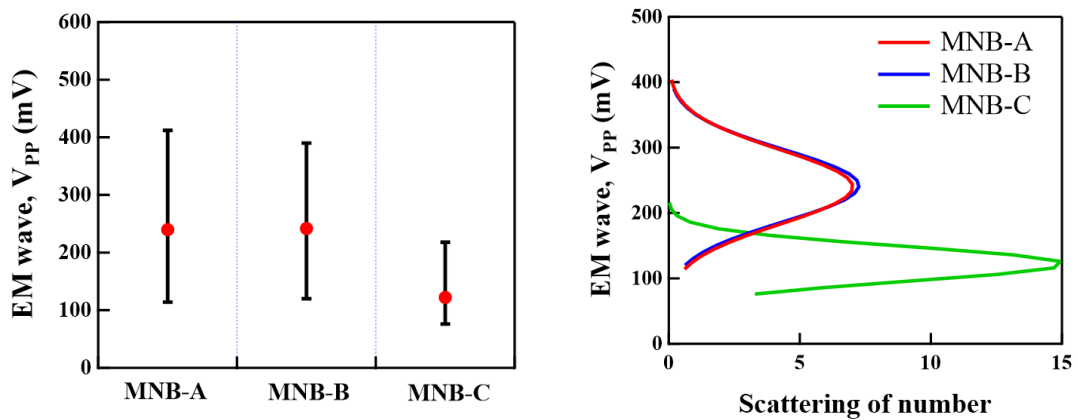
Fig. 4.3 V_{PP} of BD emitted EM waves based on segmented memory acquisition function

The measurement result confirmed that the MNB antenna could be developed with different connection lines depending on the purpose. In addition, the PD detection ability of the UHF sensor is directly related to the detection bandwidth. Consequently, the MNB-A was selected to investigate further because the detection ability was comparable and simple structure and fabrication with a rectangular connection line.

Once the MNB-A antenna was selected as a proposed antenna, it was compared with a standard wideband Horn Antenna (HA) to evaluate the discharge detection ability of the MNB antenna. The HA's performance was discussed in Chapter 2, and the purpose is

a comparison and to check the original characteristic of the discharge signal. The measured typical BD signal waveforms are shown in Fig. 4.4 using the experimental setup shown in Fig. 2.8. The V_{PP} of MNB antenna is negligibly lower than HA antenna because the bandwidth of HA is wider than MNB antenna. Fig. 4.4 (b) represents the expansion of the front part of the whole wave in Fig. 4.4 (a). It is clearly seen that the waveforms measured by the MNB antenna agreed very well with the HA in terms of amplitude and waveshape. The slight difference in the first part came from the frequency property of the antennas in the high-frequency range.

(a) Whole waveforms

(b) Expand waveforms at the front part of (a)
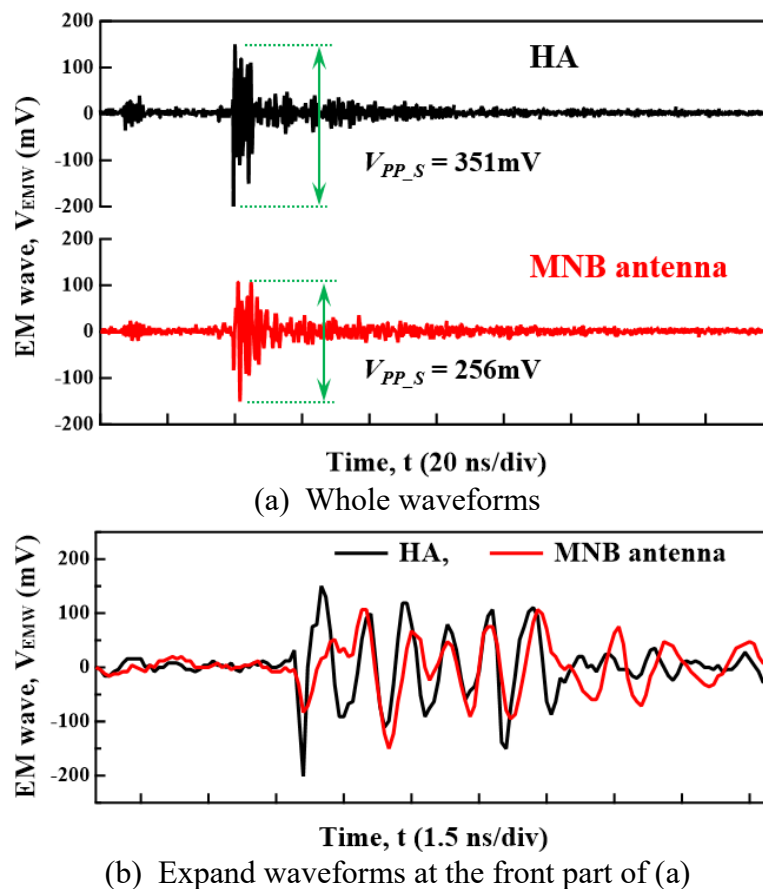
Fig. 4.4 Simultaneously measured waveforms of discharge signal by the MNB antenna and HA

Consequently, the relation between the V_{PP}'s of the waveforms measured by the MNB antenna and the HA was investigated [2]. As obviously seen in Fig. 4.5, the two antennas' V_{PP} indicates a high correlation with the correlation coefficient of 0.85, and the slope of the V_{PP} properties indicates 0.78. These results suggest that the MNB antenna realizes wideband by considering the multi-frequency bands, which enable a highly sensitive property similar to the wideband antenna against the breakdown signals.
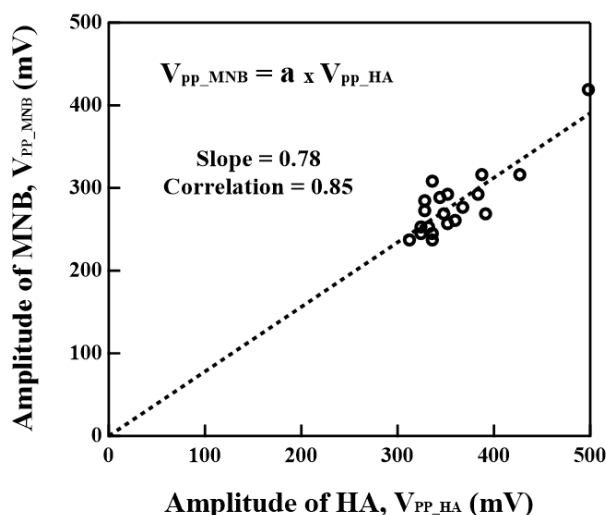
Fig. 4.5 Relation of the peak to peak amplitude of the measured breakdown discharge signals between the MNB antenna and the HA.

Fig. 4.6 shows the averaged frequency spectrum obtained from the Fast Fourier Transform (FFT) of the 20 breakdown waveforms measured by HA and MNB antennas. The dotted lines in the figures are the average value of total intensity for each antenna and represent a kind of reference line to simply discuss the detected and eliminated frequency ranges. Namely, the definition is that the frequencies with the spectral intensity above the dotted line are detected, and the frequency range below that is to be eliminated.

From the frequency spectrum of HA in Fig. 4.6 (a), it is clearly seen that the frequency component of BD was between 0.5 GHz and 1.7 GHz, and the peak of intensity occurred around 1.0 GHz. The MNB antenna had relatively undulating characteristics, i.e., peaks for detection and dips for elimination, compared to the HA due to multiple resonant bands. Note that the measured frequencies for the peaks and bottoms appeared basically around the designed ones of 0.6, 1.0, and 1.4 GHz for detection and 0.85, 1.25, and 1.7 GHz for elimination, while there was difficult to see the peak around the designed frequency of 1.8 GHz due to the relatively lower signal level.

Based on the definition of detected and eliminated frequency ranges, the total detection frequency bandwidth of the MNB antenna was evaluated as 72% of the HA in the UHF band. The ratio of the MNB antenna to the HA of the detection frequency range (0.72) was very close to the slope of the amplitude V_{PP} of both the antennas (0.78) shown in Fig. 4.5. This means that relation of the measured amplitude between the MNB antenna and the HA is valid and depends on the detection frequency properties of the antenna. As the detection bandwidth increases, the MNB antenna's detection ability can be increased.
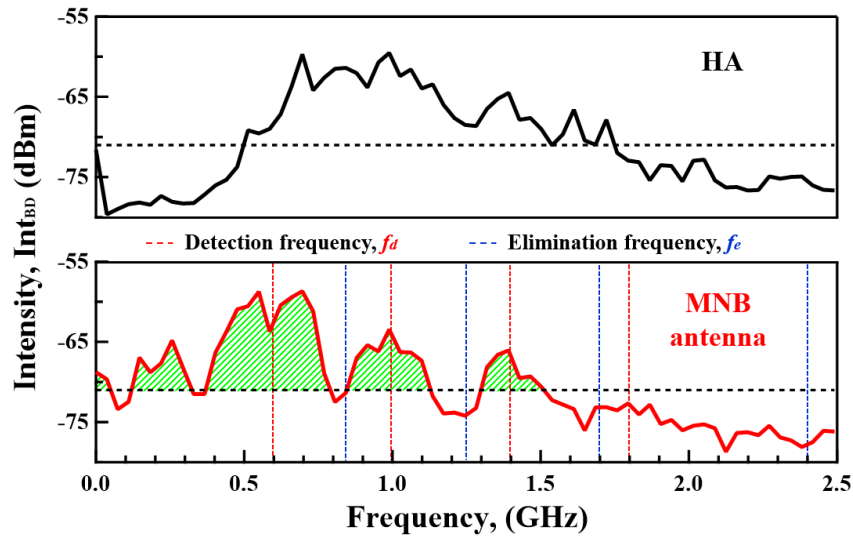
Fig. 4.6 Comparison between the averaged frequency spectrum of the BD signals measured by the MNB antenna and the HA.

4.2.2 Breakdown discharge measurement for antenna directivity

In Chapter 3, the radiation pattern of the MNB antenna was introduced based on the simulation result. In this section, the directivity of the MNB antenna was experimentally investigated by changing the antenna arrangement under the fixed discharge source. The HA was used as a reference antenna. The electromagnetic (EM) waves measured by both antennas are shown in Fig. 4.7 for each direction.

(a) Front side

(b) Back side

(c) Right side

(d) Left side
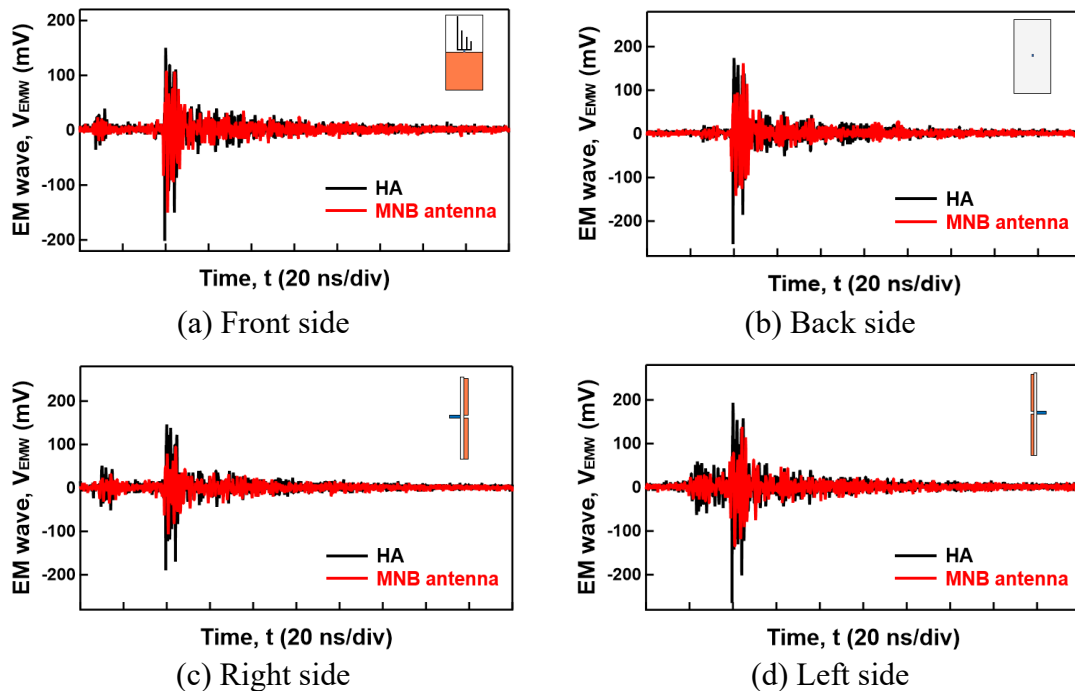
Fig. 4.7 EM wave measured by HA and MNB antenna when the position of MNB antenna was changed (continued on the following page)

(e) Top side   (f) Bottom side
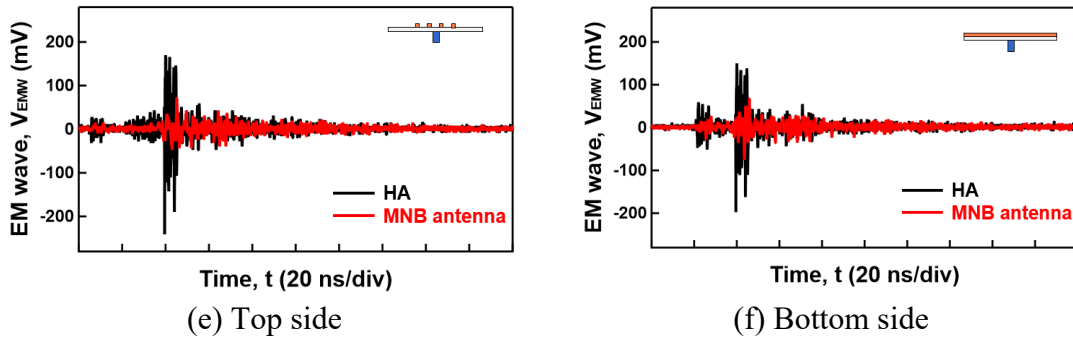
Fig. 4.7 EM wave measured by HA and MNB antenna when the position of MNB antenna was changed

The V_{PP} of measured EM waves is changed based on the direction of the MNB antenna due to the radiation pattern's differences. The summarized result is shown in Fig. 4.8, where R represents the ratio between the V_{PP} of both antennas. The ratio increased following order; top (0.23), bottom (0.28), right (0.64), left (0.65), back (0.74), and front (0.78) side of MNB antenna. Of course, the ratios can be changed based on the frequency band of the received signal because the antenna's directivity is changed based on the frequency.
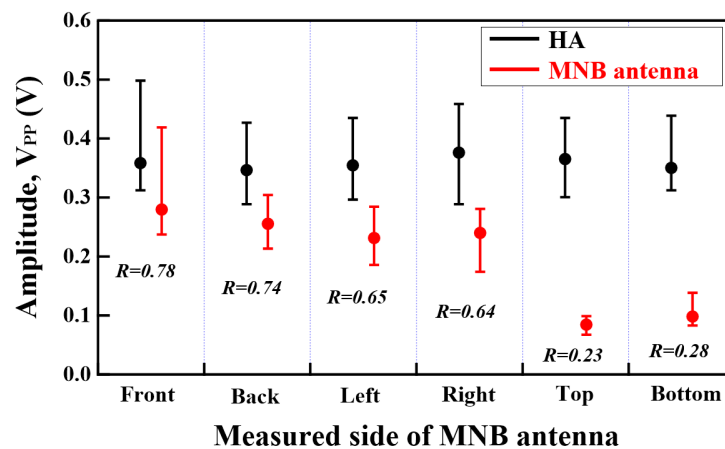
Fig. 4.8 The V_{PP} of the measured signal depends on the side of the MNB antenna

(R - Ratio of V_{PP}; V_{PP_MNB}/V_{PP_HA})

Fig. 4.9 shows the normalized V_{PP} of the MNB antenna based on the front side result. The measurement result agrees with the simulated radiation pattern, shown in Fig. 3.19. The MNB antenna receives the EM wave with a relatively higher value through the Z and X-axis (front, back, and side views), while the detection ability is relatively low for Y-axis (top and bottom). Based on this characteristic, the MNB antenna can be used for PD location detection as a multiple sensors system. In addition, the directivity of the MNB

antenna can be adjusted using an additional device such as a cavity box, depending on the purpose.
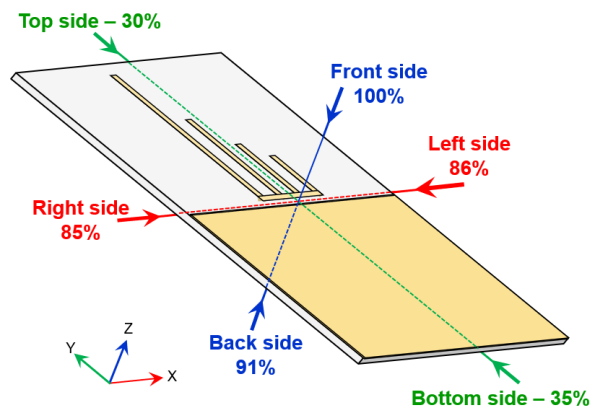
Fig. 4.9 Measured directivity of the MNB antenna against the BD signals.

(Normalized based on the front value)

4.3   Partial discharge detection

PD is a pre-breakdown phenomenon, so that PD detection gives a chance to estimate the insulation condition and avoid electric failure. PD detection is more complicated than BD detection in the UHF method because of the low intensity and random repetition of EM waves. Therefore, the RF preamplifier is used for PD measurement. The PD types and classifications were mentioned in Chapter 1. This section discusses the MNB antenna's PD detection ability based on experimental results. The MNB antenna has been developed for detecting PD in SF_6 gas. So, first, the MNB antenna was applied to measure PD in SF_6 gas and compared with HA [3]. After that, the MNB antenna was applied for PD detection in atmospheric air and solid XLPE insulation to understand the detection abilities of the MNB antenna for PD in different insulation. All experiments were carried out in an anechoic room as an open area, meaning the PD emitted EM wave was propagated in a transverse electromagnetic (TEM) mode. The waveguide propagation effect was excluded because the propagation is changed based on the HV equipment's size [4].

4.3.1 Partial discharge in SF_6 gas detection

The EM wave emitted from PD in SF_6 gas was measured by the MNB antenna and HA. Figs. 4.10 shows the photograph of the experimental setup for the PD in SF_6 gas and the PD signal emitted from the needle plate system and antennas located 1 meter from the PD source. The detail of the experimental setup, background measurement, and environmental conditions was discussed in Chapter 2.
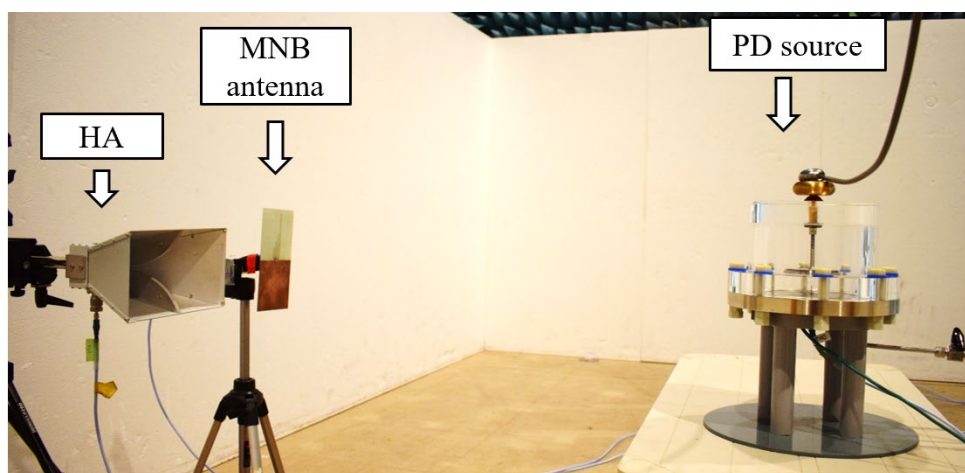
Fig. 4.10   Photograph of the experiment setup of PD in SF_6 gas

The typically measured waveforms are shown in Fig. 4.11. The background noise was noticeable low due to the anechoic room measurement, and both the HA and the MNB antenna can measure the PD signal in SF_6 gas. Even if the EM wave V_{PP} were different for the antennas, the waveforms are seemed similar from the expanded graph, as shown in Fig. 4.11 (b). Also, the PD signal amplitude was similar to the BD signal because of the RF amplifier (25 dB) used for PD measurement.

(a) Whole waveforms

(b) Expanded waveforms at the PD pulse of (a)
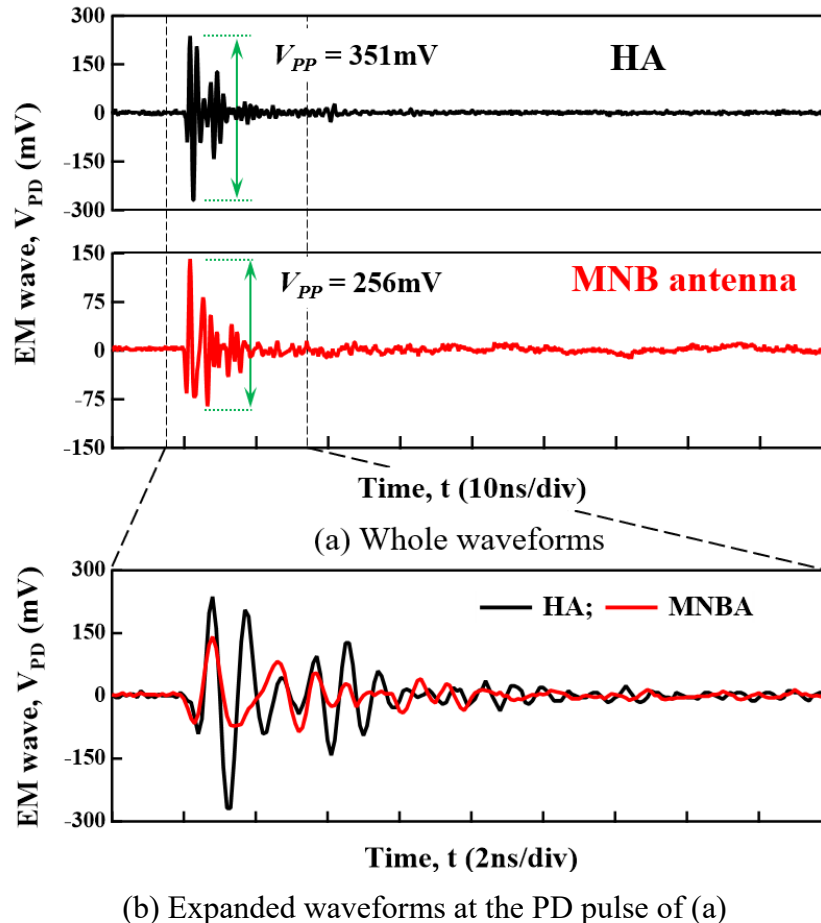
Fig. 4.11　　Simultaneously measured waveforms of PD signal in SF_6 gas by the MNB antenna and HA

The relation of the V_{PP_HA} and V_{PP_MNB} are shown in Fig. 4.12 for the PD signal. The slope coefficients, a, of the PD in SF_6 gas was 0.43, lower than that of BD. The slope reduction is related to the discharge phenomena because the BD and PD emitted signals have different frequency components. However, the correlation coefficients, r, of the V_{PP} are high enough as 0.94 and 0.85 for both the PD and BD, respectively. It means that the MNB antenna is available to detect PD signal similar to BD signal even though the amplitude of the measured EM wave by the MNB antenna is lower than the HA; thus, the slope reduction can be fixed by using the preamplifier.
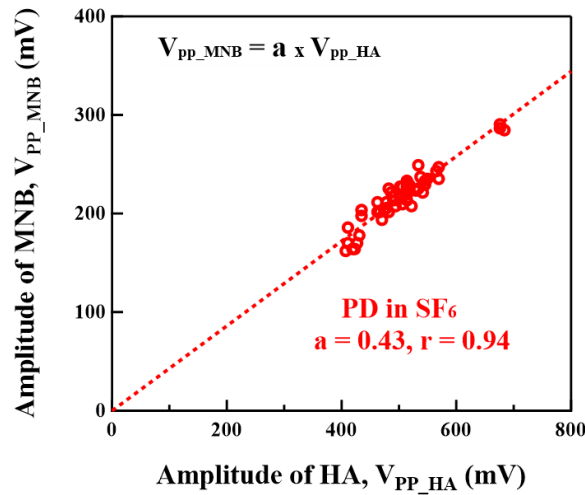
Fig. 4.12   Relation of the peak to peak amplitude of the measured EM wave
between the MNB antenna and the HA

The frequency properties of the MNB antenna on PD in SF_6 detection were further investigated because the PD phenomena have a scatter due to their nature. Fig. 4.13 shows the averaged frequency spectra of the 50 measurement results taking the PD volatility into consideration. The f_d and f_e represent the designed detection and elimination frequencies of the MNB antenna.
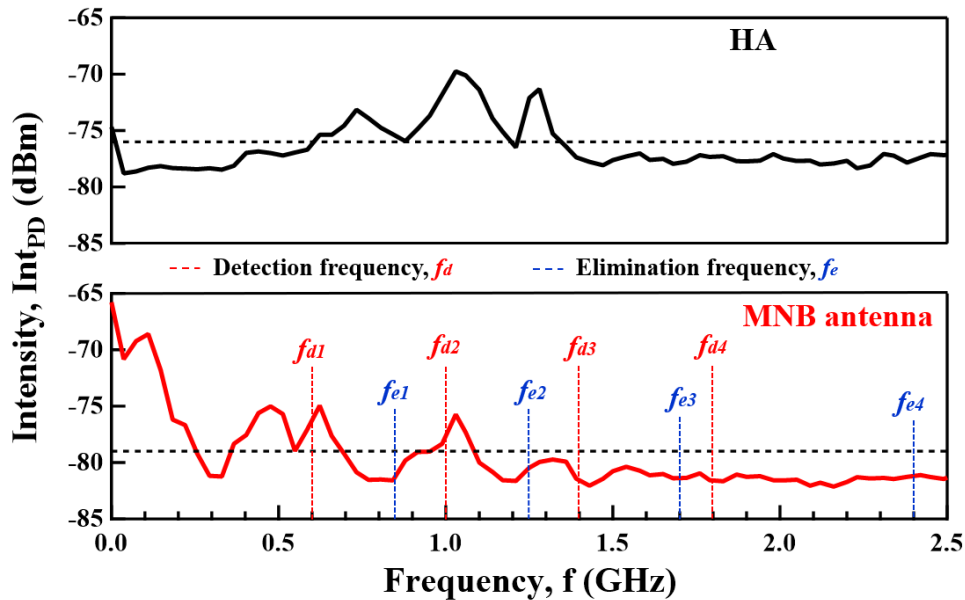
Fig. 4.13   The averaged frequency spectrum of the 50 times PD signal in SF_6 gas

As seen in Fig. 4.13, the intensities at the elimination frequencies showed local minimum values while those at the detection frequencies showed local maximum values except the fourth resonant frequency. From the measured result of HA, it seems that the intensity of PD is originally insufficient at the fourth resonant frequency.

4.3.2 Partial discharge in dry air detection

The discharge in dry air could be considered the signal or noise for the PD detection system. Air has good insulation properties under dry, clean, and compressed conditions, making it an ideal solution for switchgear insulation. For example, the Mitsubishi Electric Co. developed the dry-air insulated switchgear, Cubicle types Gas Insulated Switchgear (C-GIS), for medium voltage distribution [5]. In this case, the PD in dry air is considered a discharge signal. Another hand, the PD in dry air (corona discharge), which is one of the common discharge types in HV equipment, can affect the PD detection system as noise. For this reason, the difference between PD in SF_6 and dry air is an interesting point. Therefore, it needs to determine whether the MNB antenna can discriminate the PD in dry air and SF_6 gas. The MNB antenna was applied to measure PD in dry air. The experiment setup was the same as PD in SF_6 gas except for the applied voltage lower than PD in SF_6 gas, around 12 kV. Fig. 4.14 shows typically measured EM waveforms of PD in dry air measured by MNB antenna and HA.
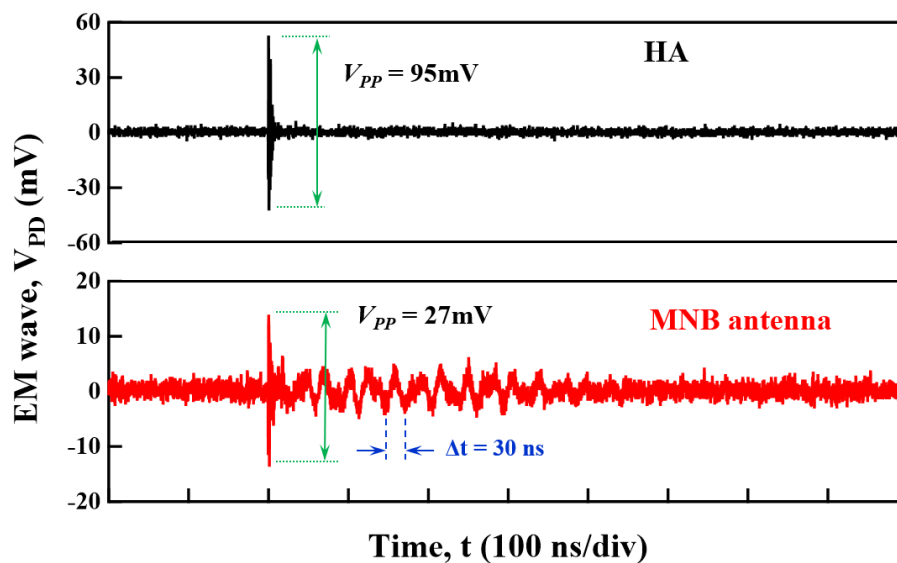
Fig. 4.14   Simultaneously measured waveforms of PD signal in the air by the MNB antenna and HA

The amplitude of EM wave is lower than PD in SF_6 gas because the main frequency band of EM wave emitted in the air is lower than 300 MHz, which is lower than the detection frequency of both antennas and operation frequency band of RF amplifier. However, it is shown that the MNB antenna received some lower frequency signal and the period of lower frequency signal is around 20~40 ns. It means the main frequency band of PD in the dry air is around 25~50 MHz.

The averaged frequency property of 100 times measurement results is shown in Fig. 4.15. As expected, the PD in dry air emits the lower frequency signal, around 50 MHz, because the dielectric constant of the dry air is lower than SF_6 gas. It means the PD current of dry air, causing the EM wave, has a higher rise time than the SF_6 gas. However, there is no high intensity at a lower frequency for HA's result. It could be related to the antenna property and effect of the RF amplifier. For MNB antenna, it has resistance from the low-frequency signal. But, it does not mean the MNB antenna does not receive the noise signal. The MNB antenna receives the elimination frequencies but with low amplitudes.
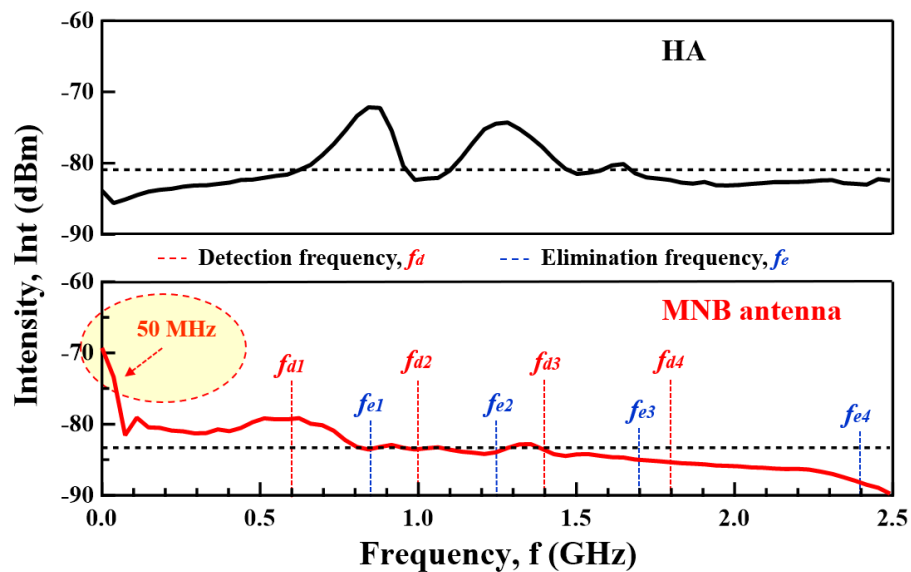
Fig. 4.15　　　The averaged frequency spectrum of the 100 times PD signal in the air

In addition, the main frequency component of PD in the air can be predicted from the frequency property of HA. At 0.85 GHz and 1.3 GHz, the intensity is touched highest point, and those frequencies are elimination frequencies of MNB antenna. Fig. 4.16 displays the relation between V_{PP} of PD in dry measured by MNB antenna and HA. Due to the mismatching of the detection frequency of MNB and frequency component of PD in dry air, the V_{PP} of the MNB antenna is much lower than that of HA. So, the slope and correlation between V_{PP} are reduced up to 0.33 and 0.88, respectively [6].
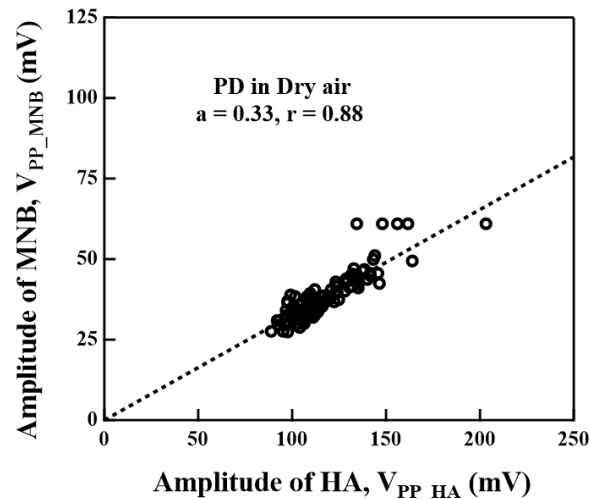
Fig. 4.16   Relation between the peak to peak amplitude of MNB antenna and the HA for PD in dry air

4.3.3 Partial discharge in XLPE insulation as an electric tree

The electric power cable is one of the main parts of the electric power system. Recently, major big cities have suffered from heavily congested roads and substructures, and as a result, the use of high voltage cables has become ever more popular. The XLPE insulation is commonly used for medium and high voltage cable systems because of low dissipation, low dielectric constant, good thermo-mechanical property, and high operating temperature and pressure. As the majority of dielectric failures in the HV XLPE cable systems can be assigned to the defects in the electrical insulation system of accessories, PDs are continuously monitored at all joints and terminations [7]. In addition, the many GIS connected to the electric system using cable terminations. The PD in XLPE insulation in cable accessories and PD in SF_6 gas in GIS can affect each other. Therefore, this section reports the experiment result of the MNB antenna for the PD in XLPE insulation.

The block sample of XLPE insulation used in this study was made with a metal protrusion as an electric tree defect by Sumitomo electrical industries in Japan. The XLPE insulation material and making way are high identity with real XLPE insulated power cable. In addition, the partial discharge properties in the XLPE block sample with electric tree defect and difference in charge of PD properties observed between IEC60270 and the UHF method were introduced in [8].

Fig. 4.17 shows the photo of the experimental setup, same as the previous experiment except for the RF amplifier. PD in XLPE measurement did not use the RF amplifier for a safety reason because the applied voltage develops the electric tree and could start BD.
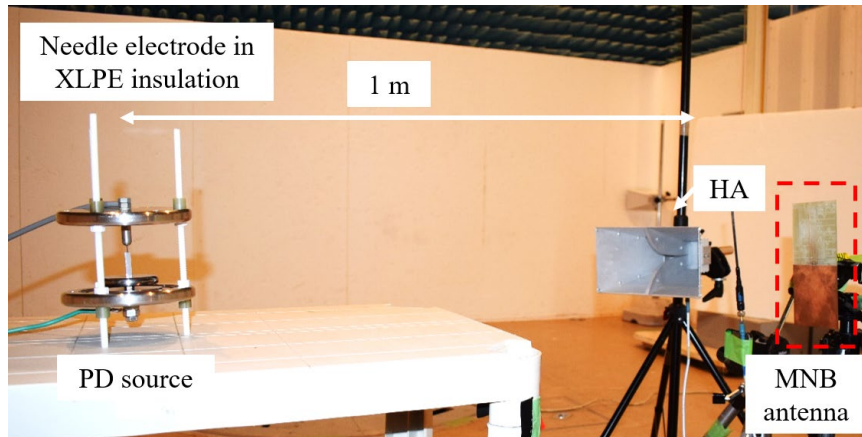
Fig. 4.17   Photograph of the experiment setup of PD in XLPE insulation

The typically measured EM waves of PD in XLPE are shown in Fig. 4.18. From the measured result, both antennas can catch the PD in XLPE. The V_{PP} ratio was around 2.7. In addition, the EM wave measured by the MNB antenna has an eye-catching lower frequency band component. However, Fig. 4.18 (b) shows that the front parts of EM wave shapes measured by both antennas have a similar trend.
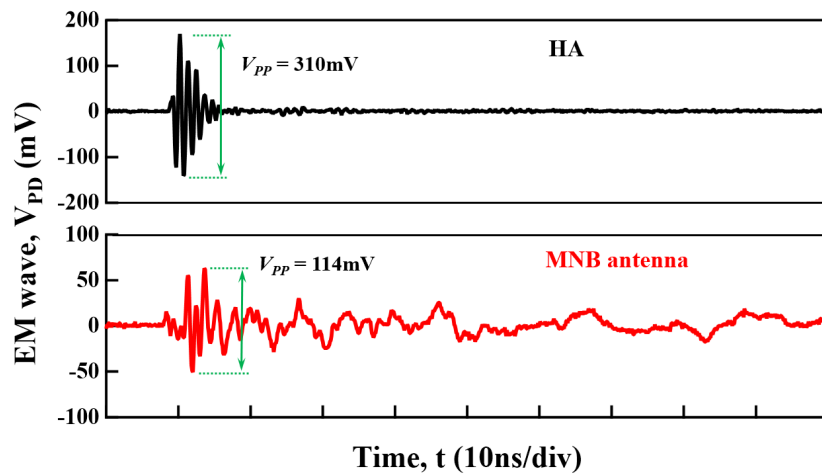
(a) whole EM waveforms
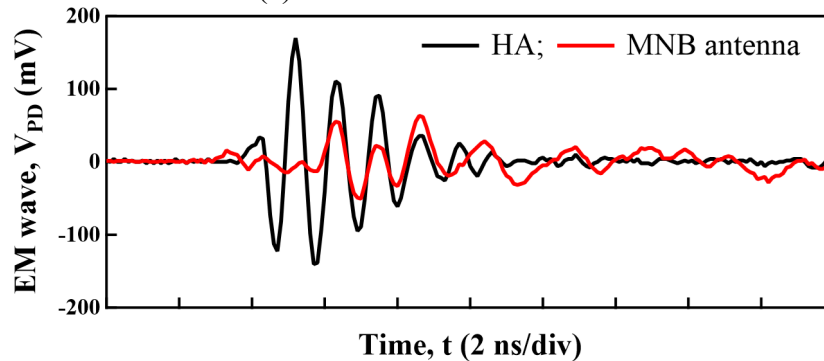
(b) Expanded waveforms at the PD pulse of (a)

Fig. 4.18   EM waveform of PD in XLPE insulator

Fig. 4.19 shows the average frequency spectrum of 50 times measured PD emitted signal in XLPE insulation. The PD in XLPE insulation emitted the EM wave, and the main component of the EM wave was from 0.65 GHz to 1.02 GHz. However, the MNB antenna has a high component at a low frequency, lower than 0.5 GHz. It seems that the nature of PD in XLPE insulation emits the EM wave from a few tent MHz to 1.0 GHz frequency range. The HA could not detect the lower frequency band due to the detection frequency range.
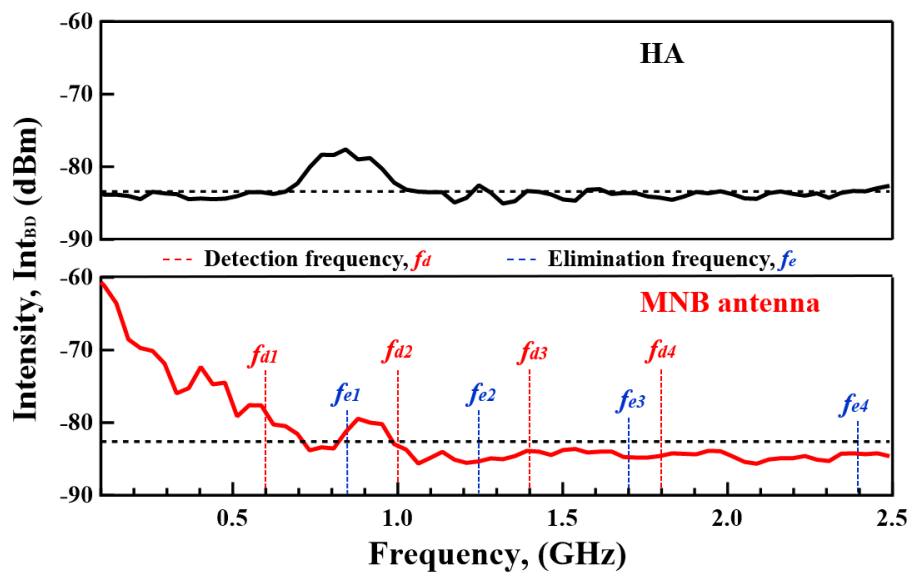
Fig. 4.19   The averaged frequency spectrum of the 50 times PD signal in the XLPE insulator

4.3.4 Comparison of discharge detection

The MNB antenna was able to detect the BD and PD in different insulation mediums, and the V_{PP} of measured EM wave compared with that of HA in Fig. 4.20. The slope of relations is different based on the discharge types because of the frequency component. The BD measurement result indicates the highest slope and V_{PP} for MNB antenna because the main frequency component of BD occurred from 0.6 GHz to 1.5 GHz and intensity was noticeably higher than PD signals. If the detection frequency band of the MNB antenna is matched with the frequency band of target types discharge, the V_{PP} of EM wave is increased, such as PD in SF_6 gas. In addition, the correlation coefficient between V_{PP} of EM waves was measured by two antennas, which means the MNB antenna detects the discharge similar to HA.
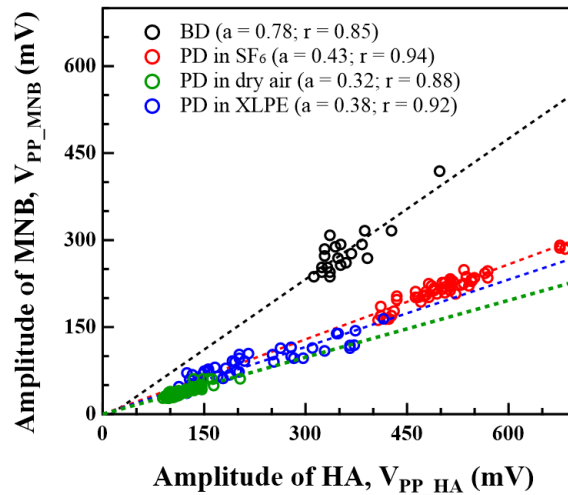
Fig. 4.20 Relation between the peak to peak amplitude of MNB antenna and HA

The main frequency components of discharge emitted EM wave is changed on discharge's original character. Fig. 4.21 (a) and (b) show the comparison of frequency components of BD and PDs for HA and MNB antenna, respectively. The dashed line shows the averaged intensity at the whole frequency to simply determine a higher component. The frequency spectrum of EM wave measured by HA shows the original frequency characteristic of BD and PDs except for the frequency band lower than 0.7 GHz because the frequency response of HA is wide and flat from 0.7 GHz to 5 GHz. In comparison, the MNB antenna has a multiple-narrow detection frequency. Thus, the highest intensity was detected at detection frequencies for the MNB antenna.

(a) HA (b) MNB antenna
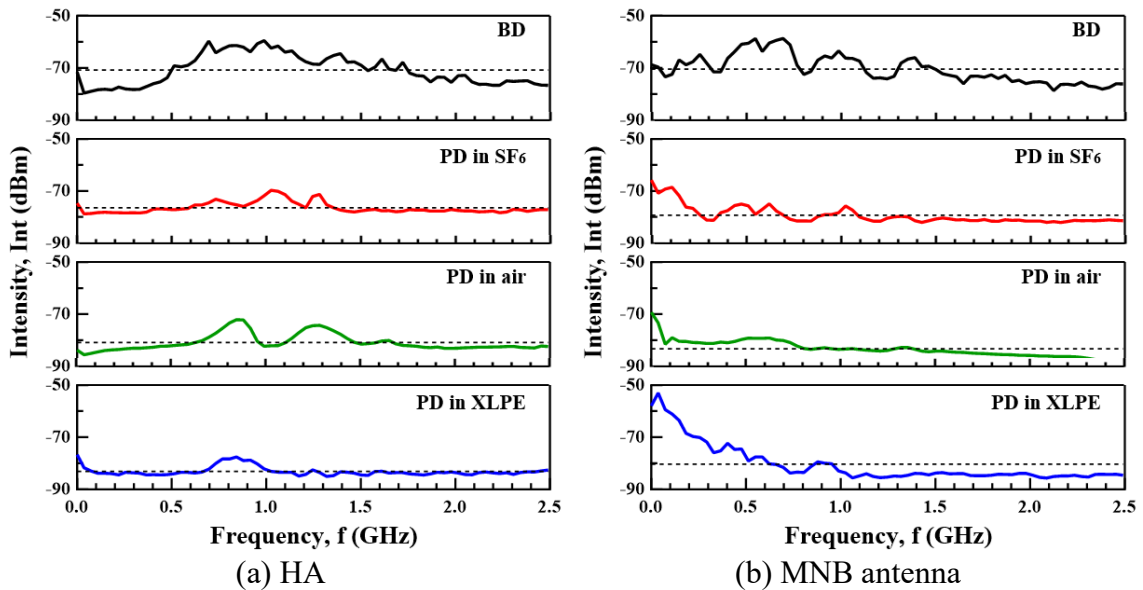
Fig. 4.21 The averaged frequency spectrum of the BD and PD signals

In addition, PD in air and XLPE insulation emits the EM wave with the noticeable high component at a frequency lower than 0.5 GHz. Even if that frequency band is not the detection frequency of MNB antenna, that detected the PD emitted signal at a frequency lower than 0.7 GHz due to remarkable high intensity. The main frequency components are shown in table 4.1.

Table 4.1. The main frequency band of discharge for each antenna

#	Discharge	Frequency range (GHz)	
		HA	MNB antenna
1	BD	0.6 ~ 1.5; 1.6; 1.7	0.12 ~ 0.3; 0.4 ~ 0.77; 0.88 ~ 1.13; 1.3 ~ 1.5
2	PD in SF6	0.6 ~ 1.4	< 0.26; 0.37 ~ 0.7; 0.9 ~1.1
3	PD in air	0.7 ~ 0.95; 1.1 ~ 1.45	< 0.8; 0.8 ~1.1; 1.3 ~1.4
4	PD in XLPE	0.7 ~ 1.0	< 0.65; 0.88 ~ 0.95

4.4   Conclusion

The following conclusions were obtained based on the experimental result of discharge detection:

1.   The MNB antenna can be fabricated with different BW and detection frequencies, and discharge detection ability was directly related to the detection BW and frequencies of the antenna.

2.   The measurement result demonstrated that the MNB antenna has good omnidirectional directivity, the same pattern as the theory. The MNB antenna can be placed at the bottom or side of the wall in the HV equipment for PD detection because of the directivity and electric field detection.

3.   The MNB antenna can detect different PD signals from the different insulations and discharge types, and the signal intensity, *i.e.,* the peak to peak amplitude of the antenna output, of the MNB antenna showed a good correlation with that of the HA.

4.   Due to the elimination frequency, the MNB antenna received the EM wave with a slightly lower amplitude than HA. However, the slope between V_{PP} could be adjusted using the RF amplifier because the correlation coefficient is high enough.

5.   The frequency spectrum and V_{PP} of the measured EM wave were changed depending on the insulation. The MNB antenna can be developed for different PD emitted signals by changing the detection frequency bands.

References

[1]   S. Tenbohlen, D. Denissov, S. M. Hoek, and S. M. Markalous, "Partial discharge measurement in the ultra high frequency (UHF) range," *IEEE Trans. Dielectr. Electr. Insul.*, Vol. 15, No. 6, pp. 1544–1552, 2008.

[2]   T. Bandi and S. Ohtsuka, "A Multiple Narrow Band Antenna for Detection of Discharge-Emitted Electromagnetic Waves for Insulation Diagnostic," *IEEJ Trans. Electr. Electron. Eng.*, Vol. 15, No. 12, pp. 1751–1757.

[3]   T. Bandi, M. Tanaka, H. Furuie, and S. Ohtsuka, "Developing of Multiple-narrowband Antenna to Detect Partial Discharge-emitted Signal under Radio Communication Noise Environment," *Proceeding - 8th Int. Conf. Cond. Monit. Diagnosis, C. 2020*, pp. 154–157, 2020.

[4]   T. Fujimoto, S. Ohtsuka, and T. Shikura, "FDTD Analysis on Propagation and TE Mode Properties of PD-Emitted Electromagnetic Wave in Three-Phase Type GIS with a Series Arrangement of HVCs," *IEEJ Trans. Electr. Electron. Eng.*, Vol. 16, No. 12, pp. 1687–1692, 2021.

[5]   S. Sato, K. Koyama, N. Inoue, M. Arioka, and M. Uenushi, "Development of Compressed Air Insulation Technology for C-GIS," *IEEJ Trans. Power Energy*, Vol. 124, No. 9, pp. 1132–1138, 2004.

[6]   T. Bandi and S. Ohtsuka, "Application of MNB antenna for Discriminating between Partial Discharges in Dry Air and SF 6 Gas," in *The 73rd Joint Conference of Electrical, Electronics and Information Engineers in Kyushu*, 2020, Vol. 2020 02–2P, p. 366.

[7]   S. Dhara, C. Koley, and S. Chakravorti, "Detection of PD Activities in XLPE Cable Using UHF Antennas," *4th Int. Conf. Cond. Assess. Tech. Electr. Syst. CATCON 2019*, pp. 26–29, 2019.

[8]   H. Furuie, T. Yamauchi, and S. Ohtsuka, "Partial Discharge Properties in XLPE Block Sample with Electric Tree Defect and Difference in Charge of PD Properties Observed between IEC60270 and the UHF Method," *Proceeding - 8th Int. Conf. Cond. Monit. Diagnosis, C. 2020*, pp. 158–161, 2020.

Chapter 5
Noise resistance properties of MNB antenna

5.1   Introduction

With the development of information and communication society, it is important to understand the interference of the communication signal for each field as electromagnetic compatibility (EMC). Especially for the UHF method, the communication and radio signals work as electromagnetic interference (EMI) and noise because the UHF band includes many communication, radio, and ISM bands. Fortunately, communication noises are commonly emitted in narrow bands as a line spectrum. Therefore, the MNB antenna was developed to detect the partial discharge (PD) signal with high noise resistance for selected narrow noise bands. Chapter 4 confirmed that the MNB antenna has excellent detection ability for PD in SF_6 gas.

In this section, the noise resistance property of the MNB antenna is investigated experimentally. The MNB antenna is applied to measure the PD in SF_6 gas under the communication noise. The communication noise is generated by SG and HA artificially or by the commercial drone (Bebop-2) as the 2.4 GHz frequency Wi-Fi noise [1-2]. The experiment setup and measurement devices were discussed in Chapter 2.

5.2   Artificial noise resistance

In this section, the MNB antenna was applied to measure PD in SF_6 gas under some artificial noises emitted from the signal generator through the emission HA, and measurement results compared with a receiver HA. The photo of the experimental setup is shown in Fig. 5.1. The PD signal in SF_6 gas under artificial noise was measured 50 times whenever the frequency of artificial noise was changed. The artificial noise was emitted from a signal generator (SG), and amplitude was fixed at 300 mV. As introduced in Chapter 3, the MNB antenna was designed with four detection and four elimination frequencies. Therefore, the artificial noise frequencies were selected from the reflection loss graph of the MNB antenna as detection and elimination frequencies of the antenna, as shown in Fig. 5.2. The selected frequencies and reflection loss of them are shown in Table 5.1. The receiver HA's measurement results are used as a reference.
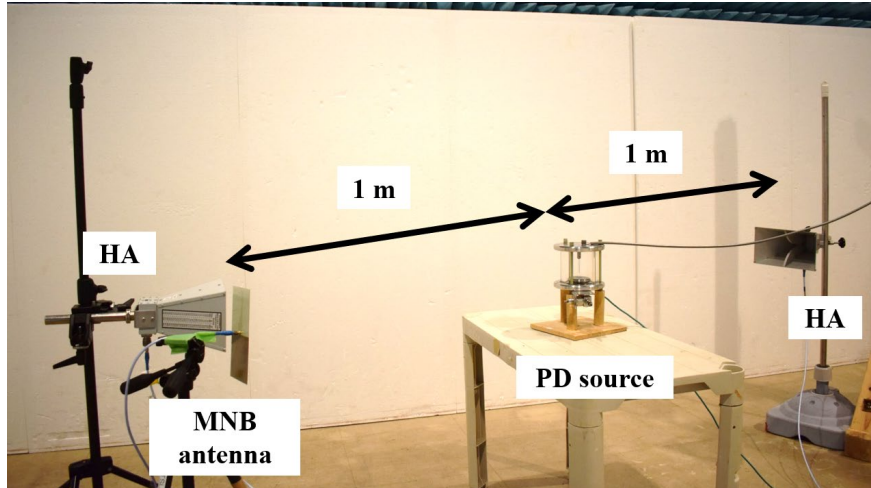
Fig. 5.1 Photograph of the experiment setup of PD in SF_6 gas under artificial noise
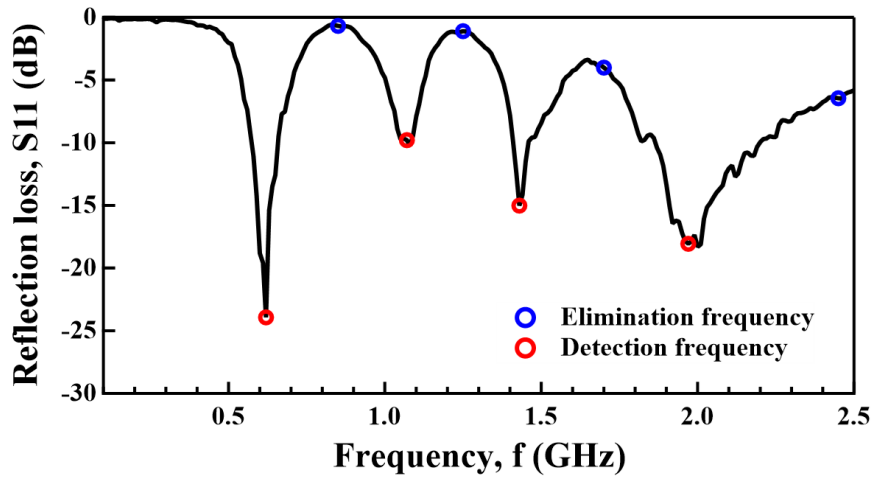
Fig. 5.2   The frequency selection of artificial noise from MNB antenna's reflection loss

Table 5.1. Frequency selection for the artificial noise

	Elimination frequencies, f_e				Detection frequencies, f_d			
Frequency, f (GHz)	0.85	1.23	1.70	2.40	0.62	1.07	1.43	1.97
Reflection loss, S11 (dB)	-0.67	-1.21	-4.01	-6.76	-23.9	-9.79	-15.0	-18.1

5.2.1 Artificial noise agrees with the detection frequency of MNB antenna

First, the artificial noise was fixed the same as the detection frequency of the MNB antenna. Figs. 5.3 (a) to (d) show the simultaneously measured waveforms by the HA and the MNB antennas under the artificial noise conditions. In these figures, V_S and V_N represent the peak to peak amplitude of the PD signal and artificial noise, respectively. The V_N was almost constant in the figure due to the constant emission by SG, and the difference in the relation between V_S and V_N appeared depending on the noise frequency.
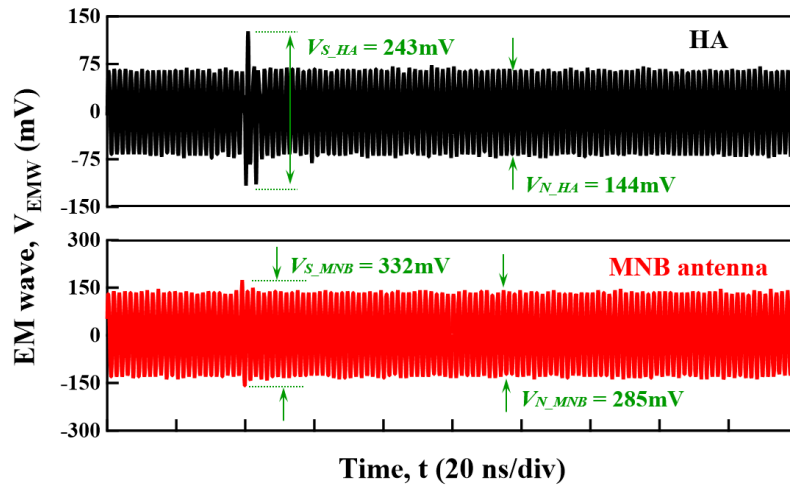
(a) when artificial noise f_{d1} = 0.62 GHz
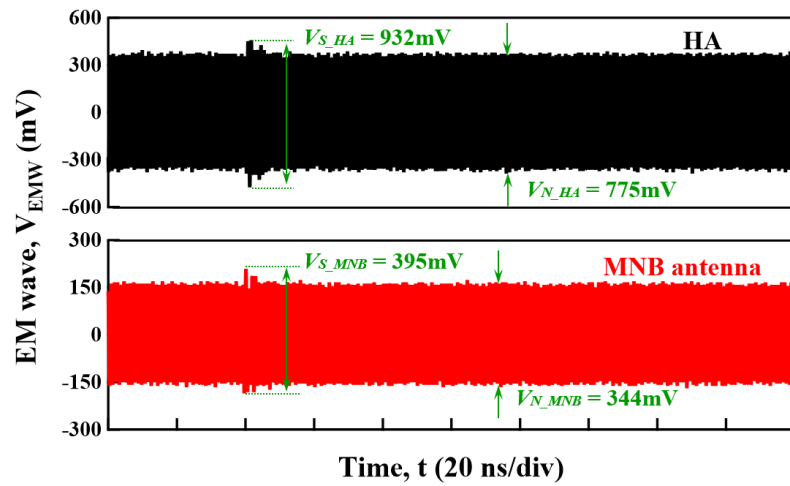
(b) when artificial noise f_{d2} = 1.07 GHz
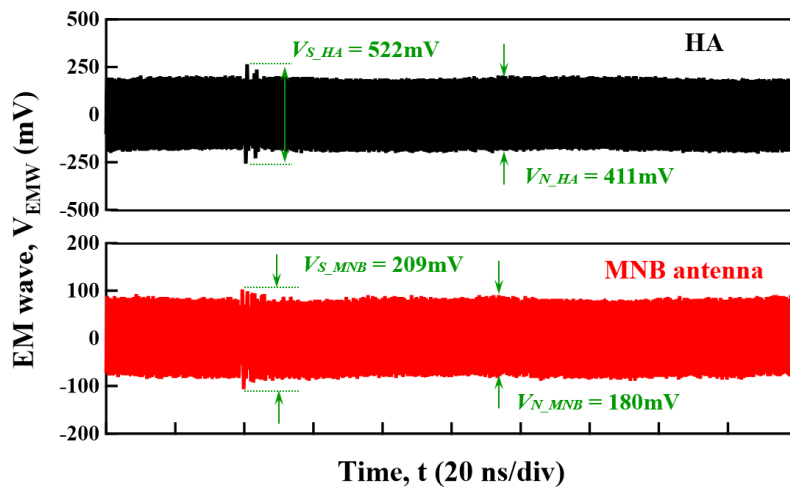
(c) when artificial noise f_{d3} = 1.43 GHz

Fig. 5.3 EM waveshape of PD in SF$_6$ gas under the artificial noise (detection frequencies of MNB antenna) (continued on the following page)
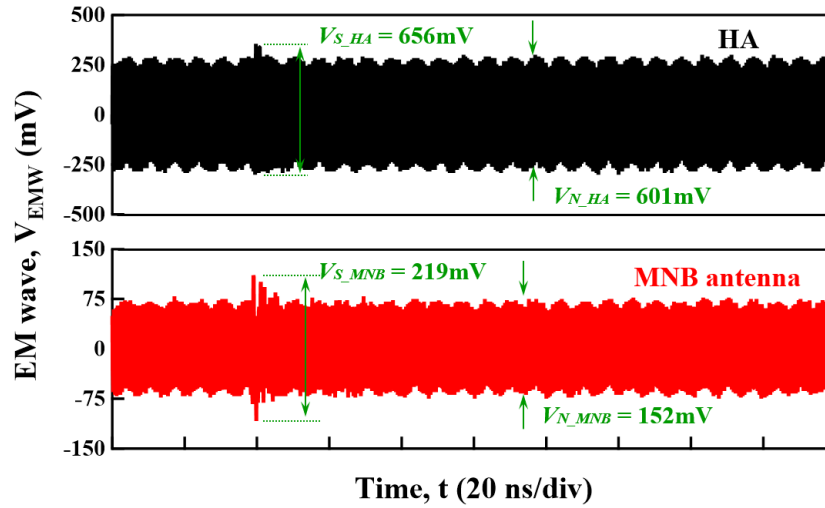
(d) when artificial noise f_{d4} = 1.97 GHz

Fig. 5.3 EM waveshape of PD in SF$_6$ gas under the artificial noise (detection frequencies of MNB antenna)

The amplitude of PD in SF$_6$ gas under the artificial noise, V_S, was much higher than the V_{PP} of just PD in SF$_6$ gas in Chapter 4 because of the superimposed waveforms of PD signal and noise. For example, under the 0.62 GHz artificial noise, the V_{S_MNB} antenna was 1.4 times higher than V_{S_HA} because of the superimposed result. The 0.62 GHz is lower than the detection frequency of HA thus; MNB antenna received the artificial noise with higher amplitude more than HA. Fig. 5.4 shows the signal-noise ratio (SNR) of PD in SF$_6$ gas under the artificial noise, changed as detection frequencies of MNB antenna.
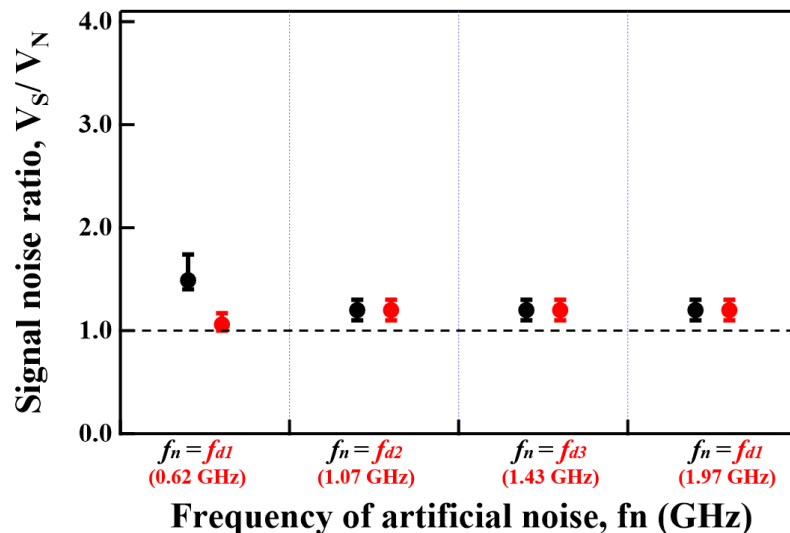
Fig. 5.4 The signal-noise ratio of PD in SF$_6$ gas under the different artificial noise (detection frequencies of MNB antenna)

The SNR was around 1.3 under detection frequencies noise for both antennas except when artificial noise frequency was 0.62 GHz. It means the MNB antenna can detect the

PD signal same as HA under the noise, whose frequency agrees with the detection frequency of the MNB antenna.

5.2.2 Artificial noise agrees with the elimination frequency of MNB antenna

The previous section showed that the MNB antenna could detect the PD signal under the detection frequency noise with SNR same as HA. In this section, the SNR was investigated under the noise whose frequency was changed as elimination frequencies of the MNB antenna. Figs. 5.5 (a) to (d) show the simultaneously measured waveforms by the HA and the MNB antennas. The V_{S_HA} is noticeably higher than V_{S_MNB} because of the superimposed components. The V_{N_MNB} is relatively lower than V_{N_HA} compared with the difference between V_{S_MNB} and V_{S_HA} due to the high noise resistance ability of the MNB antenna.
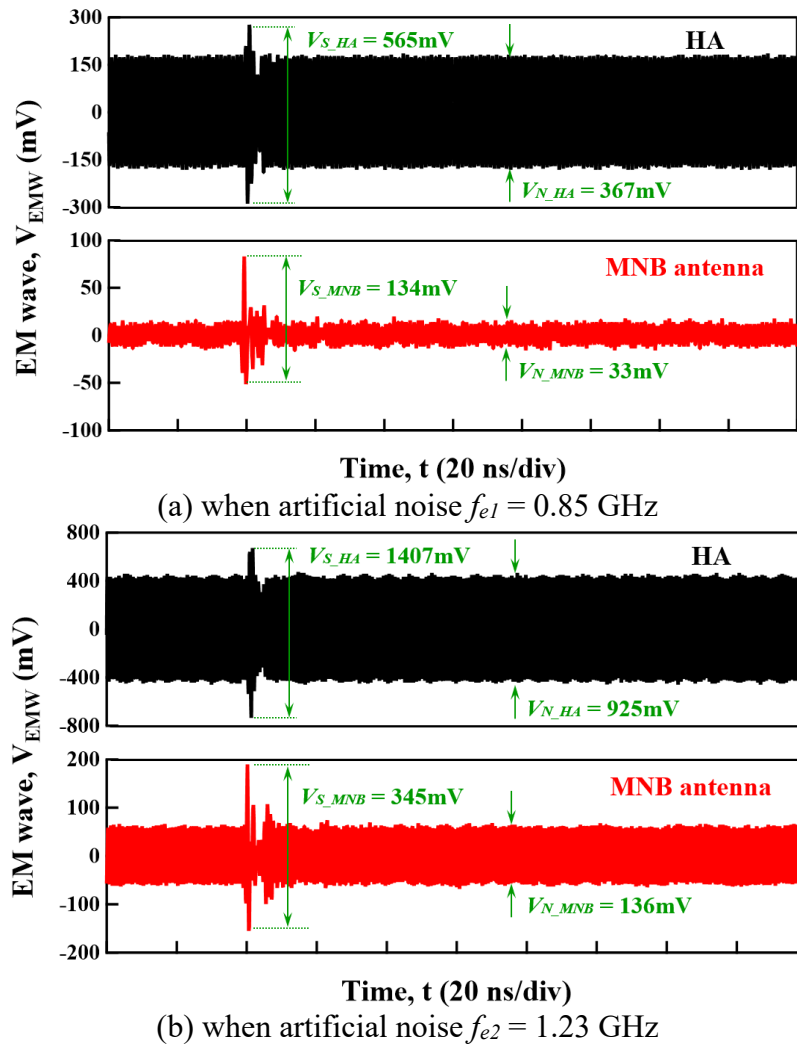
(a) when artificial noise f_{e1} = 0.85 GHz

(b) when artificial noise f_{e2} = 1.23 GHz

Fig. 5.5 EM waveshape of PD in SF$_6$ gas under the artificial noise (elimination frequencies of MNB antenna) (continued on the following page)
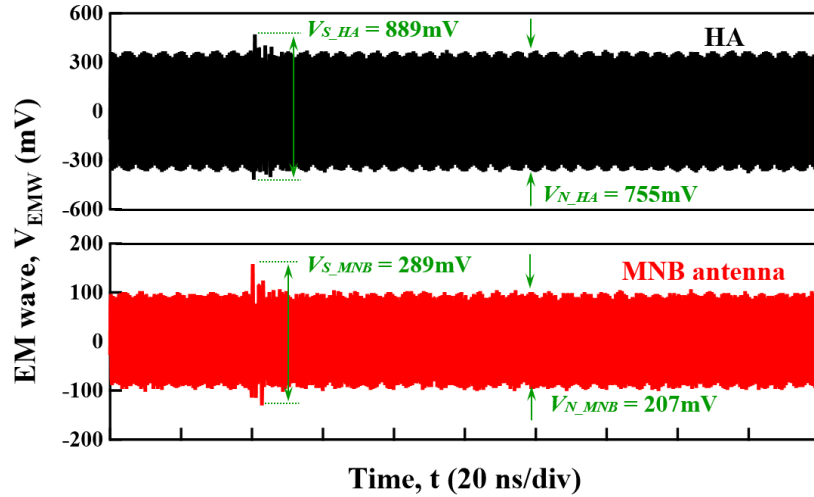
(c) when artificial noise f_{e3} = 1.7 GHz
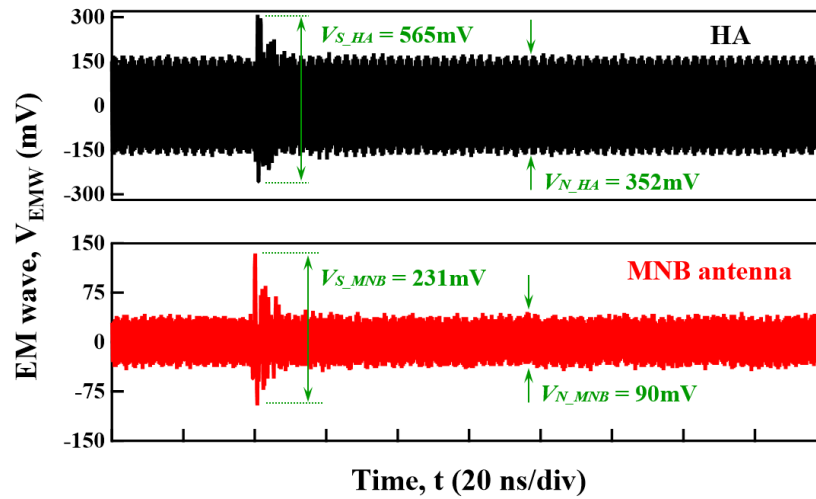
(d) when artificial noise f_{e4} = 2.4 GHz

Fig. 5.5 EM waveshape of PD in SF$_6$ gas under the artificial noise (elimination frequencies of MNB antenna)

Consequently, Fig. 5.6 shows the SNR of both antennas when the noise frequency agrees with the detection frequency of the MNB antenna. The SNR of HA was around 1.3 same as Fig 5.3 at each frequency. In contrast, the SNR of the MNB antenna was drastically higher than that of HA because of the noticeable low noise. It means the detection ability of the MNB antenna is much higher than HA under the elimination frequency noise.
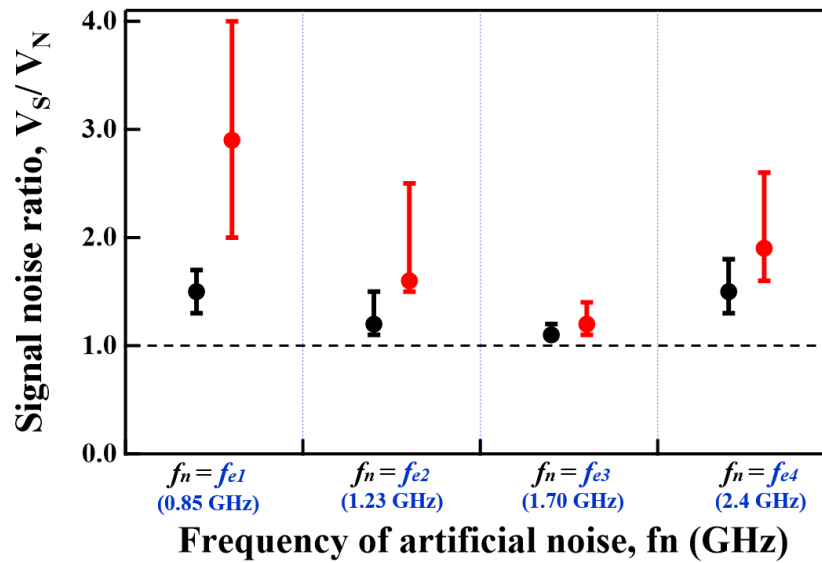
Fig. 5.6 The signal-noise ratio of PD in SF$_6$ gas under the different artificial noise
(elimination frequencies of MNB antenna)

5.3   Actual Wi-Fi noise resistance property

The MNB antenna gave a high SNR for PD detection under artificial noises. In this section, PD detection property under an actual Wi-Fi noise, 2.4 GHz, is further investigated [2]. The Wi-Fi noise is the important frequency band for electric devices because of a wireless connection and IoT technology [3], thus, selected as the elimination frequency of the MNB antenna. In addition, the high resistance of the Wi-Fi noise allows the MNB antenna can cooperate with other digital devices and technology as smart UHF sensors in digital substations [4].

Fig. 5.7 shows the photo of the experimental setup that used PD measurement under the Wi-Fi noise. The Wi-Fi noise was generated by a commercial drone (Bebop-2, drone noise), located 4 m away from the receiver antennas. The drone's distance was decided for the HA so that the amplitude values of the PD signal became slightly lower than that of the drone noise. Namely, the SNR becomes lower than 1, which corresponds to a severe condition of PD detection. First, both antennas measured the PD signal and then drone noise independently to compare the original characteristic of signal and noise. Figs 5.8 (a) and (b) show the difference in the PD signal's typical waveforms and the drone noise. As mentioned above, the amplitude of the PD signal was lower than that of the drone noise measured by the HA, as in Fig. 5.8 (a).
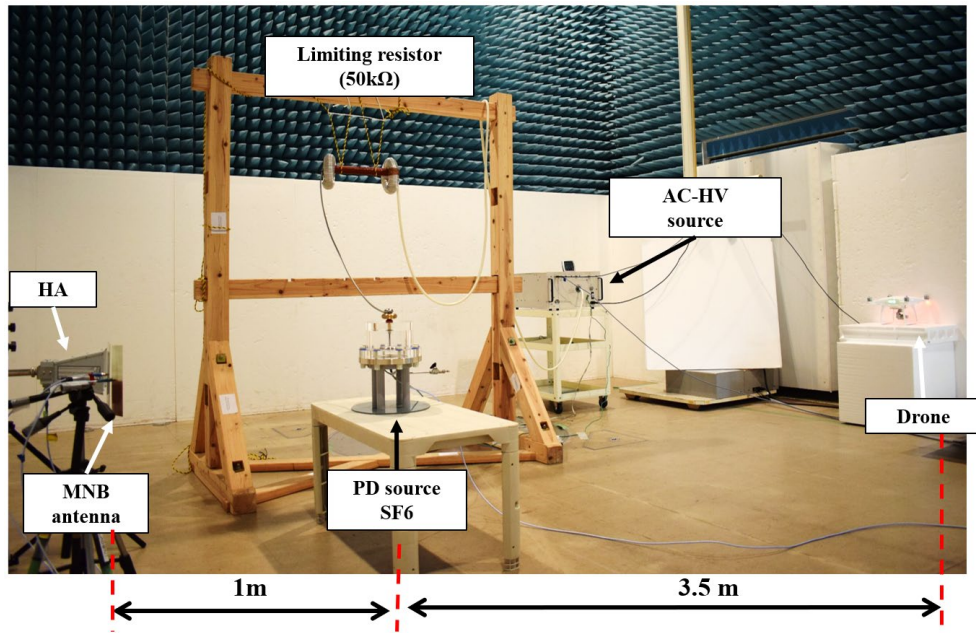
Fig. 5.7 Experiment setup to measure the PD signal under the Wi-Fi noise
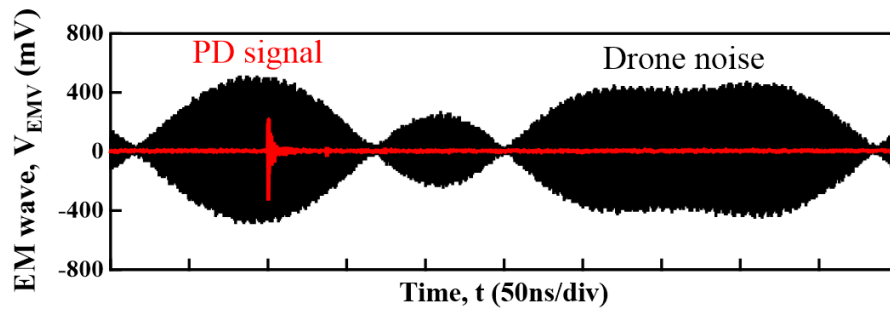
(a) EM waveforms measured by HA
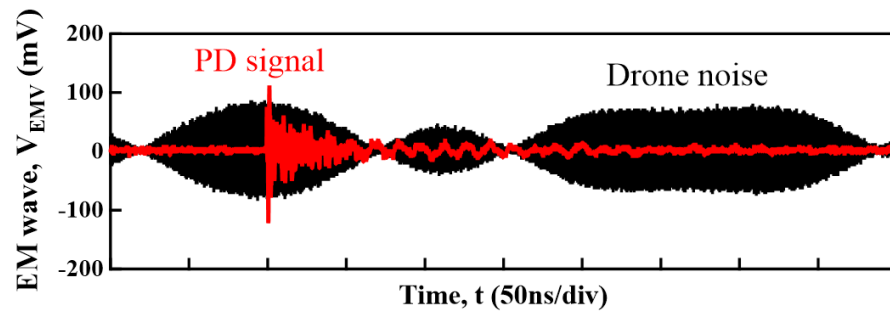
(b) EM waveforms measured by MNB antenna

Fig. 5.8 Independently measured waveforms of PD signal and drone noise

In addition, the spectrum responses of drone noise measured by both antennas are shown in Fig. 5.9. The MNB antenna reduced the drone noise by around 16.6 dBm. Therefore, the amplitude of the PD signal was higher than the drone noise for the MNB antenna, as in Fig. 5.8 (b). The advantage of the MNB antenna on the PD detection under the Wi-Fi noise environment is discussed based on the independent measurement below.
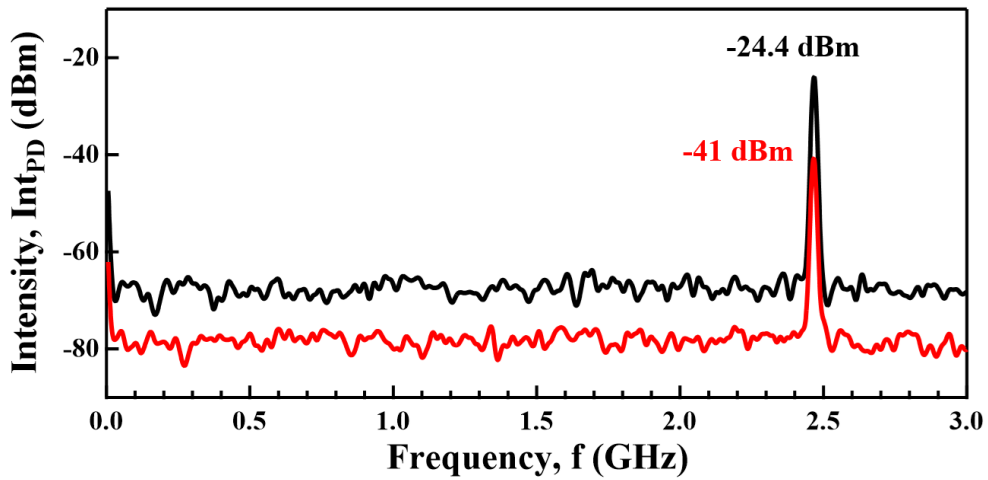
Fig. 5.9 The frequency spectrum of drone noise measured by HA and MNB antennas

Fig. 5.10 shows the relation between peak-to-peak amplitudes V_{PP} of the PD signal and the drone noise measured by the two antennas, and the 50 times measurement results were plotted. The slope coefficient of the PD signal (0.38) was larger than that of the drone noise (0.16). This means that the reduction in the amplitude V_{PP} of the drone noise is larger than that of the PD signal for the MNB antenna. In addition, in this experimental condition, the SNR of the MNB antenna became larger than that of the HA and over one, i.e., improvement of the SNR of the PD detection ability up to 1.4 as shown in Fig. 5.11 where the SNR of HA was slightly lower than 1 (SNR=0.6).
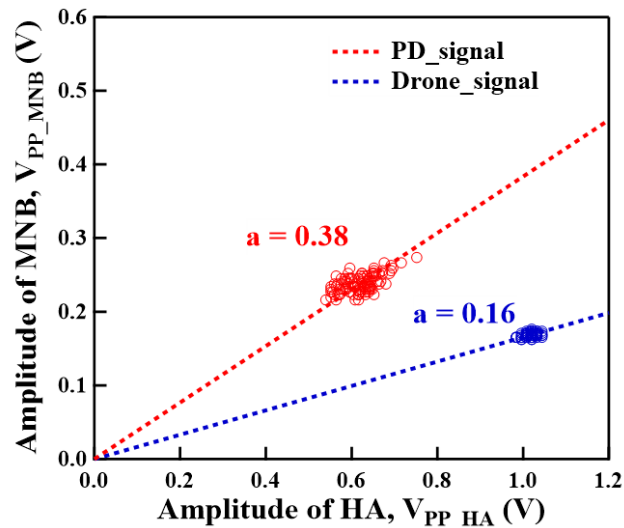
Fig. 5.10   Relation of the V_{PP} PD signal and the drone noise
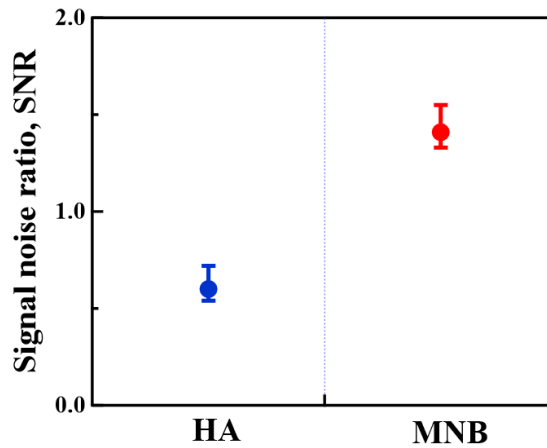
Fig. 5.11   The signal-noise ratio of PD signal and drone noise

Consequently, the advantage of noise resistance ability of the MNB antenna was investigated by comparing the measured waveforms with changing the trigger antenna for PD signal under drone noise. Figs. 5.12 (a) and (b) show examples of the measured waveforms when the HA and the MNB antenna were used as the trigger antenna, respectively. In this case, the trigger level was selected as high as possible for detecting PD-emitted EM waves. When the HA was used as the trigger antenna, the drone noise was usually detected as shown in Fig. 5.12 (a), while the MNB antenna was used as the trigger antenna, the PD signal was usually detected as in Fig. 5.12 (b). The application of the MNB antenna instead of the HA can contribute to detecting the PD signal under the drone noise.
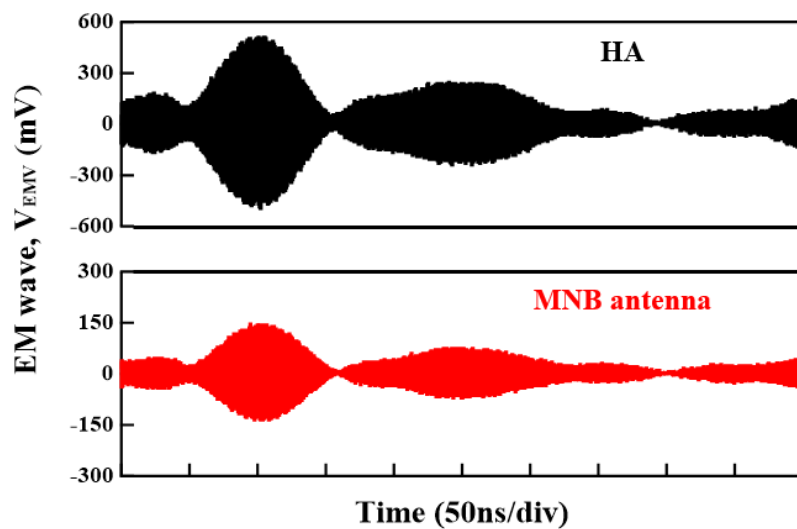
(a) Trigger antenna is HA

Fig. 5.12   Typical simultaneously measured waveforms of PD in SF_6 gas under the drone-emitted Wi-Fi noise (continued on the following page)
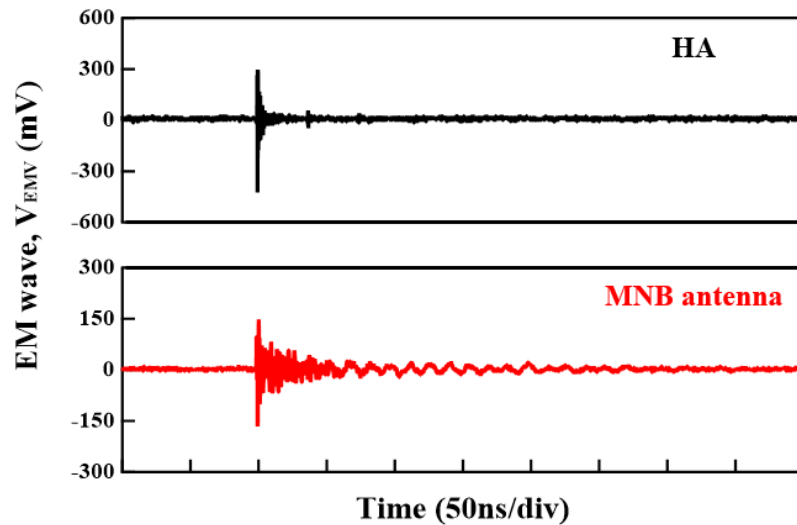
(b) Trigger antenna is MNB antenna

Fig. 5.12   Typical simultaneously measured waveforms of PD in SF_6 gas under the drone-emitted Wi-Fi noise.

5.4   Trigger antenna and level effect for PD detection under noise

According to the previous section's results, the MNB antenna can detect the PD signal under the drone noise while the HA cannot because of noise resistance ability, and the result was different from artificial noise measurement. In artificial noise measurement, the PD signal was detected superimposed with noise, and the SNR of the MNB antenna was high. However, in drone noise measurement, the antennas detected the PD signal and drone noise one by one independently, even if the PD signal and drone noise were emitted simultaneously. It is related to the repetition of EM waves and trigger level of antennas. The PD signal and drone noise are not continuous signals, and the trigger level was fixed as the highest possible level for detecting EM waves.

This section investigates the signal and noise's repetition and effect of the trigger antenna using the acquisition memory mode (fast frame mode) for PD detection under the drone noise. First, to understand the repetition rate of PD signal and drone noise depending on the trigger level, the PD signal and drone noise were measured independently when the trigger antenna and level were changed. One hundred events were detected by acquisition memory mode for each measurement, and measurement time duration was recorded to know the repetition time of events. Fig 5.13 shows the relation between repetition time and trigger level for each antenna. It was realized that when reducing the trigger level, the measurement time for 100 times events was reduced

because the high amplitude signal was repeated fewer times than the low amplitude one. In addition, if assuming the amplitudes of PD signal and drone noise are equal, the repetition time of drone noise is much shorter than PD signal. If the trigger level is low, the antennas cannot detect the PD signal due to the fast-repeating drone noise.

(a) HA   (b) MNB antenna
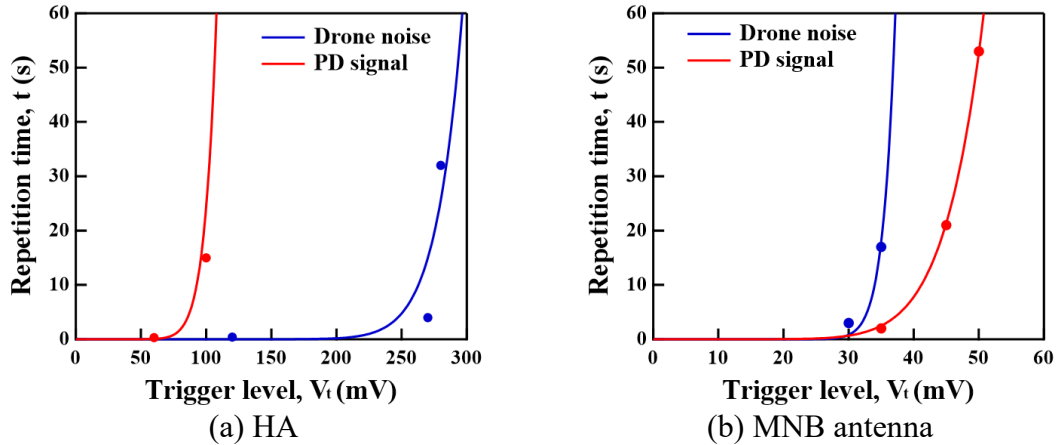
Fig. 5.13   Repetition time for 100 events of PD signal and drone noise depending on a trigger level

Consequently, the signal and noise repetition rates were calculated based on the independent measurement result and shown in Fig. 5.14. For HA, the repetition rate of drone noise is much higher than that of PD signal regardless of the trigger level. It means that the drone noise is commonly detected by HA even if the trigger level is lower than the PD signal's amplitude because of high repetition. In contrast, the MNB antenna can detect the PD signal with a high detection rate until the trigger level is lower than a critical value, T_{cr}, in which the repetition rate of the PD signal is matched with drone noise. The PD detection rate is drastically reduced if the trigger level is reduced more than T_{cr}.

(a) HA   (b) MNB antenna
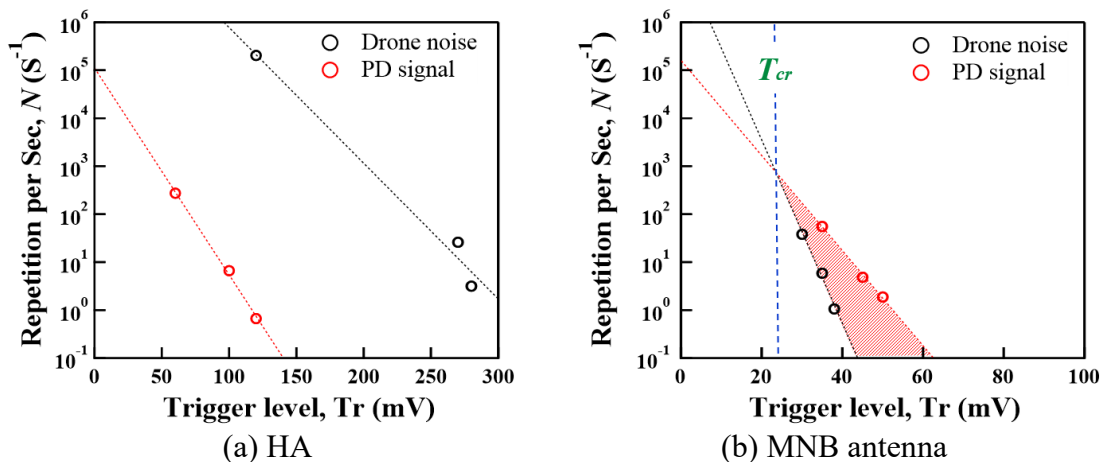
Fig. 5.14   The repetition rate of PD signal and drone noise depending on trigger level

Fig. 5.15 shows a possible assumption of the repetition of PD signal under the drone noise. The PD detection rate is discussed below when the trigger levels equal 80% of the amplitude of the drone noise for each trigger antenna as a difficulty condition.

- For HA, the amplitude of drone noise is much higher than that of PD signal, and drone noise repetition is faster than PD signal. Therefore, the antenna always catches the drone noise if the trigger level is selected as the highest possible level for detecting EM waves. If reducing the trigger level to 80% of drone noise, there is a chance to detect the superimposed PD signal and drone noise, but the PD detection rate is very low. If assuming more reduces the trigger level, the PD detection rate is more reduced due to the huge difference between repetition of signal and noise.

- For MNB antenna, the amplitude of drone noise is lower than that of PD signal. Therefore, if the trigger level is selected as the highest possible level for detecting EM waves, the MNB antenna receives the PD signal. When trigger level is selected as same as drone noise amplitude, the MNB antenna commonly receives PD signal and few times drone and superimposed PD signal and drone noise. If reducing the trigger level to 80% of drone noise, the just PD detection events are noticeably reduced and superimposed, or just drone noise events increase. If assuming more reduces the trigger level, the antennas commonly receive drone noises due to the fast repetition.

a) When HA is selected as trigger antenna

b) When MNB antenna is selected as trigger antenna
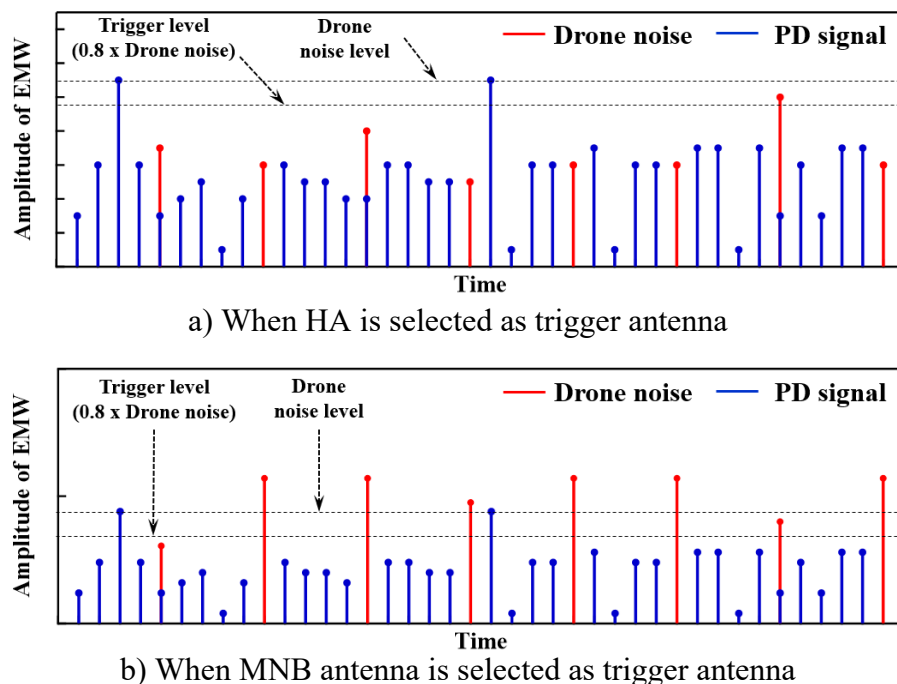
Fig. 5.15   The assumption of repetition of PD signal and drone noise

Fig. 5.16 shows the experiment result; the trigger level was fixed as 80% of the amplitude of the drone noise for each trigger antenna, and 100 triggered waveforms were recorded. Similar to the assumption, when the trigger antenna was the HA, the PD signal detection ratio, R_{PD}, was as low as 1%, and when the trigger antenna was the MNB antenna, R_{PD} was increased as high as 94%.
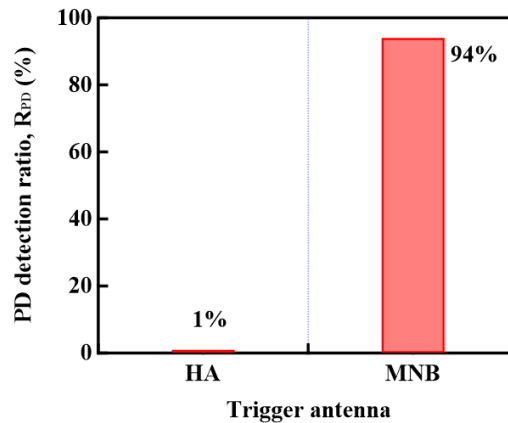
Fig. 5.16   PD signal detection ratio depending on the trigger antenna

In addition, the one PD detected events of HA was the superimposed PD signal and drone noise. When the signal and drone noise was superimposed, the amplitude is increased, and HA could catch it. The measured waveforms are shown in Fig. 5.17. In contrast, when the MNB antenna was the trigger antenna, the drone noise was detected in six events, the just PD signal was detected in 5 events, and the other 89 events were superimposed signal and drone noise. The measurement result agreed well the prediction based on repetition rate.
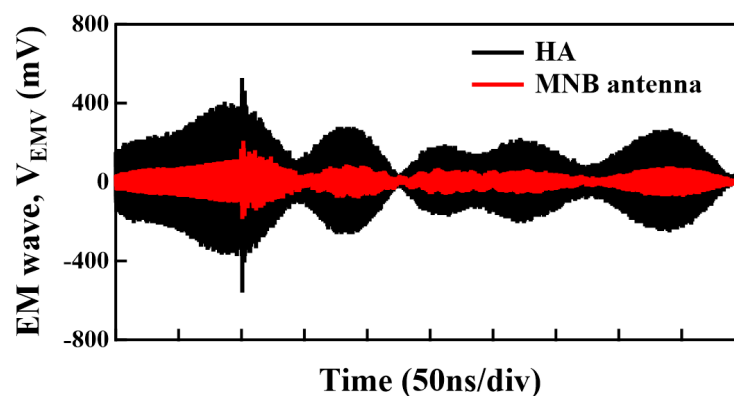
Fig. 5.17   Superimposed PD signal and Drone noise when HA was the trigger

Consequently, the three trigger levels were selected depending on the PD signal's amplitudes and drone noise. For HA, same as Fig 5.17 (a), trigger level 1 was 280 mV to be higher than the amplitude of the PD signal. The trigger levels 2 and 3 were selected 120 and 60 mV to be lower than both amplitudes of PD and drone, respectively. Fig 5.17

(b) shows the selected trigger level for the MNB antenna. Level 1 was 60 mV to be higher than the amplitude of drone noise. Levels 2 and 3 were selected 45 and 30 mV, respectively, to be lower than both amplitudes of PD and drone.

a) When HA is selected as trigger antenna

b) When MNB antenna is selected as trigger antenna
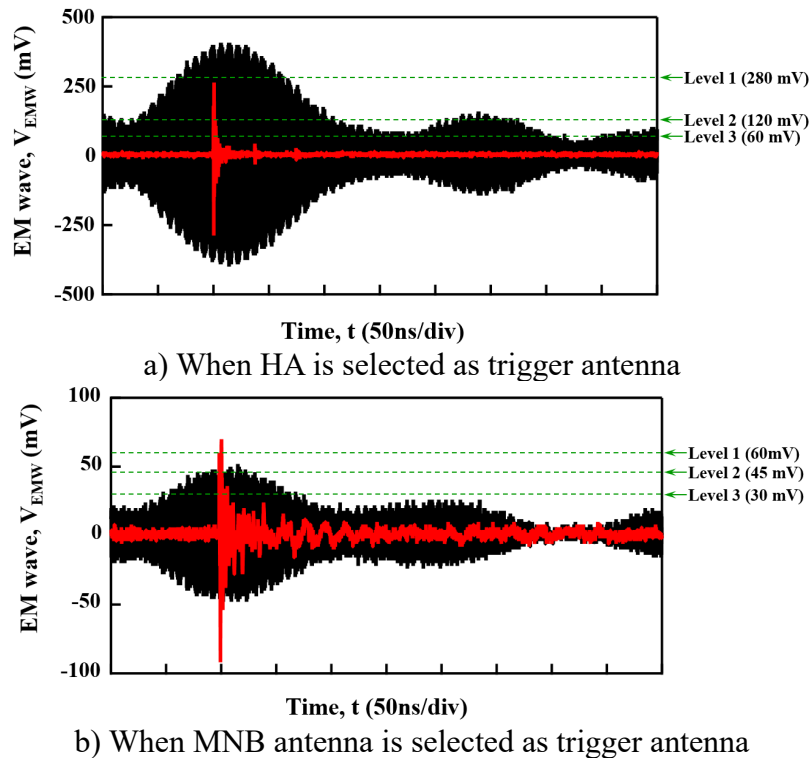
Fig. 5.18   The trigger level selection for each antenna

The measurement results are shown in Table 5.2 depends on the trigger antenna and level. When HA was the trigger, the superimposed signal was detected just one time due to the fast repetition and high amplitude of the drone noise. However, the PD detection rate was very high when the MNB antenna was selected as a trigger antenna and changed depending on the trigger level. If the trigger level is reduced, the drone noise detection increases due to the fast repetition.

Table 5.2. PD detection under the drone noise depends on the trigger antenna and level

Trigger antenna	Trigger level	PD signal	Superimposed PD and drone	Drone noise
HA	Level 1	0	1	99
	Level 2	0	0	100
	Level 3	0	0	100
MNB antenna	Level 1	0	100	0
	Level 2	6	89	5
	Level 3	2	43	55

5.5 Conclusion

The noise elimination ability of the MNB antenna was investigated based on the experiment of PD in SF_6 gas under the noise condition in this chapter. The conclusions are shown below.

1. It was clarified that the MNB antenna detected the PD in SF_6 gas under artificial noise. The signal-noise ratio of the MNB antenna was around 2, which was higher than that of the HA antenna ($SNR_{HA} \approx 1.3$) under the elimination frequency while it was around 1.2, same as SNR_{HA} under detection frequency.

2. The MNB antenna received the Wi-Fi signal with a 15 dBm lower amplitude than HA due to noise resistance ability. This noise resistance enabled the MNB antenna to detect the PD signal in SF_6 gas under drone noise ($SNR_{MNB} \approx 1.4$) while the HA could not detect ($SNR_{HA} \approx 0.6$).

3. The 100 times measurement result used the segment memory method shows that the PD detection rate under drone noise was 1% and 94% for HA and MNB antenna, respectively.

4. The PD detection rate was almost 0 for HA because PD signal repetition (R_{S_HA}) was much lower than drone noise repetition (R_{N_HA}). For the MNB antenna, the PD detection rate was changed depending on the trigger level because the ratio of PD signal and drone noise repetition was noticeably changed based on the trigger level.

5. Until the trigger level was selected as lower than the critical level, the MNB antenna could detect the PD signal under drone noise with the PD detection rate more than 50% because the PD signal repetition was higher than the drone noise repetition ($R_{S\_MNB} \geq R_{N\_MNB}$). If the trigger level was reduced more than the critical level, the PD detection rate was reduced because of $R_{S\_MNB} \leq R_{N\_MNB}$.

6. Based on these results, it can be concluded that the MNB antenna has a high noise resistance ability at the elimination frequencies and can detect the PD signal with a high signal-noise ratio under noise conditions.

References

[1] T. Bandi, M. Tanaka, H. Furuie, and S. Ohtsuka, "Developing of Multiple-narrowband Antenna to Detect Partial Discharge-emitted Signal under Radio Communication Noise Environment," *Proceeding - 8th Int. Conf. Cond. Monit. Diagnosis, C. 2020*, pp. 154–157, 2020.

[2] T. Bandi and S. Ohtsuka, "Partial Discharge Detection of Multiple-Narrow Band Antenna under the Radio Communication Noise," *IEEJ Trans. Electr. Electron. Eng.*, Vol. 16, No. 5, pp. 715–721, 2021.

[3] M. Raza, N. Aslam, H. Le-Minh, S. Hussain, Y. Cao, and N. M. Khan, "A Critical Analysis of Research Potential, Challenges, and Future Directives in Industrial Wireless Sensor Networks," *IEEE Commun. Surv. Tutorials*, Vol. 20, No. 1, pp. 39–95, 2018.

[4] M. Iglesias-Urkia, D. Casado-Mansilla, S. Mayer, J. Bilbao, and A. Urbieta, "Integrating Electrical Substations Within the IoT Using IEC 61850, CoAP, and CBOR," *IEEE Internet Things J.*, Vol. 6, No. 5, pp. 7437–7449, 2019.

Chapter 6

Enhanced Filtered Multiple Narrow Band Antenna

6.1   Introduction

Previous chapters introduced the MNB antenna as the wideband UHF sensor with high noise resistance. The experiment results demonstrated that the MNB antennas have excellent performance for PD detection under noise conditions due to noise resistance ability. However, noise resistance does not mean that the antenna does not detect noise because the antenna receives the noise, but much lower than original wideband antennas. Also, the PD detection rate of the MNB antenna was reduced when the trigger level was reduced due to the fast repetition of drone noise. The big difference between PD signal and noise gives a high PD detection rate.

If assuming that the drone is flying near the antenna, the PD signal could be masked by drone noise even if the antenna has noise resistance because of the strong intensity and repetition of noise. Therefore, a stronger noise resistance than the original MNB antenna is required for high noise conditions. In this point of view, the enhanced Filtered Multiple Narrow Band (FMNB) antenna consisting of the MNB antenna with a microstrip filter is developed to increase the noise resistance ability. The microstrip filter can be developed as any filters such as band stop, bandpass, high pass, and low pass, selectively depending on noise condition.

This chapter evaluates the designing process of an FMNB antenna with a microstrip filter to reduce Wi-Fi noise effectively. In addition, the antenna performance is experientially investigated by PD detection under Wi-Fi noise and compared with a standard Horn Antenna (HA) and the MNB antenna, fabricated same physical dimension with FMNB antenna to check the microstrip filter effect.

6.2   Design of enhanced FMNB antenna

6.2.1 Enhancement and improvement of MNB antenna

This section introduces the improvement and enhancement of the MNB antenna. There are two designing steps to upgrade the MNB antenna performance; (i) Improvement of structure and (ii) Enhancement of noise resistance ability.

Structure improvement of MNB antenna – The antenna designed in previous chapters was a general structure of MNB antenna. Based on the experiment and simulation result of the general structure of MNB antenna, the following structure improvements were implemented for MNB antenna to increase detection frequency and reduce mutual inductions and antenna size.

- Strip length: For increasing the detection bandwidth of the antenna.
- Strip order: For reducing the mutual inductance.
- Ground size: For reducing the antenna size.

Strip length and order. As discussed in Chapter 3, the printed strip monopole antenna has the feature to receive the high-order oscillation of a resonant frequency. Based on this characteristic, it is possible to use four strips to make the MNB antenna with five resonant frequencies. The FMNB antenna introduced in this chapter was designed with different frequency bands from the MNB antenna discussed in previous chapters to check the versatility of MNB types antenna.

The detection and elimination frequency bands of the FMNB antenna were shown with corresponding strip lengths in Table 6.1. The strip length was calculated by equation (3.1) with a slight adjustment.

Table 6.1. Frequency selection for the FMNB antenna

Strip length, L_S (mm)	L_1=96	L_2=50	L_3=39	L_4=32	$L_1 \approx 96/3$
Detection frequencies, f_d (GHz)	0.6	1.0	1.2	1.4	1.8
Elimination frequencies, f_e (GHz)	0.8	1.1	1.3	2.4	

In addition, the strip order was changed to reduce the mutual inductance between strips. The following equation calculated the mutual inductance between strips:

$$L \approx \frac{\mu_0}{2\pi}\left[\ln\left(\frac{2l}{\sqrt{wd}}\right) - 1\right] \qquad (6.1)$$

where, μ_0 – magnetic permeability in free space, l – corresponding length of strips, w – strip width, d – the distance between strips. The following strip order gave the lowest mutual inductance between strips; L4, L2, L1, and L3, according to the calculation.

Ground length. The ground plate is used as an image part for the printed monopole antenna. For the MNB antenna, the ground length was selected as longer than the longest strip (L_G =100 mm) because the longer strip gave the highest performance. However, the excessive ground length reduces the antenna performance. As a result, the first resonant

frequency has low reflection loss, but the reflection loss is higher than the minimum possible value for other resonant frequencies. It means the L_G=100 mm increased the detection ability of L_1 but reduced the detection ability of L_2, L_3, and L_4. From this point of view, the ground length was optimized as L_G =50 mm for the FMNB antenna, which provides enough detection ability for each frequency band and reduces the antenna size. Fig. 6.1 (a) shows the MNB antenna design after improvements.

Enhancement of noise resistance ability (using the microstrip filter) - The noise resistance ability of the MNB antenna is an important feature, distinguishing it from other wideband sensors. Therefore, an enhancement method was investigated to increase the noise resistance ability of MNB antenna for especial strong noise conditions such as noise sources coming near the antenna such as drones, cell phones, and inspection robots. As a result, the enhanced FMNB antenna has been developed by integrating the MNB antenna and a microstrip filter in a PCB without size extension.

The filter is widely used in RF-microwave applications to separate or combine the RF-microwave signals within assigned spectral limits. In the UHF method, the software and hardware filters are used for PD signal processing for noise elimination and an investigation of PD location [1-3]. Depending on the requirements and specifications, filters can be designed as lumped or distributed element circuits. The filters based on distributed element circuits are generally realized in various transmission-line structures, such as waveguide, coaxial line, coplanar waveguide (CPW), slot-line, and microstrip [4], and are suitable for printed antennas because of complex and non-size extension. The slot and microstrip filters are used to the printed antenna for noise reduction using feeding transmission lines without affecting antenna performance [5-6].

As mentioned in Chapter 3, there are three types of feeding methods commonly used in printed antennas; (i) coaxial feeding, (ii) coplanar feeding, and (iii) microstrip feed, as shown in Fig. 6.1. The coaxial feed method, shown in Fig. 6.1 (a), is the most used feed method for printed antennas such as patch antennas [7]. The coaxial cable's outer shield and center conductor pass through the dielectric substrate and connect to the antenna's ground and radiation parts. This feeding method was used for the MNB antenna design because of its simple, one-side structure and suitable installation in HV equipment.

The coplanar waveguide (CPW) and microstrip feeding methods are shown in Fig. 6.1 (b) and (c). In these methods, the radiation part is connected to the coaxial transmission line's center conductor through a 50 Ω microstrip line [8-9]. The difference

is that the CPW feed method is printed on one side of the PCB, while the microstrip feed method is designed on two sides. The advantages of these methods are a low radiation loss, uniplanar structure, flexible feed position, and high compatibility with active and passive devices. In addition, the microstrip filter can be designed using the 50 Ω microstrip feeding line in one PCB with the antenna. Therefore, the microstrip feed method is used for FMNB antenna design [10].

| (a) Coaxial feed | (b) Coplanar feed | (c) Microstrip feed |
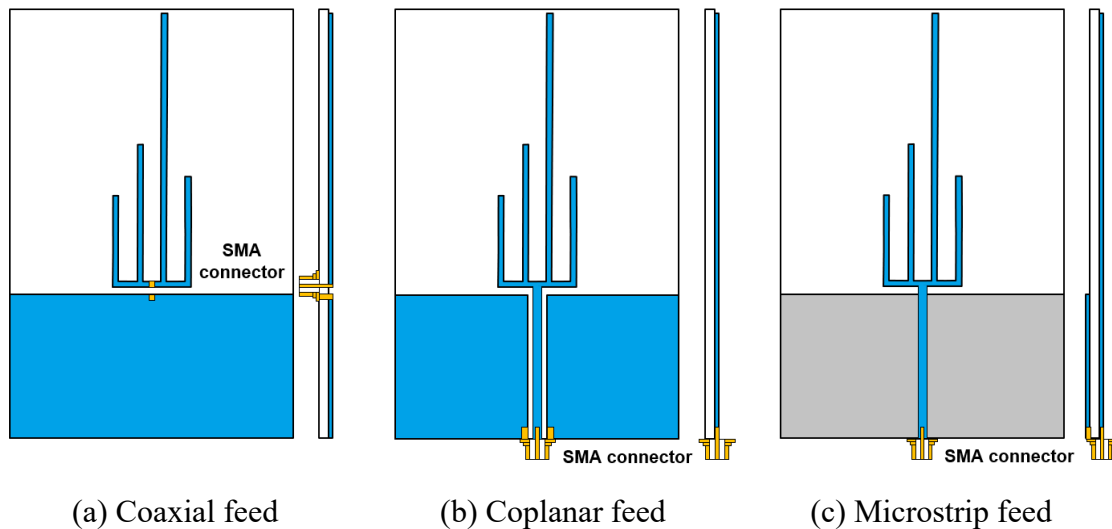
Fig. 6.1 Feeding methods for the printed monopole antennas

Once the microstrip feeding method allows developing the MNB antenna with microstrip filter, the microstrip filter is designed for FMNB antenna as the following type.

- Type of filter - The important advantage of FMNB antenna is the possibility of being designed with all type filters such as low pass, high pass, bandpass, and bandstop depending on the target frequencies. In this study, the FMNB antenna is suggested with a low pass filter with a 2 GHz cut of frequency (f_C=2GHz) for high resistance of Wi-Fi, 2.4 GHz noise.

- Filter prototype of low pass filter - There are two commonly used filter prototypes, Chebyshev and Butterworth, and their frequency response are shown in Fig. 6.2. The Butterworth types filter has a maximally flat response, but the transition region is wide and not steep. In contrast, the Chebyshev type has steep and narrow transition regions, but a passband ripple response is higher than the Butterworth type. Due to steep transition, the Chebyshev types filter was selected, and passband ripple was selected as low as possible, 0.1 dB for FMNB antenna design.
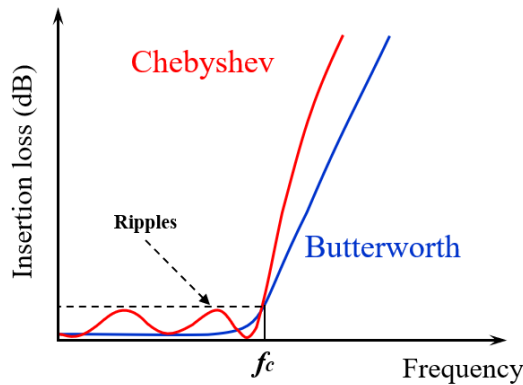
Fig. 6.2 Comparison of the frequency response of different prototype filters

- Structure of microstrip filter - Depending on the making method, many different conventional microstrip LPFs are widely used in many RF and microwave applications, such as stepped-impedance filter, open-stub filter, and semi-lumped elements filter [4]. For the FMNB antenna, the stepped-impedance L-C ladder-type was used because of simple adjustment and configuration.

Fig. 6.3 shows a general structure of stepped-impedance microstrip LPF, with a fifth-order cascaded shunt structure of alternating high-and-low impedance transmission lines. Even if the high order cascaded structure increases filtering response, the fifth-order cascaded shunt structure was selected due to size limitation.
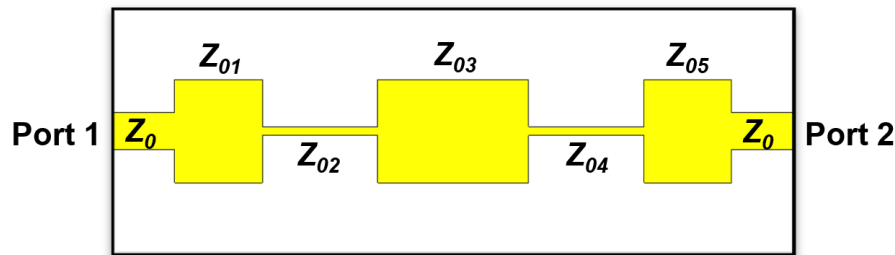
(a) layout structure in the PCB
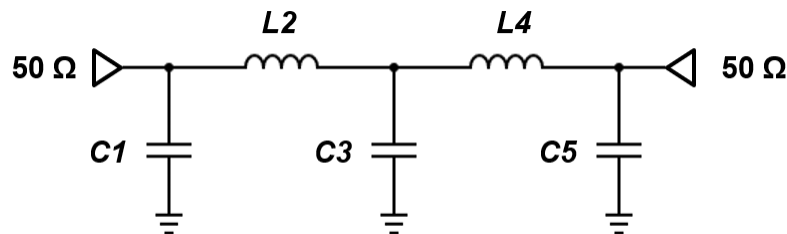
(b) equivalent circuit

Fig. 6.3 Design of the stepped-impedance microstrip low-pass filter (5th order cascading with shunt structure)

The high-impedance lines act as series inductors, and the low-impedance lines act as shunt capacitors, like the equivalent circuit shown in Fig. 6.3 (b). Because expressions for inductance and capacitance depend upon both the characteristic impedance and length, the impedance of microstrip lines should be following order $Z_{0C} < Z_0 < Z_{0L}$, where Z_{0C} and Z_{0L} represent the characteristic impedances of low and high impedance lines, respectively, and Z_0 is the connection impedance, which is usually 50 Ω for microstrip filters.

To select the high and low impedances, it should be considered (i) the lower impedance is better for Z_{0C}, but the line width W_C must not affect the operation frequency and (ii) the higher impedance is better for Z_{0L}, but the impedance must not so high that its fabrication becomes difficult as a narrow line or that its current-carrying capability becomes a limitation. According to the above considerations, the characteristic impedance of the high- and low-impedance lines was chosen as Z_{0L} = 100 Ω, Z_0 = 50 Ω, and Z_{0C} = 25 Ω.

The main purpose of the microstrip filter for this research is to reduce the Wi-Fi noise; thus, the cut-off frequency was selected as 2 GHz and passband ripple 0.1 (or reflection loss <-16.45 dB). The design parameters of the proposed microstrip LPF were calculated following formulas.

- Inductance and capacitance values

$$L_n = \left(\frac{Z_0}{g_0}\right)\left(\frac{\Omega_c}{2\pi f_c}\right) g_n \tag{6.2}$$

$$C_n = \left(\frac{g_0}{Z_0}\right)\left(\frac{\Omega_c}{2\pi f_c}\right) g_n \tag{6.3}$$

- The physical width of lines

$$W = \frac{7.48 \times h}{e^{\left(\frac{Z_0\sqrt{\varepsilon_r+1.41}}{87}\right)}} - 1.25 \times t \tag{6.4}$$

- Effective dielectric constant

$$\varepsilon_{eff} = \frac{\varepsilon_r + 1}{2} + \frac{\varepsilon_r - 1}{2}\left(1 + 12\frac{h}{W}\right)^{-0.5} \tag{6.5}$$

- The guided wavelength of the microstrip

$$\lambda_g = \frac{\lambda_0}{\sqrt{\varepsilon_{eff}}} \tag{6.6}$$

- The physical length of high and low impedance lines

$$l_L = \frac{\lambda_{gL}}{2\pi} sin^{-1} \left(\frac{\omega_c L_n}{Z_{0L}} \right) \tag{6.7}$$

$$l_C = \frac{\lambda_{gC}}{2\pi} sin^{-1} (\omega_c C_n Z_{0c}) \tag{6.8}$$

where, Ω_C – normalized cut off frequency (1.0 GHz), n – order number, g_n – element values for an order number, f_C – cut off frequency (2.0 GHz), Z_0 - impedance of the line, h – the dielectric thickness (1.6 mm), t – trace thickness (0.001 mm), ε_r – relative dielectric constant (4.5), λ_0 – free-space wavelength. The calculated parameters of the proposed microstrip LPF are shown in Table 6.2.

Table 6.2. The design parameter of the purposed microstrip LPF

Element	Characteristic impedance (Ω)	Element transformation	Width (mm)	Length (mm)
Z_0	50	50 Ω	3.0	3.0
Z_{01}; Z_{05}	25	0.98 pF	8.4	7.2
Z_{02}; Z_{04}	100	6.43 nH	0.7	9.4
Z_{03}	25	3.18 pF	8.4	12.4

Fig. 6.4 shows the S21 and S11 parameters purposed fifth-order Chebyshev stepped-impedance microstrip LPF simulated using the parameters from Table 6.2 and compared with fifth-order Butterworth LPF. As a previous discussion, the S parameters of purposed Chebyshev types filter is steeper than Butterworth type; the S21's slope at cut-off frequency was -19.28 dB/GHz and -13.57 dB/GHz, and the S11's slope was 23.7 dB/GHz and 7.9 dB/GHz, for Chebyshev and Butterworth type, respectively. The cut-off frequency agreed well designed one; at the 2.0 GHz, the S21 transfer function, i.e., insertion loss, was -3.22 dB. Therefore, this filter design can be used for FMNB antenna.
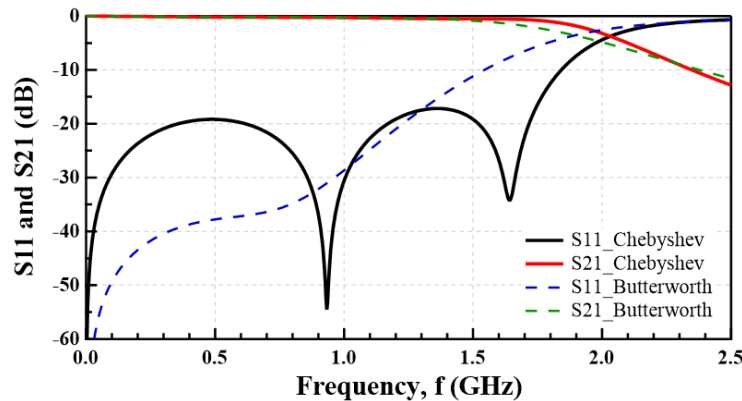
Fig. 6.4 Simulated S11 and S21 parameters of the fifth-order Chebyshev and Butterworth filters

6.2.2 Simulation of FMNB antenna

After the above enhancement and improvements, the improved MNB and enhanced FMNB antennas were simulated by COMSOL software. The simulation setup and function were decided in detail in Chapter 2. Fig. 6.5 (a) and (b) show the antenna design of MNB and FMNB antenna, respectively. The full size of the antennas is 100x150x1.6 mm and lower than the MNB antenna, designed and used in previous chapters.

(a) without microstrip filter (MNB)   (b) with microstrip filter (FMNB)
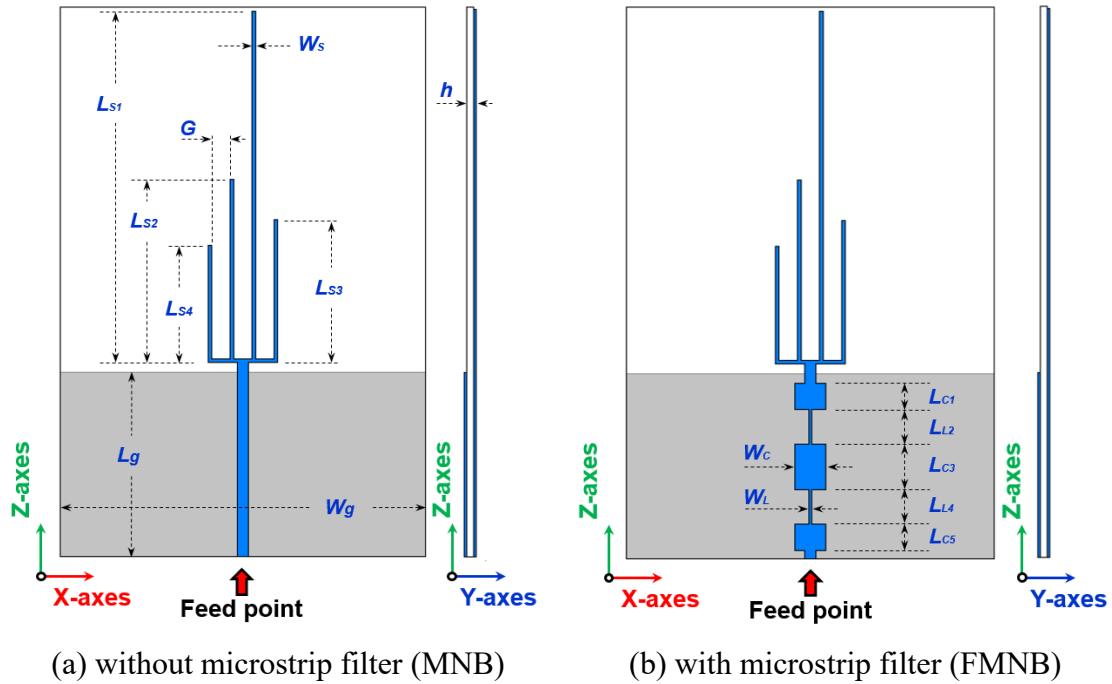
Fig. 6.5 Design of FMNB antenna

The simulated reflection loss of the FMNB antenna is shown in Fig. 6.6 compared with the MNB antenna. The detection and elimination frequencies generally agreed well with the designed one. The detection bandwidth is shown in Table 6.3 for each resonant frequency. There are two differences related to the microstrip filter at a frequency higher than 1.7 GHz.

1. The fifth resonant frequency was slightly shifted to the high frequency because of the ripple effect of the Chebyshev filter. However, it cannot affect the detection and elimination bandwidth because the reflection loss was around -18 dB, which belonged detection zone of the antenna.

2. The reflection loss of FMNB antenna drastically increased up to -4.6 dB at 2 GHz, cut-off frequency. It means the FMNB antenna has high resistance for high-frequency noises. Especially, the reflection loss was increased from -3.26 dB to -0.28 dB at the Wi-Fi frequency band (2.4 GHz). It means the FMNB antenna receives the 2.4 GHz

signal with a high reduction around 95%.

According to the above results, it can be concluded that the FMNB antenna gave sufficient reduction at the Wi-Fi frequency band.
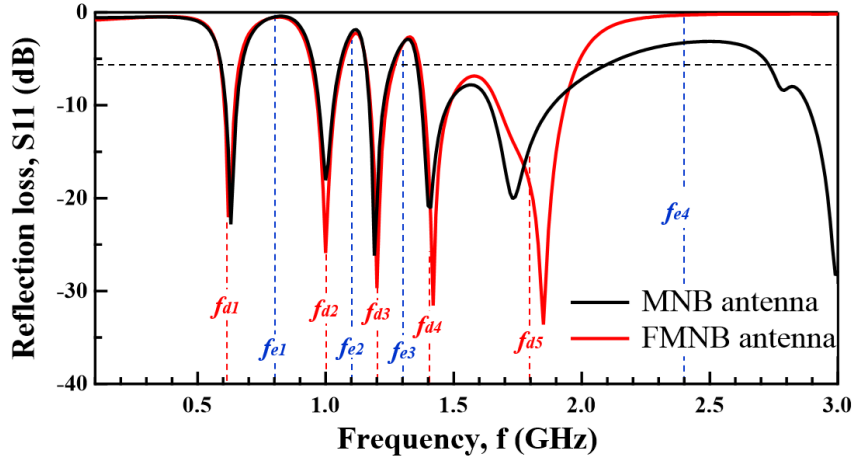
Fig. 6.6 Simulated reflection loss of FMNB antenna compared with MNB antenna

Table 6.3. The detection frequency bandwidth of MNB and FMNB antennas

Order number		1st	2nd	3rd	4th	5th	Total
MNB antenna	Resonant frequency (GHz)	0.62	1.0	1.2	1.42	1.85	-
	Bandwidth (GHz)	0.08	0.1	0.1	0.7		0.98
FMNB antenna	Resonant frequency (GHz)	0.63	1.0	1.19	1.41	1.73	-
	Bandwidth (GHz)	0.08	0.1	0.1	0.62		0.9

The detection frequencies were confirmed by the simulated electric field distribution at the resonant frequencies of the FMNB antenna in Fig. 6.7 (a) to (e). The electric field accumulated the corresponding strip's edge at each detection frequency. The fifth detection frequency comes from the third-order oscillation of the first detection frequency; thus, the first strip activated around strip edge as well as two-third of the strip at Fig. 6.7 (e). To clearly see the microstrip LPF effect, the electric field distribution of the FMNB antenna at 2.4 GHz is shown in Fig. 6.8 compared with that of the MNB antenna. Due to their coupling capacitance, the MNB antenna was slightly activated around the connection line and ground edge. While, the FMNB antenna, the microstrip filter blocked the 2.4 GHz resonation.

(a) at 0.62 GHz (f_{d1})   (b) at 0.10 GHz (f_{d2})   (c) at 1.2 GHz (f_{d3})

(d) at 1.42 GHz (f_{d4})   (e) at 1.85 GHz (f_{d5})
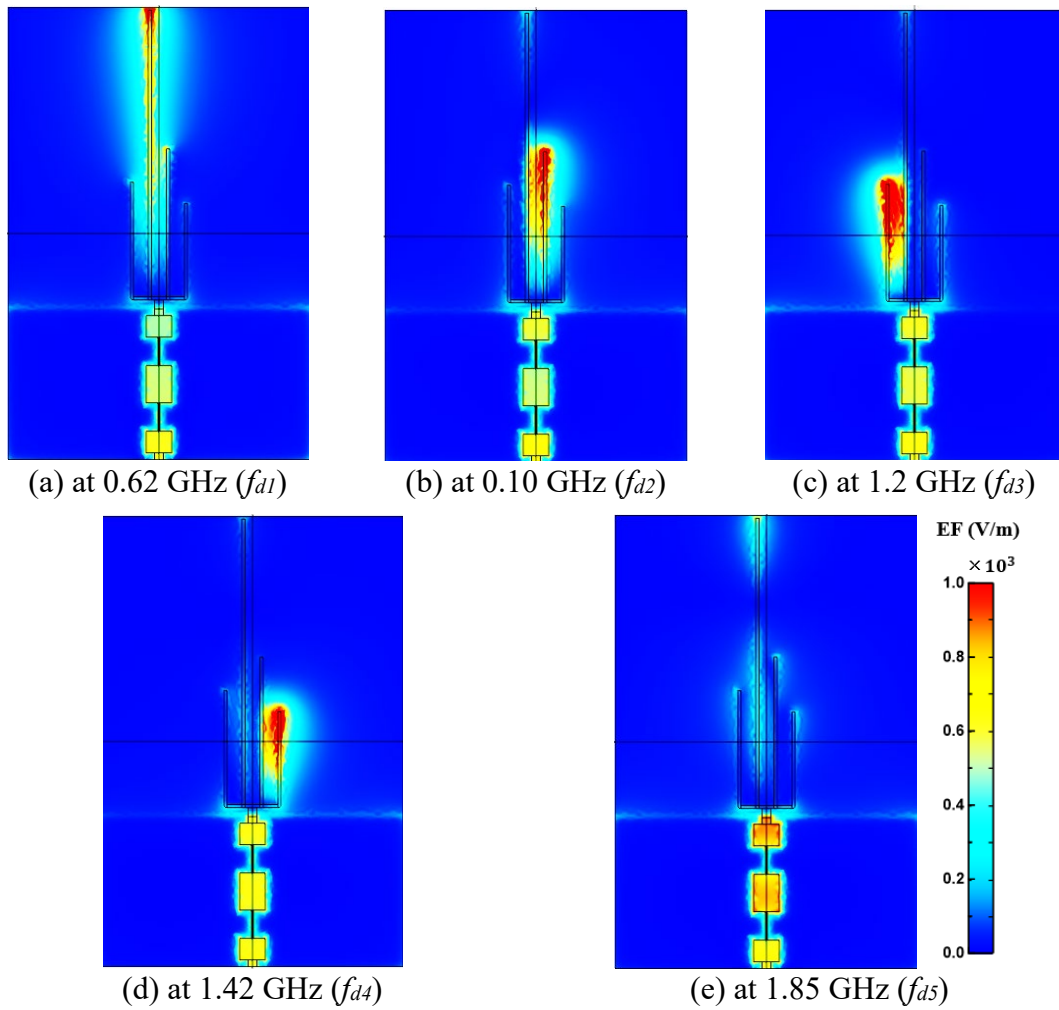
Fig. 6.7 Electric field distribution of FMNB antenna at detection frequencies of it

(a) MNB antenna   (b) FMNB antenna
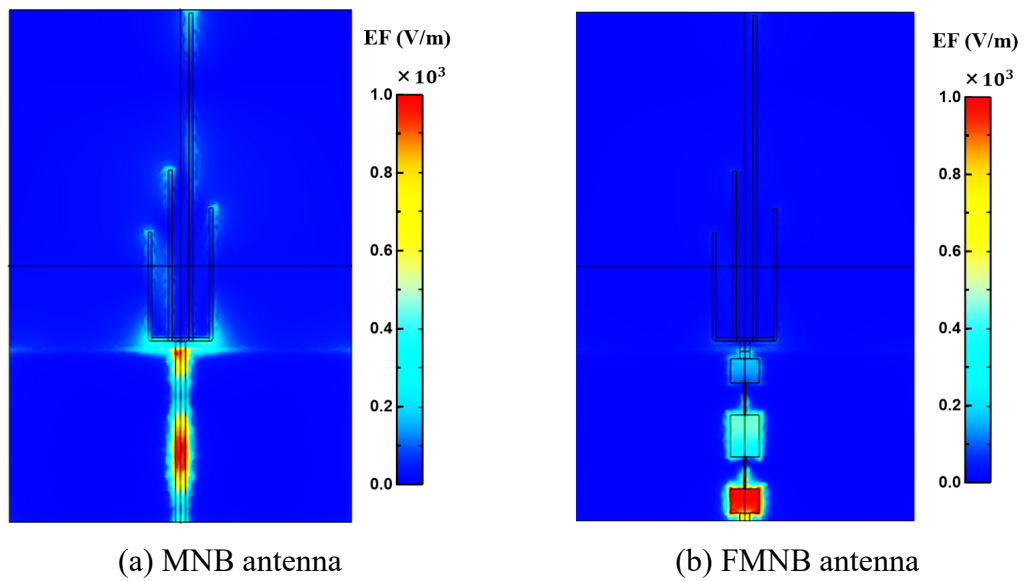
Fig. 6.8 Electric field distribution of FMNB antenna at Wi-Fi frequency compared with MNB antenna

In addition, the directivity of the FMNB antenna is shown in Fig. 6.9 as a 2D radiation pattern. The simulation results demonstrated that the FMNB antenna has good omnidirectional characteristics, the same as the MNB antenna.
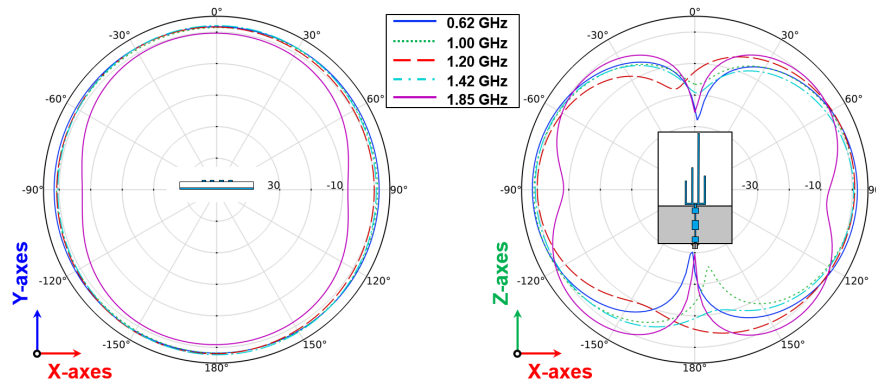
Fig. 6.9 The radiation pattern of the FMNB antenna

Once the simulation result gave the applicable performance, the FMNB and MNB antennas were fabricated using the etching method to reduce the fabrication errors. Fig. 6.10 shows the fabricated MNB and FMNB antenna compared with HA.
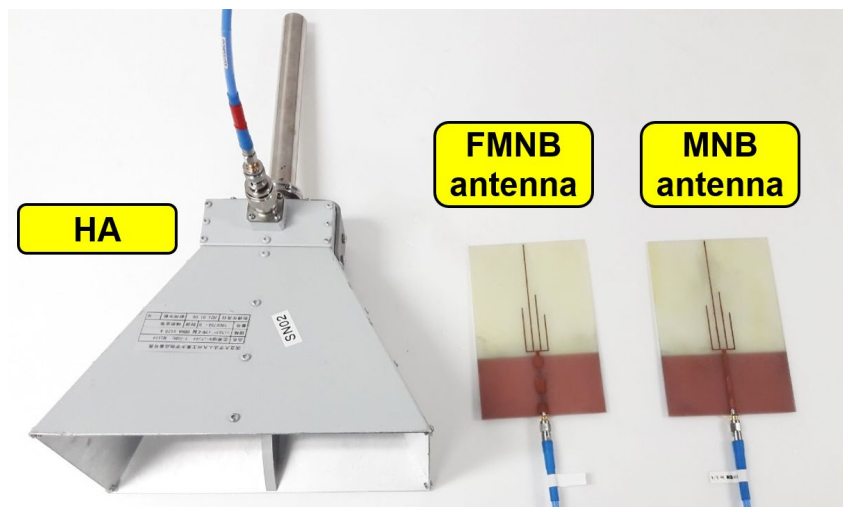
Fig. 6.10   Fabricated MNB and FMNB antenna compared with HA

6.2.3 Test of FMNB antenna

First, the reflection losses of the FMNB and MNB antennas were measured and shown in Fig. 6.11. The measurement results are compared with simulation results. For the MNB antenna, the measured and simulated results have an excellent agreement more than the antenna discussed in Chapter 3. It could be related to the improvement of structure and fabrication methods. The antenna discussed in Chapter 3 detected four resonance frequencies, and the fourth resonance frequency overlapped with the third-order oscillation of the first resonance. These overlapped resonant frequencies were the

reason for simulation and measurement's difference. However, the improved MNB antenna is fabricated with five resonant frequencies using four strips because the third-order oscillation of first resonance and fourth resonant frequencies are separated. Also, the fabrication error is reduced by using the etching method. As a result, the difference between simulation and measurement results could be reduced.
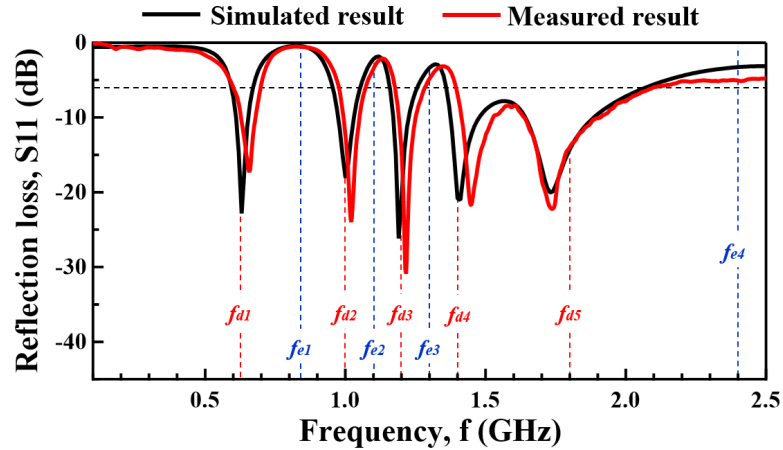
(a) MNB antenna
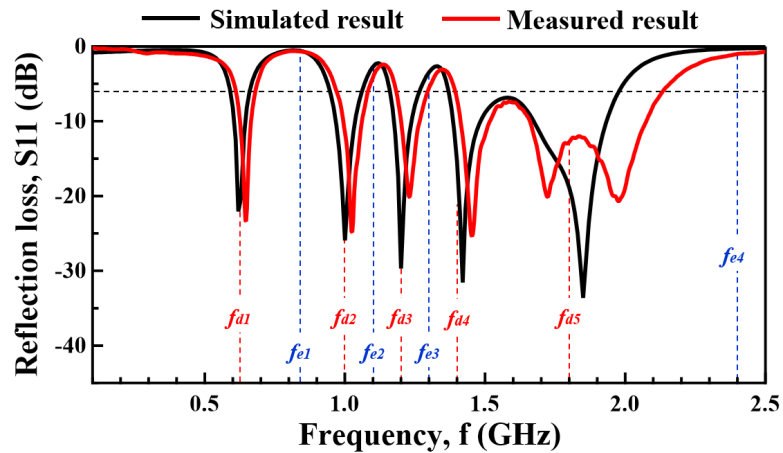
(b) FMNB antenna

Fig. 6.11　　　Measured reflection loss of FMNB and MNB antennas compared with the simulation results

For the FMNB antenna, the measurement results agree well with the simulation except that there are two dips around the fifth detection frequency for the FMNB antenna. The reason for this difference could come from the microstrip filter. As early mentioned, the Chebyshev types filter has a steep roll-off rate parallel with passband ripple. In addition, the reflection loss of the FMNB antenna is lower than -1 dB when that of the MNB antenna was -5 dB at 2.4 GHz.

After that, the transfer function of both antennas was measured to calculate the antenna factor using standard wideband HA as a reference antenna. The measurement was performed in an anechoic room, and the photo of the experimental setup is shown in Fig. 6.12. The experiment procedure and setup were decided in detail in Chapter 2.

Fig. 6.12   Experiment setup for transfer function and antenna factor

The antenna factor has a reverse relation with reflection loss. The calculated antenna factor of the FMNB antenna is shown in Fig. 6.13 compared with the reflection losses of the antenna. The antenna factor is reduced at the detection frequencies of the antenna, and there are slight differences. These could be related to the reference antenna effect and the antenna directivity because the antenna factor is related to the antenna directivity while reflection loss is not. However, the antenna factor is relatively high at the Wi-Fi frequency band, which means the FMNB antenna effectively reduced the Wi-Fi signal.
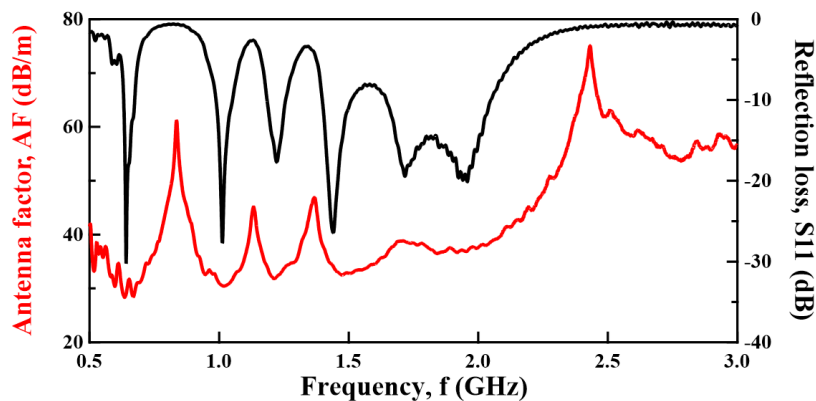
Fig. 6.13   Calculated antenna factor of FMNB antenna compared with the

reflection loss

6.3 Discharge detection ability of FMNB antenna

The FMNB antenna was successfully designed and fabricated, and the measured parameters of antennas agreed well with simulated ones. In this session, the FMNB and MNB antennas were applied to detect the BD and PD emitted signals, and the experiment setups were arranged the same as in Chapter 4.

6.3.1 Breakdown discharge detection

Both MNB and FMNB antennas could detect the BD signal and Fig. 6.14 shows the BD experiment results in a time and a frequency domain. The EM waveforms measured by the fabricated antennas are slightly wider than HA because of the low-frequency components (under 0.7 GHz). The intensity of BD signal is reduced at elimination frequencies of FMNB antenna while it was relatively high at detection frequencies except for 1.2 GHz because of the original frequency spectrum of BD signal. The FFT of HA represented the original frequency component of the BD signal, and the intensity of HA was relatively low at 1.2 GHz.
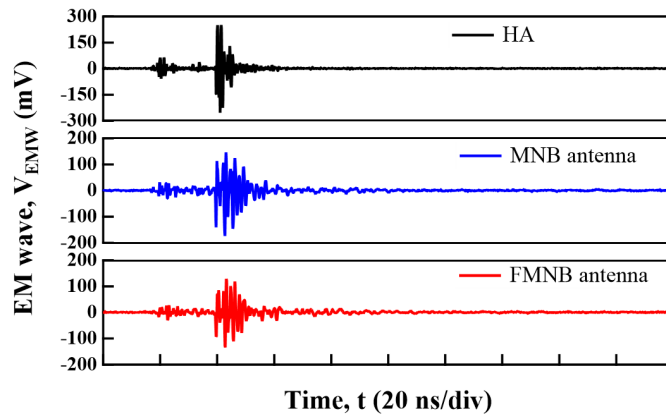
(a) Electromagnetic waveform of breakdown discharge
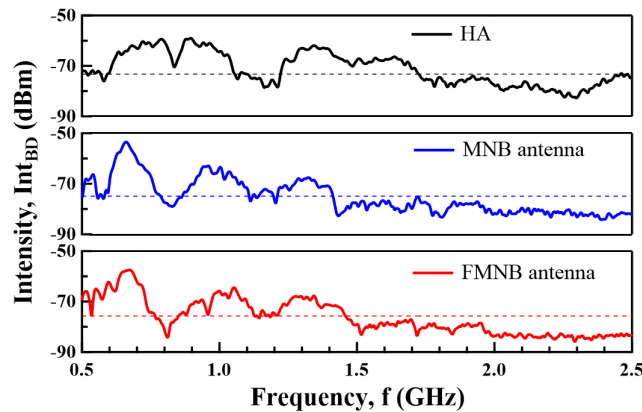
(b) Frequency spectrum of measured electromagnetic wave of BD

Fig. 6.14   The measurement result of the BD signal

The V_{PP_BD} of the MNB and FMNB antennas was compared with HA in Fig. 6.15. The slope was 0.54 and 0.44 for MNB and FMNB antenna, respectively. The difference in slope is related to the detection frequency bandwidth and filter effect. The MNB antenna has wider bandwidth than the FMNB antenna, so detection amplitude was high. However, the correlation coefficient was high enough, 0.96, for both antennas.
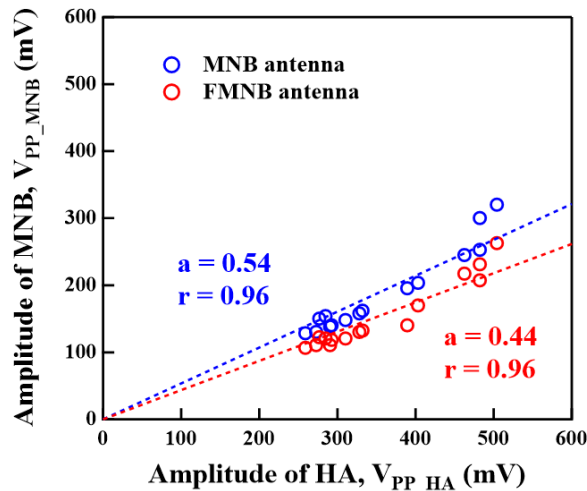
Fig. 6.15   The amplitude relation of antennas for BD experiment

6.3.2 Partial discharge in SF$_6$ gas detection

After the BD signal detection experiment, the MNB and FMNB antennas were applied to PD in SF$_6$ gas measurement in an anechoic room. The experiment setup was the same as the PD detection setup in Chapter 4, and the detail was decided in Chapter 2. Fig. 6.16 (a) and (b) show the typically measured EM waves and averaged frequency spectrum of 30 measurements. The MNB and FMNB antennas received some relatively low-frequency signals due to high intensity. These noises could come from the PD experiment setup as corona discharge and so on. Therefore, the EM waveforms measured by MNB and FMNB antennas are wider than the result of HA, but it does not affect the PD detection performance. The frequency spectrum of the PD signal agreed well with the reflection loss of the FMNB antenna.

The V_{PP_PD} of MNB and FMNB antennas was compared with HA in Fig. 6.17. The slope was 0.29 and 0.27 for MNB and FMNB antenna, respectively, and the linear relations were confirmed for the PD signal. The slope difference was the same as BD measurement; the MNB antenna had a slightly higher slope than the FMNB antenna. In addition, the correlation coefficient was reduced for the FMNB antenna due to the frequency response of the antenna.
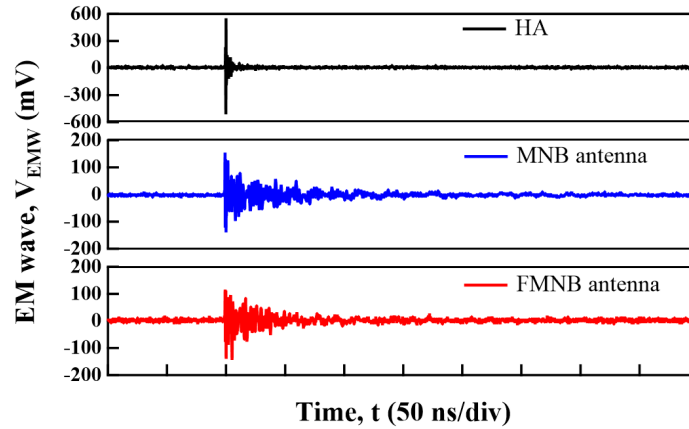
(a) Electromagnetic waveform of PD in SF$_6$ gas
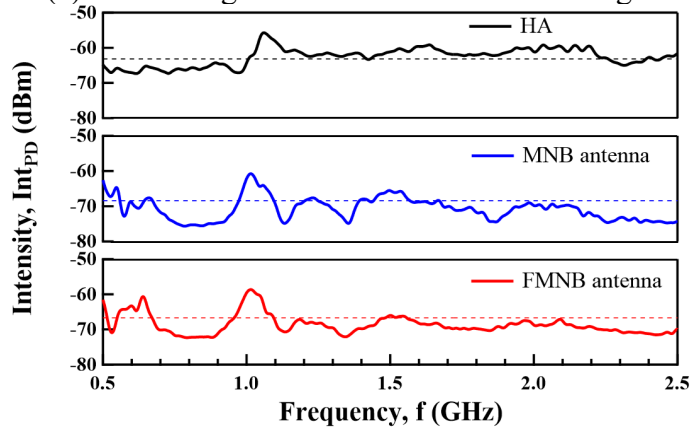
(b) Frequency spectrum of measured electromagnetic wave of PD in SF6 gas

Fig. 6.16   The measurement result of the PD signal in SF$_6$ gas
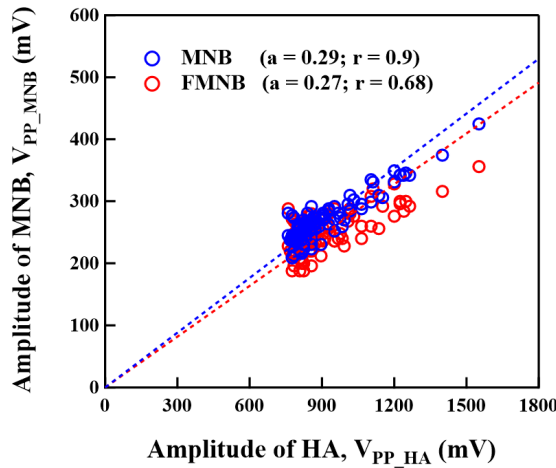
Fig. 6.17   The amplitude relation of antennas for PD experiment

6.4   Noise resistance ability of FMNB antenna

The previous session shows the PD detection ability of the FMNB antenna. In contrast, the noise reduction ability of the FMNB antenna was discussed in this session, especially for Wi-Fi noise. The Wi-Fi noise was represented by the commercial drone Phantom-4, whose operating frequency is 2.4 GHz. First, the fabricated antennas were applied to measure just drone noise with HA to compare. The typical EM waves of drone noise were simultaneously measured by three antennas when HA was selected as the trigger antenna, and frequency spectrums averaged from 30 measurements were shown in Fig. 6.18. The HA received the drone noise with a large amplitude, whereas the MNB antenna detected the drone noise 14 dB lower than HA. It seems that the FMNB antenna did not receive the drone noise because the amplitude was same as the background noise. However, it is shown in Fig. 6.18 (b) that the FMNB antenna detected the drone noise, whose intensity was noticeably lower compared with the result of HA, more than 35 dBm.
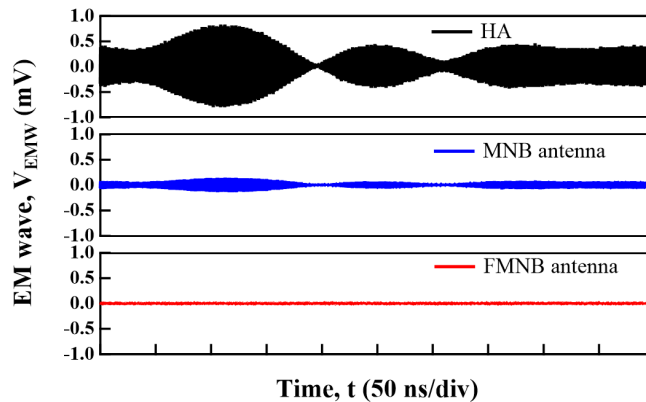
(a) Electromagnetic waveform of Drone noise
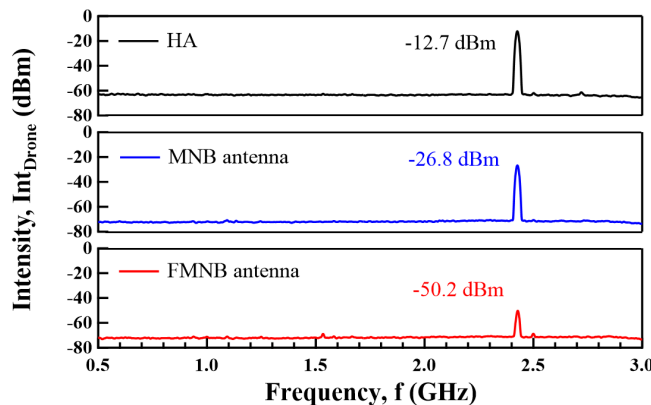
(b) Frequency spectrum of measured electromagnetic wave of drone noise

Fig. 6.18   The measurement result of drone noise

The relation between V_{PP} of the drone noise measured by the MNB and FMNB antenna versus the HA is shown in Fig. 6.19. The slope of MNB and FMNB were 0.19

and 0.03, respectively. Namely, the slope of the drone noise was 1.5 and 8 times lower than that of the PD signal for the MNB and FMNB antenna, respectively.
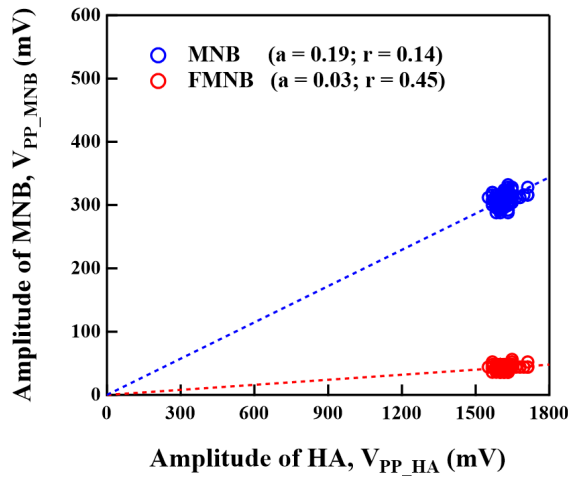
Fig. 6.19   The amplitude relation of antennas for Drone noise experiment

The comparison between V_{PP} of PD signal and drone noise for each antenna based on 100 measurement results are shown in Fig. 6.20 (a) when HA was a trigger antenna. In this condition, there is a high probability that the FMNB antenna can detect PD signal in all cases, while the MNB antenna could detect the drone noise in some cases because of the relation of V_{PP} between the PD and noise. Namely, $V_{S\_FMNB} > V_{N\_FMNB}$, $V_{S\_MNB} \approx V_{N\_MNB}$, and $V_{N\_HA} > V_{S\_HA}$ for the same event measurement.

Fig. 6.20 (b) summarized the signal-noise ratio (SNR) of antennas based on the average values of the independent measurement results. The SNR was 0.57, 0.87, and 5.84 for HA, MNB, and FMNB antennas, respectively. This result suggests that the FMNB antenna has far superior detection properties for PD detection in SF$_6$ gas than the wideband HA and MNB antennas under the drone noise.
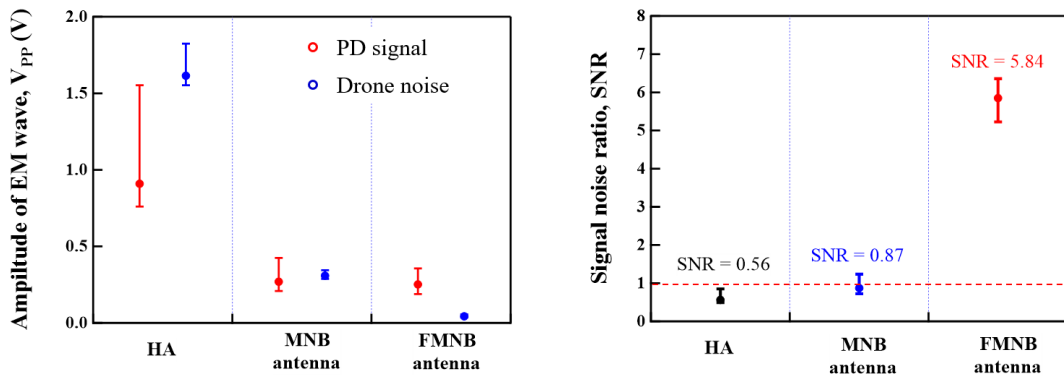
(a) Amplitudes   (b) Signal noise ratio

Fig. 6.20   Comparison of PD signal and drone noise detection based on independent measurement

6.4.1 PD detection under Wi-Fi noise

The above results are obtained based on the independent measurements. It means the signal and noise repetition did not affect the measurement. However, the generation repetition of PD signal and drone noise are also important to detect PD under the noise except the amplitude. According to Chapter 5, there are two cases where PD signal can be detected under the noise. One is that the amplitude of the PD signal is higher than that of drone noise. Another one is detecting PD signals when drone noise is not generated or generated at a relatively lower level, even if the drone is working. However, detecting the PD signal as the second case is difficult because drone noise's amplitude and generation repetition are extremely higher than that of the PD signal.

In this session, the antennas were applied to measure the PD signal under the drone noise using the fast frame mode, i.e., a segmented memory acquisition mode, to catch 100 events. Fig. 6.21 shows the photo of the measurement setup, and the distance between PD and antenna and drone and antennas was 1 and 4 meters, respectively.
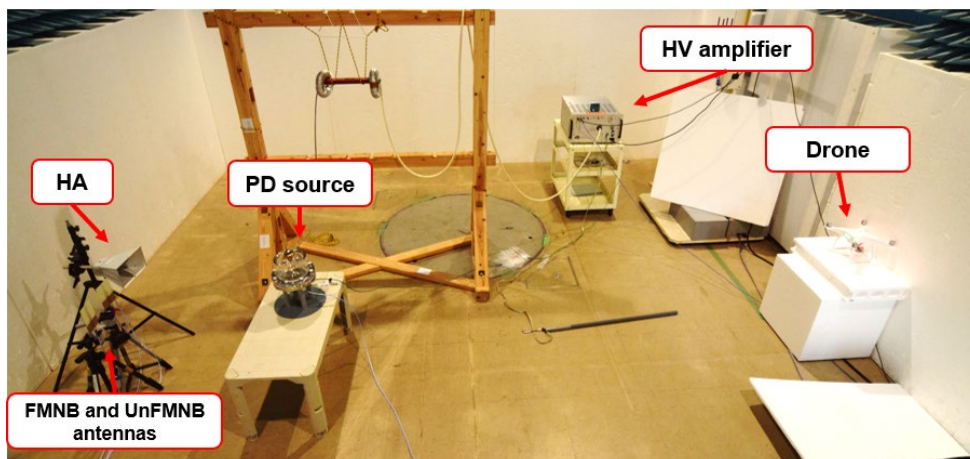
Fig. 6.21 Experiment setup of PD measurement under the drone noise

First, the PD current was used as a trigger signal to check the repetition of the PD signal and drone noise. For 100 measurements, six events were detected, just PD signals without drone noise, and the rest 94 events were PD signals superimposed on the drone noise. It indicates that the generation repetition of drone noise is much higher than the PD signal. Figs. 6.22 (a) and (b) showed typical waveforms measured simultaneously with the HA, MNB, and FMNB antennas where PD occurred along with drone noise, and the frequency response obtained as average from 100 waveforms FFT analysis.

Fig. 6.22 (a) indicates that the FMNB antenna has noticeable higher SNR than the MNB and HA, and the PD signal can be clearly recognized by eliminating the drone noise

for the FMNB antenna. The MNB and HA could detect the PD signal, but their SNR was around 1.5 and lower than 1, respectively. From Fig. 6.22 (b), it was found that the MNB and FMNB antennas received the drone noise reduced around 14 and 33.6 dBm.
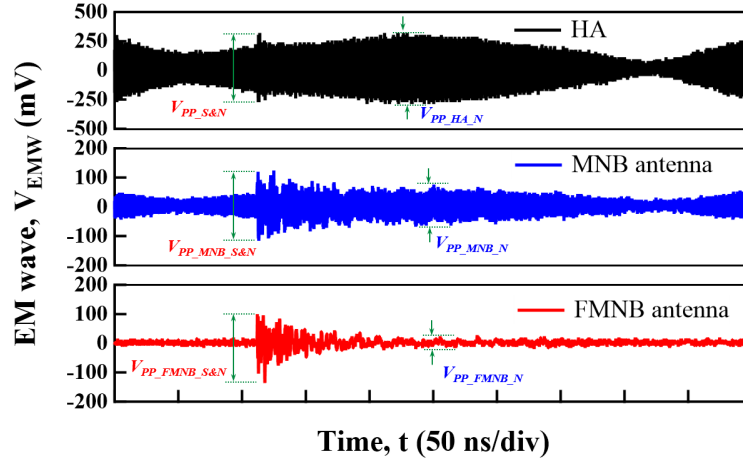
(a) Electromagnetic waveform of a superimposed PD and drone noise
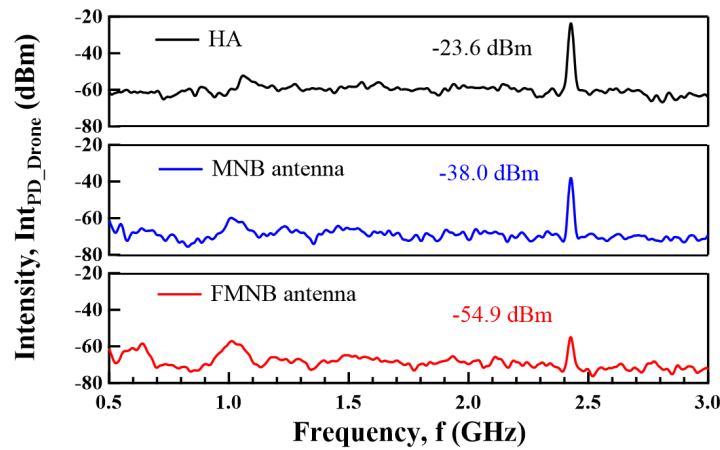
(b) Frequency spectrum of a superimposed PD and drone noise

Fig. 6.22   The measurement result of PD signal under drone noise when the PD current was used as the trigger signal

The amplitude relation of only PD signal, only drone noise, and superimposed PD signal on drone noise between the HA and the FMNB antennas are shown in Fig. 6.23. The relation of the only PD signal (black line) between the antennas showed the linear correlation with a relatively higher slope (0.41) compared to those of the only drone noise (blue dashed line) as well as the only PD signal (0.27) shown in Fig. 6.19. The much lower coefficient of the drone noise was caused by the high noise resistance ability of the FMNB antenna. Namely, the V_{PP} of the FMNB antenna for the drone noise is almost constant that is equal or lower than BGN, irrespective of the drone noise amplitude. i.e., fundamentally no relation between the antennas.
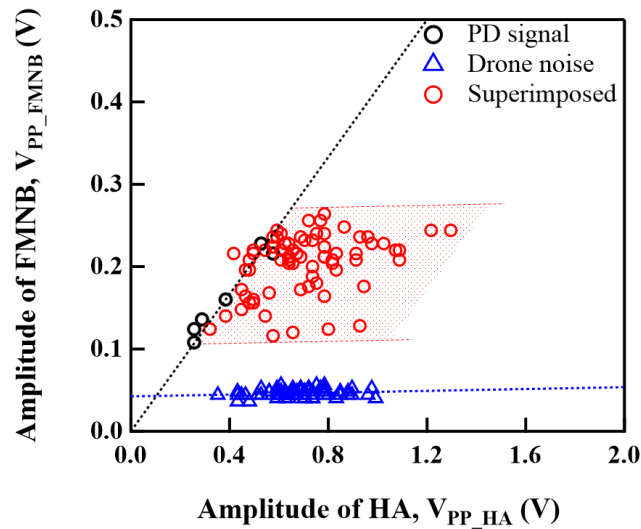
Fig. 6.23   Relation between V_{PP} of PD signal, drone noise, and superposed PD signal measured by HA and FMNB antennas

The difference in the slope for the only PD signals between Fig. 6.23 and Fig. 6.17 resulted from the waveform, i.e., frequency components, of the measured PD-emitted EM waves by the different triggers. The higher coefficient of the slope in Fig. 6.23 was attributed to the PD current trigger that could detect the waveform with much wider frequency components because of no limitation compared with the HA trigger. The relation of a superimposed PD signal on the drone noise between the antennas (red circle) showed scattering, but the distribution of V_{PP} of the FMNB and the HA antennas agreed well with that of the only PD signal and the only drone noise, respectively. This is because the FMNB antenna just detects the PD signal by eliminating the drone noise, and the HA detects the superimposed PD signal on the drone noise. Thus, this result also supports the superiority of the FMNB antenna to detect PD signal under the drone noise to the conventional wideband antenna.

6.4.2 Trigger antenna difference

As mentioned previously, there are two chances where a PD signal can be detected under the noise. The first one is that the amplitude of the PD signal is higher than that of drone noise. Another is detecting PD signals when drone noise is not generated or generated at a relatively lower level. To check the first case, the PD detection ability under the drone noise was summarized in the 100 events measurement by changing the trigger antennas when the trigger level was fixed as high as possible. The result is shown in Fig. 6.24, including the result triggered by PD current trigger.
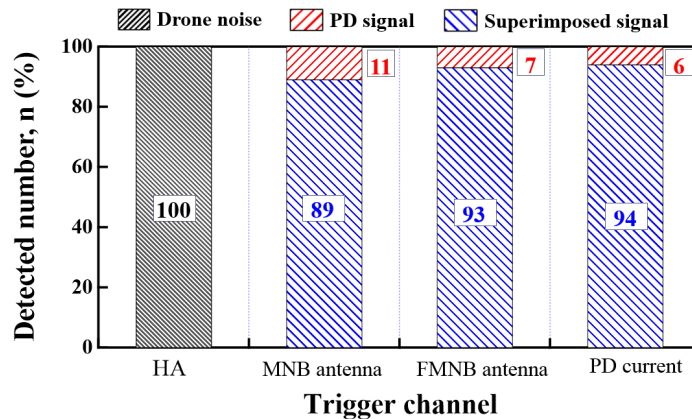
Fig. 6.24   PD signal under the drone noise measurement depends on trigger antenna

In Fig. 6.24, it was clearly shown that all events that the MNB and FMNB antenna detected were PD signals, even including the superimposed PD signals on the drone noise, which was the same tendency as the PD current trigger result, while the HA antenna could not at all. Even if the MNB and FMNB antennas can detect the PD signal under drone noise equality 100 %, the signal-noise ratio of the measured EM wave was drastically changed based on the antennas. Fig. 6.25 showed the signal-noise ratio of each antenna when the trigger antenna was an FMNB antenna. These experimental results demonstrate that the FMNB antenna has a high noise resistance ability for Wi-Fi noise.
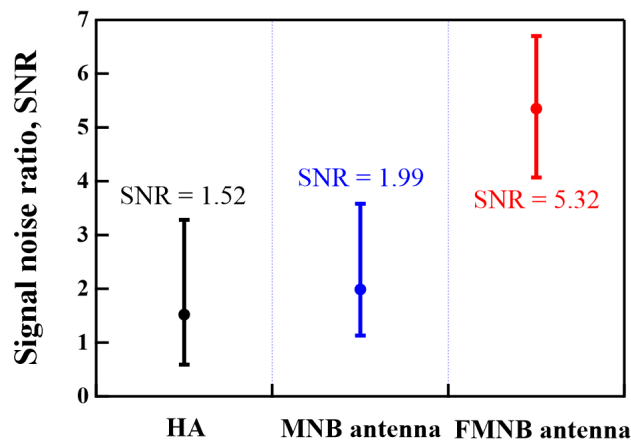
Fig. 6.25   The signal-noise ratio of antennas for PD signal under drone measurement when trigger antenna was FMNB

In addition, to estimate the repetition speed of PD signal and drone noise, the independent measurement results were used. The PD signal and drone noise were measured for each antenna as 100 events at different trigger levels, and measurement duration was recorded. The repetition rate was calculated for PD signal and drone noise based on this measurement time, as shown in Fig. 6.26. From these repetition rates, it is

clearly seen the following things and the PD under noise measurement confirmed:

- For HA, the drone repetition rate is much higher than PD repetition. Therefore, the PD detection rate is almost 0.

- For MNB antenna, the PD repetition rate is higher than drone repetition when the trigger level is higher than the critical level (T_{CR}). It means the MNB antenna can detect the PD signal when the trigger level higher than T_{CR}. If the trigger level is reduced, the PD detection rate is drastically reduced because of the high repetition of drone noise. Therefore, there is a PD detection zone from T_{CR} to the maximum level of PD signal.

- For the FMNB antenna, the PD detection rate is very high even if the trigger level is reduced because of its strong noise reduction ability. It means the PD detection zone of the FMNB antenna is much wider than the MNB antenna from PD signal level up to background noise.
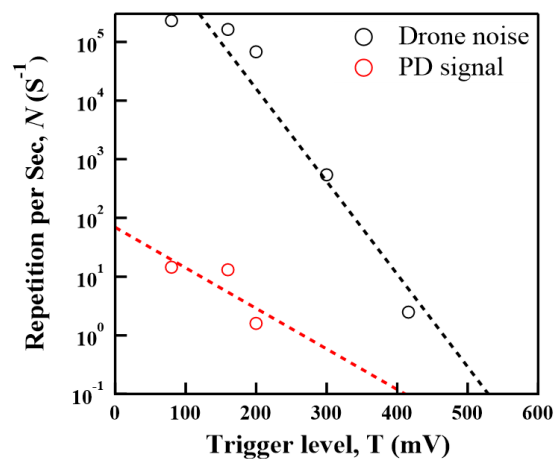
(a) Triggered by HA
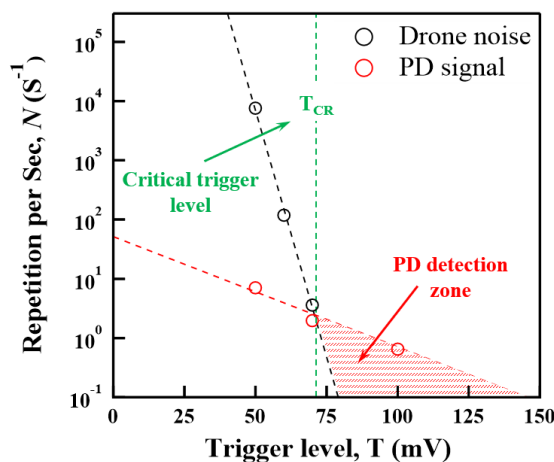
(b) Triggered by MNB antenna

Fig. 6.26   The PD signal and drone noise repetition rate depending on trigger antenna (continued on the following page)
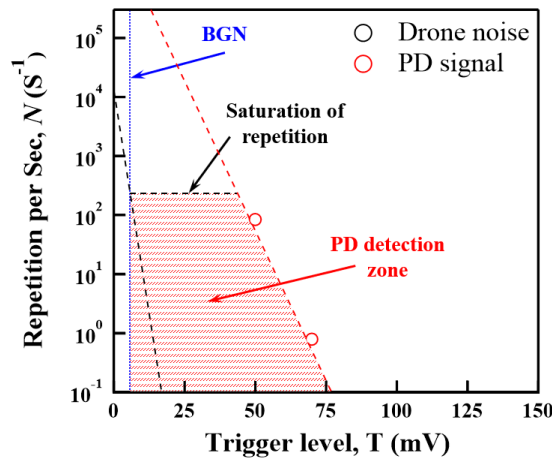
(c) Triggered by FMNB antenna

Fig. 6.26   The PD signal and drone noise repetition rate depending on trigger antenna

Then, the PD signal under the drone noise measurement was performed again to check the second case of PD detection when the trigger level changed for each antenna. The measurement results are summarized and shown in Table 6.4. The HA could not detect the PD signal in all cases while the PD detection rate of the MNB antenna reduced whenever the trigger level reduced. FMNB antenna gave a high performance for PD measurement under the drone noise even if the trigger level reduced up to 25 % of the amplitude of the PD signal. This result demonstrates the conclusions based on the repetition rate. The FMNB antenna can detect the PD signal under high Wi-Fi noise with a high signal-noise ratio.

Table 6.4. PD detection ratio when trigger antenna was changed

Trigger antenna	Trigger level		Result		
	%	mV	PD	PD+Drone	Drone
HA	100	416	0	0	**100**
	73	304	0	0	**100**
	38	160	0	0	**100**
MNB	100	80	11	89	0
	87	70	0	15	**85**
	75	60	0	0	**100**
FMNB	100	70	7	95	0
	85	60	5	93	0
	70	50	8	92	0

6.5   Conclusion

This chapter designed and evaluated the enhanced Filtered Multiple Narrow Band (FMNB) antenna consisting of the MNB antenna and microstrip low-pass filter theoretically and experimentally. The conclusions are shown below.

1. The FMNB antenna with higher communication noise resistance than the MNB antenna was successfully developed without size extension by applying the microstrip feed method to form the high-and-low impedances, which act as series inductors and shunt capacitors.

2. The microstrip filter increased the Wi-Fi noise resistance ability from 15 dBm to more than 30 dBm.

3. The FMNB antenna was applied to detect the PD signal under drone noise with the improved MNB antenna and HA. The measurement result showed that the HA could not detect the PD signal under drone noise due to high amplitude and repetition of drone noise, while MNB and FMNB antennas could detect the PD signal with a high PD detection rate.

4. The PD detection rate of the MNB antenna is reduced depending on trigger level due to the repetition ratio between PD signal and drone noise. For the FMNB antenna, the PD detection rate is almost irrelative to the trigger level because of high noise reduction. Even if the trigger level reduced up to 30% of the PD signal, the FMNB antenna could detect the PD signal with a high detection rate.

5. In addition, the FMNB antenna detected the PD signal under drone noise with the highest SNR_{FMNB} around 5.32 while SNR_{MNB}=1.99 and SNR_{HA}=1.52. Based on the above result, the FMNB antenna has a high noise resistance ability at Wi-Fi noise frequency.

6. In addition, the microstrip filter can be designed for different frequency bands to resist certain noises.

References

[1] G. V. R. Xavier, A. C. De Oliveira, A. D. C. Silva, L. A. M. M. Nobrega, E. G. Da Costa, and A. J. R. Serres, "Application of Time Difference of Arrival Methods in the Localization of Partial Discharge Sources Detected Using Bio-Inspired UHF Sensors," *IEEE Sens. J.*, Vol. 21, No. 2, pp. 1947–1956, 2021

[2] C. F. F. C. Cunha, A. T. Carvalho, M. R. Petraglia, and A. C. S. Lima, "A new wavelet selection method for partial discharge denoising," *Electr. Power Syst. Res.*, Vol. 125, pp. 184–195, 2015.

[3] X. Chen, Y. Qian, G. Sheng, and X. Jiang, "A time-domain characterization method for UHF partial discharge sensors," *IEEE Trans. Dielectr. Electr. Insul.*, Vol. 24, No. 1, pp. 110–119, 2017.

[4] J.-S. Hong, *for RF / Microwave Applications*. 2011.

[5] G. H. Sun, S. W. Wong, L. Zhu, and Q. X. Chu, "A Compact Printed Filtering Antenna with Good Suppression of Upper Harmonic Band," *IEEE Antennas Wirel. Propag. Lett.*, Vol. 15, pp. 1349–1352, 2016.

[6] C. T. Chuang and S. J. Chung, "Synthesis and design of a new printed filtering antenna," *IEEE Trans. Antennas Propag.*, Vol. 59, No. 3, pp. 1036–1042, 2011.

[7] R. Bancroft, *Antenna Design Second Edition*. .

[8] W. Wang, S. S. Zhong, and S. B. Chen, "A novel wideband coplanar-fed monopole antenna," *Microw. Opt. Technol. Lett.*, Vol. 43, No. 1, pp. 50–52, 2004.

[9] J. Liang, L. Guo, C. C. Chiau, X. Chen, and C. G. Parini, "Study of CPW-fed circular disc monopole antenna for ultra-wideband applications," *IEE Proc. Microwaves, Antennas Propag.*, Vol. 152, No. 6, pp. 520–526, 2005.

[10] T. Bandi and S. Ohtsuka, "Application of Microstrip Filter for Multiple Narrow Band Antenna to Detection of Partial Discharge," in *The 22nd International Symposium on High Voltage Engineering, 2021*, pp. 1–5.

[11] T. Bandi and S. Ohtsuka, "Partial Discharge Detection of Multiple-Narrow Band Antenna under the Radio Communication Noise," *IEEJ Trans. Electr. Electron. Eng.*, Vol. 16, No. 5, pp. 715–721, 2021.

Chapter 7
Conclusions

Partial discharge (PD) is a pre-breakdown phenomenon that can cause the insulation deterioration of HV equipment. Thus, detection of PD signals enables us to evaluate the insulation condition and avoid catastrophic breakdown. This also brings the reliable operation of the electric power system consisting of the HV equipment.

The UHF method, which is one of the PD detection methods on the PD-emitted electromagnetic wave in the UHF bands, has been widely used in the electric power system because this method has many advantages like a non-direct connection with the HV circuit, high sensitivity, quick response as a real-time-enabled measurement and so on. However, the rapid development of ICT and digital technology could impact the PD detection by the UHF method in view of the noise interference by the communication waves, consequently reducing the sensitivity and the detection ability of PDs. Thus, the elimination of the communication noise is strongly required in parallel with the wideband PD detection in the UHF method.

Many researchers have investigated the wideband detection methods in the UHF band and the noise elimination methods for the communication waves for PD detection with high sensitivity, but a UHF PD sensor that fully satisfies them has not been realized. Under this background, this dissertation deals with the development of the wideband UHF sensor with high noise resistance ability for PD detection under noise conditions.

7.1   Summary of This Dissertation

In Chapter 2, the setup of the simulation on the antenna performance and the HV experiment, as well as procedures used in this study, were described in detail. As the PD sources, different insulation media like SF_6 gas, dry air, and electrical tree discharge in the XLPE sample were prepared and applied to evaluate the developed UHF sensors. Meanwhile, two different types of noise were also used to investigate the noise resistance ability.

In Chapter 3, the design method on the Multiple Narrow Band (MNB) antenna, which is my newly proposed and developed as a wideband UHF sensor with high noise resistance, was established based on the theoretical and experimental discussion. The

MNB antenna satisfied the main requirements of the UHF sensor and could be optimized by numerical simulation. The detection frequency bandwidth realized more than 1 GHz, and the reflection loss was higher than -6 dB at the elimination frequencies, which means the MNB antenna had excellent properties like wideband detection and high noise resistance in the communication and ISM bands. The design rule was summarized as the flow chat that allows us to develop the MNB antenna with different detection and elimination frequencies depending on the purpose.

In Chapter 4, the discharge detection property and the directivity of the MNB antenna were clarified and compared with those of the HA. The directivity of the MNB antenna was investigated by the breakdown experiment, and the omnidirectional radiation pattern was confirmed, which was the same pattern as the theory. The antenna can be placed at the bottom or side of the wall in the HV equipment for PD detection because of the directivity and electric field detection. The MNB antenna can detect different PD signals from the different insulations and discharge types, and the signal intensity, *i.e.,* the peak to peak amplitude of the antenna output, of the MNB antenna showed a good correlation with that of the HA.

In Chapter 5, the communication noise resistance ability of the MNB antenna was discussed based on two different noise sources; (i) artificial noise emitted from SG with constant amplitude and (ii) the Wi-Fi noise emitted from the commercial drone. The PD in SF_6 gas under noise source experiment was performed to make practical conditions. From the artificial noise experiment result, it was found that the MNB antenna detected the PD in SF_6 gas under artificial noise. The signal-noise ratio of the MNB antenna was around 2, which was higher than that of the HA antenna ($SNR_{HA} \approx 1.3$) under the elimination frequency while it was around 1.2, same as SNR_{HA} under detection frequency. From the drone noise measurement result, the MNB antenna received the drone noise with 15 dBm lower amplitude than that measured by HA. Due to this noise amplitude reduction, the MNB antenna could detect the PD signal in SF_6 gas under drone noise ($SNR_{MNB} \approx 1.4$) while the HA could not detect ($SNR_{HA} \approx 0.6$). The 100 times measurement result used the segment memory method shows that the PD detection rate under drone noise was 1% and 94% for HA and MNB antenna, respectively. The PD signal and drone noise repetition rates were investigated to understand the advantage of MNB antenna compared with HA. The results show that the PD detection rate was almost 0 for HA because PD signal repetition (R_{S_HA}) was much lower than drone noise repetition (R_{N_HA}).

For the MNB antenna, the PD detection rate was changed depending on the trigger level because the ratio of PD signal and drone noise repetition was noticeably changed based on the trigger level. Until the trigger level was selected as lower than the critical level, the MNB antenna could detect the PD signal under drone noise with the PD detection rate more than 50% because the PD signal repetition was higher than the drone noise repetition ($R_{S\_MNB} \geq R_{N\_MNB}$). If the trigger level was reduced more than the critical level, the PD detection rate was reduced because of $R_{S\_MNB} \leq R_{N\_MNB}$. Based on these results, it can be concluded that the MNB antenna has a high noise resistance ability at the elimination frequencies.

In Chapter 6, the communication noise elimination ability of the MNB antenna was further improved by adding the low-pass filtering function. The enhanced Filtered Multiple Narrow Band (FMNB) antenna was designed with higher communication noise resistance than the MNB antenna. Applying the micro-strip feed method to form the high-and-low impedances, which act as series inductors and shunt capacitors, the FMNB antenna was realized-without size extension. This enhancement increased the Wi-Fi noise resistance ability from 15 dBm to more than 30 dBm. The FMNB antenna was applied to detect the PD signal under drone noise with the improved MNB antenna and HA. The measurement result showed that the HA could not detect the PD signal under drone noise due to high amplitude and repetition of drone noise, while MNB and FMNB antennas could detect the PD signal with a high PD detection rate. However, the PD detection rate of the MNB antenna is reduced depending on trigger level due to the repetition ratio between PD signal and drone noise. For the FMNB antenna, the PD detection rate is almost irrelative to the trigger level because of high noise reduction. Even if the trigger level reduced up to 30% of the PD signal, the FMNB antenna could detect the PD signal with a high detection rate. In addition, the FMNB antenna detected the PD signal under drone noise with the highest SNR_{FMNB} around 5.32 while SNR_{MNB}=1.99 and SNR_{HA}=1.52. Based on the above result, the FMNB antenna has a high noise resistance ability at Wi-Fi noise frequency. In addition, the microstrip filter can be designed for different frequency bands to resist certain noises.

Moreover, the MNB antenna can be designed for different PD signals, and different noise condition depends on the purpose by adjusting the detection and elimination frequencies. It means the MNB antenna can be used in all types of HV equipment as a

UHF sensor. Also, the noise resistance ability makes the MNB antenna is suitable to cooperate with other ICT and digital technology as a wireless and smart sensor.

7.2   Future Subjects

This study successfully designed and developed a novel wideband UHF sensor for PD detection with high noise resistance. Consequently, the sensor's performance was validated experimentally. Based on the satisfied result of this study, some suggestions for future work are proposed.

1. Flexible sensor for a cylindrical or non-flat surface.

    UHF sensor is commonly installed in the wall of the HV equipment. However, the wall is generally a non-flat surface. Therefore, the flexible sensor is suitable for installation in HV equipment. The MNB antenna has a flat and very thin structure, which gives a chance to make a flexible sensor for PD detection, such as a cylindrical surface of the GIS tank.

2. Size reduction methods for MNB antenna.

    In this study, the size limitation is not considered a general study, and however, the sensor size is one of the important parameters in practice. Therefore, size reduction methods are needed for MNB antenna to develop a small antenna. The L-shaped MNB antenna was designed and fabricated to reduce antenna size, and the simulation and fabrication result is attached in Appendix. But, a more advanced size reduction method can be used, such as a meandering method.

3. PD detection system using MNB antenna as a smart sensor.

    The digital technology applied and enhanced every technical field, including the HV substation such as digital substation. The MNB antenna can cooperate with digital technology without noise interference. Therefore, the PD detection system can be developed based on this idea, reducing the electrical connection between sensors and diagnostic devices and increasing processing time and accuracy.

List of Publications

Journal paper

1. MNB antenna for detection of discharge emitted EMW for insulation diagnostic

    IEEJ Transactions on Electrical and Electronic Engineering, Vol 15, Issue 12, pp. 1751-1757, Dec. 2020

    Authors: **Tuvshinbayar Bandi** and Shinya Ohtsuka

2. Partial discharge detection of MNB antenna under the radio communication noise

    IEEJ Transactions on Electrical and Electronic Engineering, Vol 16, Issue 5, pp. 715-721, May. 2021

    Authors: **Tuvshinbayar Bandi** and Shinya Ohtsuka

Awards

1. Excellent Student Award of the IEEE Fukuoka Section: "Developing of Multiple-narrowband antenna to detect partial discharge-emitted signal under radio communication noise environment"

    Proceeding of the 8th International Conference on Condition Monitoring and Diagnosis (CMD), 2020, pp. 154-157, Phuket, Thailand, Oct. 2020

    Authors: **Tuvshinbayar Bandi**, Marina Tanaka, Hiroki Furuie and Shinya Ohtsuka

2. Best paper presentation award: "Application of microstrip filter for Multiple Narrow Band antenna to detection of partial discharge"

    Proceeding of the 73rd Joint Conference of Electrical, Electronics and Information Engineers in Kyushu, Volume 2020 02-2P-05, p. 366, Fukuoka, Japan, Sep. 2020

    Authors: **Tuvshinbayar Bandi** and Shinya Ohtsuka

International Proceedings

1. Developing of Multiple-narrowband antenna to detect partial discharge-emitted signal under radio communication noise environment

    Proceeding of the 8th International Conference on Condition Monitoring and Diagnosis (CMD), 2020, pp. 154-157, Phuket, Thailand, Oct. 2020

Authors: **Tuvshinbayar Bandi**, Marina Tanaka, Hiroki Furuie and Shinya Ohtsuka

2. Application of microstrip filter for Multiple Narrow Band antenna to detection of partial discharge

   Proceeding of the 22nd International Symposium on High Voltage Engineering, pp. 1-5, Xi'an, China, Nov. 2021

   Authors: **Tuvshinbayar Bandi** and Shinya Ohtsuka

National Proceedings

1. Towards development of a new Multiple-narrowband strip antenna for health diagnostic by detecting discharge-emitted signals

   Proceeding of the 1st International Conference on Joint Research Program in Mongolia, Ulaanbaatar, Mongolia, Mar. 2019

   Authors: **Tuvshinbayar Bandi**, Bat-Erdene Bayar and Shinya Ohtsuka

2. Development of a Multiple-narrowband Strip Antenna for Health Diagnostic of Electric Power Equipment by Detecting Discharge-emitted Electromagnetic Signals

   Proceeding of the 30th Annual Conference of Power & Energy Society, IEEJ, pp. 242-243, Hiroshima, Japan, Sep. 2019

   Authors: **Tuvshinbayar Bandi** and Shinya Ohtsuka

3. Application of developed MNB antenna with 4 strips to detect PD emitted EMW in SF_6 gas

   Proceeding of the 72nd Joint Conference of Electrical, Electronics and Information Engineers in Kyushu, Volume 2019 04-2A-02, p. 327, Fukuoka, Japan, Sep. 2019

   Authors: **Tuvshinbayar Bandi**, Marina Tanaka, and Shinya Ohtsuka

4. Fundamental detection properties of a developed MNB antenna for health diagnostic of electric power equipment

   Proceeding of the Mongolia-Japan traditional seminar, S2-06-01, Nagoya, Japan, Dec. 2019

   Authors: **Tuvshinbayar Bandi** and Shinya Ohtsuka

5. Discharge signal measurement using newly designed antenna for health diagnostics

Proceeding of the 7th Research Symposium on High-Voltage Engineering and Power Systems, Abu-Dhabi, United Arab Emirates, Feb. 2020

Authors: **Tuvshinbayar Bandi** and Shinya Ohtsuka

6. Application of Microstrip Filter on Multiple-narrowband Antenna to Reduce 2.4 GHz, Wi-Fi Noise

   Proceeding of the 2020 Annual Meeting of the Institute of Electrical Engineers of Japan, p. 60, Tokyo, Japan, Mar. 2020

   Authors: **Tuvshinbayar Bandi** and Shinya Ohtsuka

7. Application of Multiple Narrow Band (MNB) antenna to discriminate partial discharge type using UHF method

   Proceeding of the 73rd Joint Conference of Electrical, Electronics and Information Engineers in Kyushu, Volume 2020 02-2P-05, p. 366, Kitakyushu, Japan, Sep. 2020

8. Application of developed multiple narrow band antenna for discharge detection under the communication noise

   Proceeding of the 8th International Symposium on Applied Engineering and Sciences, SAES 2020, Fukuoka, Japan, Dec. 2020

   Authors: **Tuvshinbayar Bandi** and Shinya Ohtsuka

9. Usage of the Multiple-narrowband antenna for partial discharge detection under communication noise

   Proceeding of the 8th Research Symposium on High-Voltage Engineering and Power Systems, Online, Jan. 2021

   Authors: **Tuvshinbayar Bandi** and Shinya Ohtsuka

10. Research of developed Multiple Narrow Band antenna for partial discharge detection under the noise condition

    Proceeding of International Conference on Innovation and Entrepreneurship Development, Ulaanbaatar, Mongolia, May. 2021

    Authors: **Tuvshinbayar Bandi** and Shinya Ohtsuka

11. Application of Novel High Noise Resistance UHF Sensor to Partial Discharge Detection under Flying Drone Noise

    Proceeding of the 9th Research Symposium on High-Voltage Engineering and Power Systems, Abu-Dhabi, United Arab Emirates, Feb. 2022

Authors: **Tuvshinbayar Bandi** and Shinya Ohtsuka

12. Partial Discharge Detection Ability of Filtered Multiple Narrow Band UHF Sensor under Flying Drone Noise

Proceeding of the 2022 Annual Meeting of the Institute of Electrical Engineers of Japan, pp. 1-2, Tokyo, Japan, Mar. 2022

Authors: **Tuvshinbayar Bandi** and Shinya Ohtsuka

Biography of the Author

Tuvshinbayar Bandi was born on June 14, 1992, at Umnugobi province, Mongolia. He is the son of military colonel Bandi Ninjbayar Orkhid and Mrs. Oyuntsetseg Gunraaz Borjigon. He received the B.Eng. and M.Eng. degrees in electrical engineering from the Mongolian University of Science and Technology, Mongolia, in 2013 and 2016. While studying the master course, he was hired as an electrical engineer at Electomonseti LLC, in which he carried out construction, adjustment, and testing of high voltage transmission and distribution lines and substations. From 2016 to 2017, he was employed as an officer of scientific research and innovation in the Power Engineering School at the Mongolian University of Science and Technology. Since 2018, he has been employed as an assistant professor in the electrical technique department, Power Engineering School, Mongolian University of Science and Technology. He moved to Japan in November of 2018 as a research student at Ohtsuka laboratory, Kyushu Institute of Technology. Continuously, he entered the doctoral course of electrical engineering at Ohtsuka laboratory, Kyushu Institute of Technology, in April 2019. His research topic was involved the development of a novel wideband UHF sensor with high noise resistance ability for high voltage insulation diagnosis. In 2020, Tuvshinbayar Bandi was awarded the best paper presentation award from the Institute of Electrical Engineers of Japan (IEEJ) and the excellent student award of the Institute of Electrical and Electronics Engineers (IEEE) Fukuoka Section. His research interests include the protection and automation of electric power system and high voltage insulation properties such as diagnostic techniques and UHF sensors to detect partial discharge for electrical power apparatus. Tuvshinbayar Bandi is a member of the IEEJ and the Institute of Electrical and Electronics Engineers (IEEE), Electromagnetic Comfortability Society (EMC).